ALMA MATER STUDIORUM · UNIVERSITÀ DI BOLOGNA

School of Science
Department of Physics and Astronomy
Master Degree in Physics

SiPM Detector Timing Response Study for the Electron-Ion Collider

Supervisor:
Prof. Gilda Scioli

Co-Supervisor:
Dott. Roberto Preghenella

Presented by:
Chiara Fraticelli

Anno Accademico 2021/2022

Abstract

The Electron-Ion Collider (EIC) will be a new high luminosity large-scale and high-polarization collider designed to investigate the QCD dynamics in the nucleons with unprecedented precision. It is planned to be built at the Brookhaven National Lab (BNL) in the US [1].

A key element of a general-purpose experiment at EIC is a detector providing particle identification in the hadronic endcap. It has to allow a 3σ separation of particles in a broad momentum range from a few GeV/c up to 50 GeV/c, while operating in a high magnetic field region. To meet these requirements a dual-radiator RICH (dRICH) is being developed: it exploits Cherenkov light produced by two different mediums to cover the full momentum range without penalty owing to the Cherenkov threshold of the gas.

Through a dRICH prototype, the performance of Silicon PhotoMultipliers (SiPM), the baseline photo-sensor candidate for the dRICH was tested. They provide a cheap, highly efficient technology and they are not sensitive to the high magnetic field.

The data analysis presented in this dissertation was taken during the beam test performed between 12th and 19th October, 2022 in which the performance of different SiPMs coupled to a dRICH prototype was tested. The readout electronics for the SiPM employed in the beam test was based on the ALCOR (A Low power Chip for Optical sensors Readout) chip. This chip performs time measurements through the *rollover*, *coarse* time and *fine* time components, which combine to provide a signal time-of-hit.

The *fine* time component is a correction on the *coarse* time, which is especially useful to apply in the event of working in an accelerator environment with high luminosity, as is the case with the EIC. The presence of the fine time correction permits a more precise time-of-hit measurement and the reduction of background through the performance of cuts.

The work here presented concerns the refinement of the Reference Timing system Time Resolution as a result of the introduction of corrections derived from the *fine* time.

The results show the Reference Timing system was calibrated to provide a measured Time Resolution of 135 ± 2 ps.

Contents

Chapter 1

Fundamental Physics at EIC

1.1 The EIC and its Realization

The Electron-Ion Collider (EIC) is a new large-scale particle accelerator facility conceived by U.S. nuclear and accelerator physicists over two decades and planned for construction at Brookhaven National Laboratory on Long Island, NewYork by the U.S. Department of Energy in the 2020s. The EIC will study protons, neutrons and atomic nuclei through an electron microscope. Its resolution and intensity is achieved by colliding high-energy electrons with high-energy protons or ion beams. The EIC provides the capability of colliding beams of polarized electrons with polarized beams of light ions at high intensity.

The main design requirements of the EIC are:

- Highly polarized electron ($\smile$ 70%) and proton ($\smile$ 70%) beams

- Ion beams from deuterons to heavy nuclei such as gold, lead, or uranium

- Variable $e + p$ center-of-mass energies from 20-100 GeV, upgradable to 140 GeV

- High collision electron-nucleon luminosity 10^{33} - $10^{34} cm^{-2} s^{-1}$

- Possibility to have more than one interaction region

Several of the above performance parameters will be realized for the first time at EIC in a collider mode, such as the availability of nuclear beams and polarized nucleon beams along with the operation at high collision luminosity.

The EIC will collide bright, intense counter circulating beams of electrons and ions and use sophisticated, large detectors to identify specific reactions whose precise measurement can provide better insight into the structure of the nucleon and the nucleus than previously obtained.

The realization of the EIC is led jointly by Brookhaven National Laboratory and Thomas Jefferson National Accelerator Facility at Newport News, Virginia and its design is represented in Figure 1.1. This realization is expected to take around a decade, with beam operations to start in the early 2030s [7].
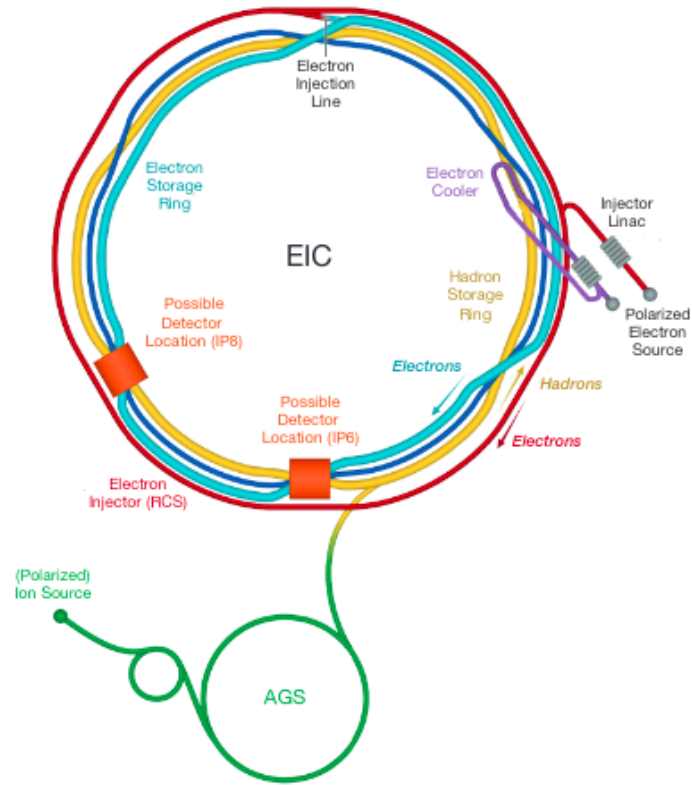

Figure 1.1: Schematic layout of the planned EIC accelerator based on the existing RHIC complex at Brookhaven National Laboratory.

1.2 Physics Deliverables of the EIC

DIS (deep inelastic scattering) is the name given to a process used to probe the insides of hadrons (particularly baryons, such as protons and neutrons), using electrons, muons and neutrinos.

With such a facility, the EIC physics program would have an excellent start toward addressing the following fundamental questions through targeted measurements [7]:

- Proton spin: The EIC would be able to supply decisive measurements concerning the quark and gluon intrinsic spin contribution to the proton spin.

- Motion of quarks and gluons in the proton: Semi-inclusive measurements with polarized beams would allow the precise selective probing of the correlation between the spin of a fast moving proton and the confined transverse motion of both quarks and gluons within it.

- Tomographic images of the proton: By measuring exclusive processes, the EIC, with its unprecedented luminosity and detector coverage, would create detailed images of the proton gluonic matter distribution, as well as images of sea quarks. Such measurements would reveal aspects of proton structure that are intimately connected with QCD dynamics at large distances.

- QCD matter at an extreme gluon density: By measuring the diffractive cross sections at the same time of the total deep inelastic scattering cross-sections in electron+proton and electron+nucleus collisions, the EIC would yield the first unambiguous evidence for the novel QCD matter of saturated gluons. The EIC is poised to explore with precision the new field of the collective dynamics of saturated gluons at high energies.

- Quark hadronization: By measuring pion and D^0 meson production in both electron+proton and electron+nucleus collisions, the EIC would provide the first measurement of the quark mass dependence of the hadronization along with the response of nuclear matter to a fast moving quark.

1.3 Physics Measurements and Requirements

Some of the most fundamental questions in science the Electron-Ion Collider will address will include the origin of the nucleon mass, the nucleon spin, and the emergent properties of a dense system of gluons.

Crucial physics topics that led to the requirement for the construction of an EIC in addition to key science questions that it will address are [8]:

- How do underlying parton interactions effect nucleon properties such as mass and spin?

- How are partons within the nucleon distributed in both momentum and position space?

- How do color-charged quarks and gluons, and jets, interact with a nuclear medium? How do the confined hadronic states emerge from these quarks and gluons? How do the quark-gluon interactions create nuclear binding?

- How does a dense nuclear environment affect the dynamics of quarks and gluons, their correlations, and their interactions? What happens to the gluon density in nuclei? Does it saturate at high energy, creating gluonic matter or gluonic phase with universal properties in all nuclei and even in nucleons?

1.4 Nucleon Spin and its 3D Structure and Tomography

Years of experiments involving deep inelastic scattering (DIS) on nucleons using electron or muon beams have provided valuable insights into the manner in which quarks and gluons (commonly referred to as partons) distribute the momentum within a swiftly moving nucleon. However, these experiments have not fully addressed the question of how partons apportion the nucleon's spin or contribute to other intrinsic properties like mass and magnetic moment. Previous investigations primarily focused on determining the longitudinal momentum distribution of quarks and gluons, providing a limited one-dimensional perspective of nucleon structure.

The Electron-Ion Collider (EIC) has been specifically devised to significantly enhance our understanding of nucleon structure. By generating multi-dimensional maps that encompass the spatial, momentum, spin, and flavor distributions of partons, the EIC aims to unlock deeper insights into the intricate nature of the nucleon.

The 12 GeV upgrade [1] [4] of CEBAF [2] at JLab [3] [5] and the COMPASS [4] [6] at CERN will initiate such studies in predominantly valence quark region. However, these programs will be further extended at the EIC to explore the role of the gluons and sea quarks in determining the hadron structure and properties. This will resolve crucial questions, such as whether a substantial "missing" portion of nucleon spin resides in the gluons. By providing high energy probes of partons' transverse momenta, the EIC should also explain the role of their orbital motion contributing to nucleon spin [7].

---

[1]The scientific program of the 12 GeV Continuous Electron Beam Accelerator Facility (CEBAF) addresses important topics in nuclear, hadronic, and electroweak physics, including nuclear femtography, meson and baryon spectroscopy, quarks and gluons in nuclei, precision tests of the standard model and dark sector searches

[2]The CEBAF (Continuous Electron Beam Accelerator Facility) is a scientific research facility located in Newport News, Virginia, USA. It is a particle accelerator that produces a continuous beam of high-energy electrons that are used to investigate the structure of matter.

CEBAF was originally built in the 1980s as a four-pass electron accelerator, but underwent a major upgrade in the 2000s to become a continuous-wave (CW) accelerator. The upgrade included the installation of new superconducting radiofrequency (SRF) cavities, which allow the electrons to be accelerated to higher energies than were possible with the original technology.

[3]Thomas Jefferson National Accelerator Facility (Jefferson Lab) is a U.S. Department of Energy Office of Science national laboratory. Scientists worldwide utilize the lab's unique particle accelerator, known as the Continuous Electron Beam Accelerator Facility (CEBAF), to probe the most basic building blocks of matter - helping us to better understand these particles and the forces that bind them - and ultimately our world.

[4]The COMPASS (Common Muon and Proton Apparatus for Structure and Spectroscopy) is a particle physics experiment located at the CERN (European Organization for Nuclear Research) laboratory in Geneva, Switzerland. It is designed to study the structure and properties of hadrons, which are particles composed of quarks, such as protons and neutrons.

1.4.1 The Spin and Flavor Structure of the Nucleon

Over the past two decades, global experimental initiatives have revealed that the spin of quarks and antiquarks contributes to only approximately 30% of the total spin of a proton. Recent findings from RHIC suggest that gluons also make a non-zero contribution to the spin in the currently explored kinematic range, but this contribution is not sufficient to account for the remaining 70%.

The overall helicity contribution of partons to the proton spin is highly dependent on the minimum momentum fraction x that can be probed by experiments. The Electron-Ion Collider (EIC) would serve as a powerful tool to address this issue by significantly lowering the minimum momentum fraction by two orders of magnitude and covering a wide range of momentum transfers Q. Through collisions between longitudinally polarized electrons and nucleons, the EIC would enable precise quantification of how the spins of gluons and quarks of different flavors contribute to the proton's spin. Both inclusive and semi-inclusive deep inelastic scattering (DIS) measurements would be conducted, with the former detecting only the scattered electron and the latter identifying an additional hadron produced in the collisions.

Figure 1.3 illustrates the reduction in uncertainties associated with the contributions to the nucleon spin from the spin of gluons, quarks, and antiquarks within the x range of 0.001 to 1.0, achievable during the initial operations of the EIC. In the future, the kinematic range could be expanded further, reaching down to x values around 0.0001, thereby significantly reducing the uncertainty in the unmeasured small-x region. While the central values of the helicity contributions in Figure 1.3 are derived from existing data, they may change as new data becomes available in the low-x region. The uncertainties presented here are based on the latest theoretical treatment incorporating all relevant data pertaining to the nucleon spin puzzle. Undoubtedly, the EIC will have a profound impact on our understanding of these quantities, surpassing any other existing or anticipated facility. The reduced uncertainties will decisively address the question of whether the spin preferences of partons alone can explain the overall proton spin or if additional contributions from the orbital angular momentum of partons within the nucleon are necessary.

1.4.2 The Confined Motion of Partons Inside the Nucleon

Semi-inclusive Deep Inelastic Scattering (SIDIS) measurements exhibit two inherent momentum scales: the high momentum transfer from the electron beam required for precise spatial resolution, and the momentum of the produced hadrons perpendicular to the direction of momentum transfer, which favors small values reflecting the confined motion of partons. Recent notable advancements in theory have established a robust framework that links information about the confined motion of partons within a fast-moving nucleon to transverse momentum-dependent parton distributions (TMDs). TMDs offer
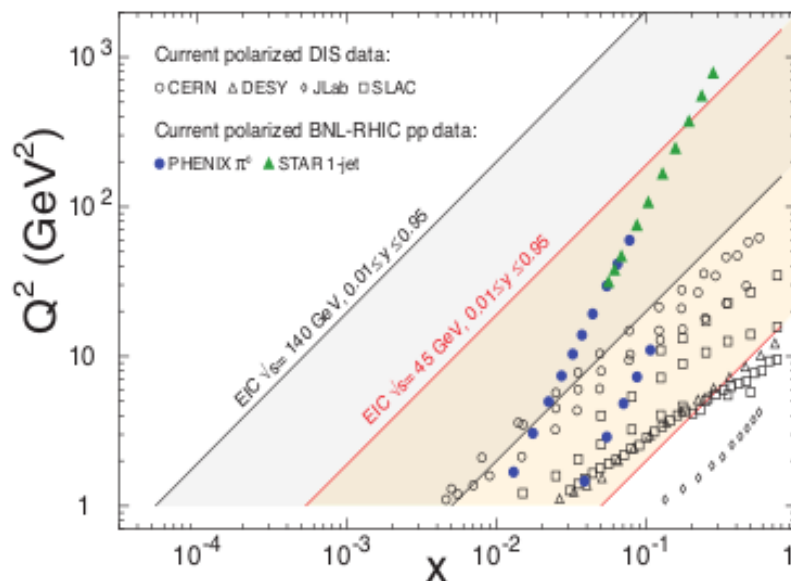
Figure 1.2: The range in parton momentum fraction x vs. the square of the momentum transferred by the electron to the proton Q^2 accessible with the EIC in e+p collisions at two different center-of-mass energies, compared to existing data [7].

sensitivity to correlations between parton motion, parton spin, and the spin of the parent nucleon, which can arise from spin-orbit coupling among the partons, an area that remains largely unexplored.

TMDs provide a means to explore the complete three-dimensional dynamics of the proton, surpassing the longitudinal momentum information provided by conventional parton distributions. The Electron-Ion Collider (EIC) holds immense potential for advancing our understanding of the confined motion of gluons and sea quarks by employing polarized electron and nucleon beams at collider energies. This surpasses the capabilities of any existing or proposed facility.

Figure 1.4 displays the transverse momentum distribution of up quarks inside a proton that is moving in the z-direction (out of the page) with its spin polarized in the y-direction. The color representation indicates the probability of locating the up quarks within the proton.

1.4.3 The Tomography of the Nucleon - Spatial Imaging of Gluons and Sea Quarks

By selecting specific final states in electron-proton scattering, the Electron-Ion Collider (EIC) will explore the transverse spatial distribution of sea quarks and gluons within the fast-moving proton, taking into account the parton's longitudinal momentum fraction,

9
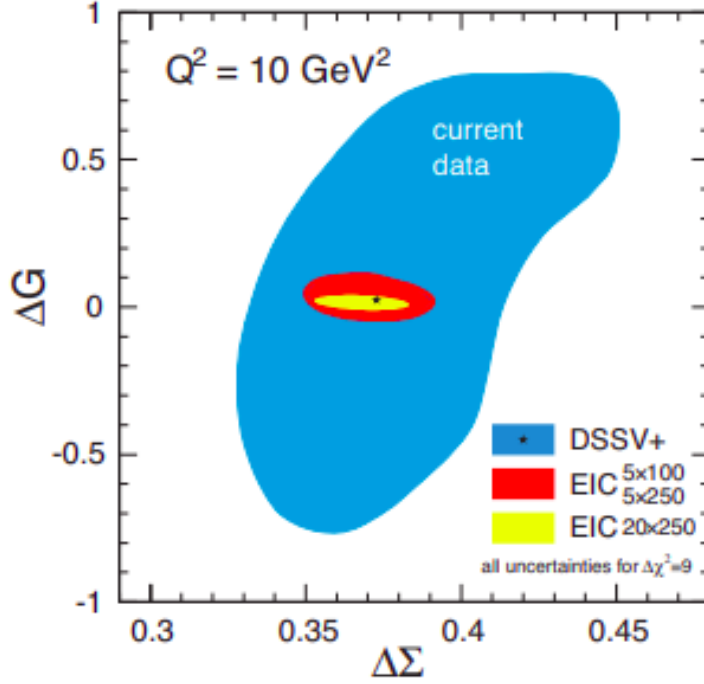
Figure 1.3: Accuracies for the correlated truncated integrals of $\Delta\Sigma$ and Δg over $0.001 \leq x \leq 1$, on the basis of the "DSSV+" analysis (outer area) and projected for an EIC (inner areas) [2].
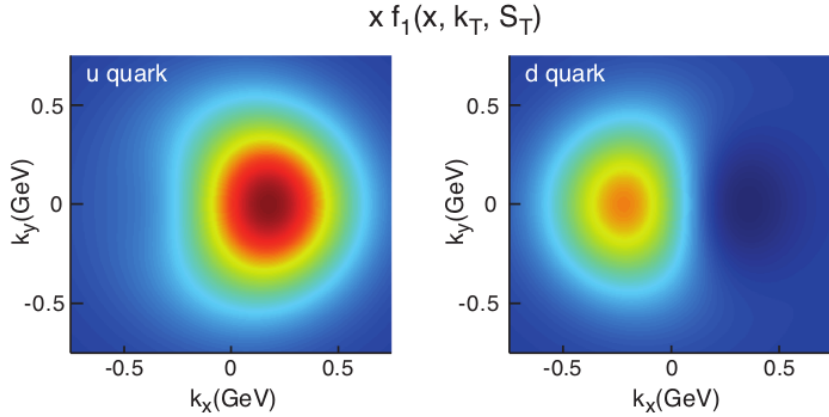
Figure 1.4: The density in the transverse-momentum plane for unpolarized quarks with x = 0.1 in a nucleon polarized along the $\hat{y}$ direction. The anisotropy due to the proton polarization is described by the Sivers function, for which the model of [3] is used. The deep red (blue) indicates large negative (positive) values for the Sivers function [7].

denoted as x. This spatial distribution provides a complementary perspective on proton structure compared to the information obtained from the transverse momentum distribution of quarks and gluons. It reveals aspects of proton structure that are closely tied to the dynamics of Quantum Chromodynamics (QCD) at large distances.

With its wide range of collision energies, high luminosity, and nearly complete detector coverage, the EIC has the potential to visualize the proton with unparalleled detail and precision across various transverse distances. The accessible parton momentum fractions span a range where sea quarks and gluons dominate, gradually transitioning to a region where valence quarks play a significant role. This allows for connections to be made with the precise imaging expected from the 12 GeV upgrade at Jefferson Lab (JLab) and the COMPASS experiment at CERN.

This is illustrated in Figure 1.5, which shows the precision expected for the spatial distribution of gluons as measured in the exclusive process: electron + proton → electron + proton + J/Ψ.

The information obtained from exclusive processes, through cross-sections and polarization asymmetries, provides tomographic images that are represented by generalized parton distributions (GPDs) [10]. GPDs merge the concepts of parton densities and elastic form factors, offering detailed insights into spin-orbit correlations and the angular momentum carried by partons. This includes information about the spin and orbital motion of the partons. To extract contributions of quark and gluon angular momentum to the proton spin, it is crucial to have a combined kinematic coverage provided by the Electron-Ion Collider (EIC), the upgraded Continuous Electron Beam Accelerator Facility (CEBAF), and the COMPASS experiment.
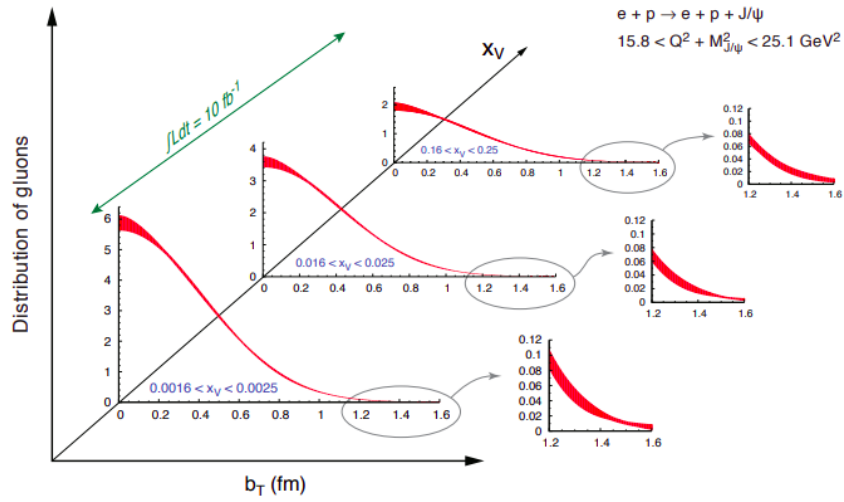
Figure 1.5: The projected precision of the transverse spatial distribution of gluons as obtained from the cross-section of exclusive J/Ψ production. It includes statistical and systematic uncertainties due to extrapolation into the unmeasured region of momentum transfer to the scattered proton. The distance of the gluon from the center of the proton is b_T in femtometers, and the kinematic quantity $x_V = x_B(1 + M_{J/\Psi}^2/Q^2)$ determines the gluon's momentum fraction. The collision energies assumed for the top large x_V plot and the lower x_V plots are E_e= 5, 20 GeV and E_p = 100, 250 GeV, respectively [7].

1.5 The Nucleus, a QCD Laboratory

Understanding the formation of nuclei in Quantum Chromodynamics (QCD) is a fundamental goal in nuclear physics. Nuclei can be regarded as QCD "molecules" with a complex structure that corresponds to bound states of nucleons. The long-term objective is to comprehend the mechanisms behind nucleus formation within the framework of QCD. The Electron-Ion Collider (EIC), with its extensive kinematic range as depicted in Figure 1.6, and its capability to investigate various nuclei through inclusive and semi-inclusive DIS measurements, will be the first experimental facility capable of exploring the internal three-dimensional structure of sea quarks and gluons within a fast-moving nucleus. Additionally, the nucleus itself serves as a unique laboratory for studying the collective behavior of gluonic matter at high gluon occupation numbers and for investigating the propagation of rapidly moving color charges within a nuclear medium.[7].
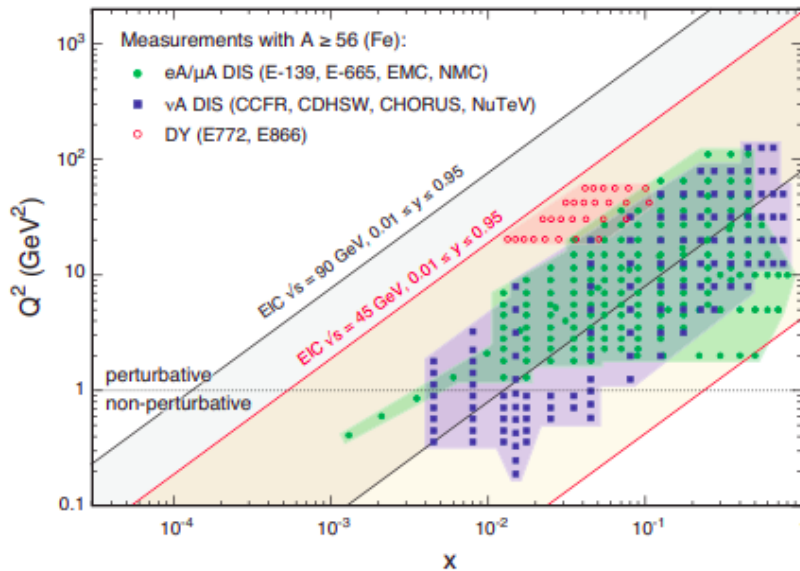
Figure 1.6: The range in the square of the transferred momentum by the electron to the nucleus, Q^2, versus the parton momentum fraction x accessible to the EIC in e-A collisions at two different center-of-mass energies, compared with the existing data [7].

1.5.1 QCD at Extreme Parton Densities

In the framework of Quantum Chromodynamics (QCD), the abundance of soft gluons enables a nonlinear process called gluon-gluon recombination, which limits the growth of density. This self-regulating mechanism in QCD gives rise to a dynamic scale known as the saturation scale (Q_s), where the splitting and recombination of gluons achieve

a balance. At this scale, the gluon density is expected to reach saturation, leading to novel and universal properties of hadronic matter. The saturation scale (Q_s) acts as a boundary, separating the condensed and saturated soft gluonic matter from the dilute, yet confined, quarks and gluons within a hadron.

The existence of this saturated state of soft gluon matter, often referred to as the Color Glass Condensate (CGC), is a direct consequence of gluon self-interactions in QCD. It has been hypothesized that the CGC in QCD possesses universal properties that are common to nucleons and all nuclei. These properties can be systematically calculated if the dynamic saturation scale (Q_s) is sufficiently large. However, achieving a semi-hard Q_s in electron-proton scattering without a multi-TeV proton beam is a challenging task. The EIC, with its heavy ion beams, could provide early access to the saturation regime and allow for the study of CGC properties. In forward lepton scattering with virtual photons, the matter is probed coherently over a characteristic length proportional to $1/x$, which can exceed the contracted diameter of a Lorentz-contracted nucleus. Consequently, all gluons at the same impact parameter of the nucleus, enhanced by the nuclear diameter proportional to $A^{1/3}$ (where A is the atomic weight), contribute to the probed density. This leads to saturation at significantly lower energies compared to electron-proton collisions. While previous facilities such as HERA, RHIC, and the LHC have provided indications of saturated gluonic matter, the EIC would be in a position to further advance and complete the research initiated at those facilities. Figure 1.7 provides a visual representation of the anticipated effects of gluon density saturation in electron+nucleus and electron+proton collisions at the EIC. The left panel focuses on coherent diffractive processes, which involve the beam nucleus remaining intact with a rapidity gap devoid of produced particles. The figure demonstrates that gluon saturation (red dots) significantly increases the fraction of such diffractive events compared to the predictions of the shadowing model (blue dots). In all gluon saturation models, the coherent destructive interaction among colored gluons suppresses both the coherent diffractive and total DIS cross-sections on nuclei relative to those on the proton. However, the suppression of coherent diffractive events, where the nucleus remains intact, is much weaker compared to the suppression of the total cross section. This leads to a pronounced enhancement in the double ratio, as depicted in the left panel of Figure 1.7. Conducting early measurements of coherent diffraction in e+A collisions at the EIC would offer the initial definitive evidence for gluon saturation.

The right panel of Figure 1.7 indicates that gluon saturation is expected to dampen the production of vector mesons in e+A collisions compared to e+p collisions at the EIC. These vector mesons originate from quark-antiquark pair fluctuations in the virtual photon, which subsequently hadronize through the exchange of gluons with the beam proton or nucleus. The degree of suppression depends on the size, or color dipole moment, of the quark-antiquark pair. Specifically, the suppression is notably more pronounced for ϕ mesons (red dots) than for J/Ψ mesons (blue dots). Conducting measurements of these processes at the EIC, as depicted in the right panel of Figure 1.7, would serve as

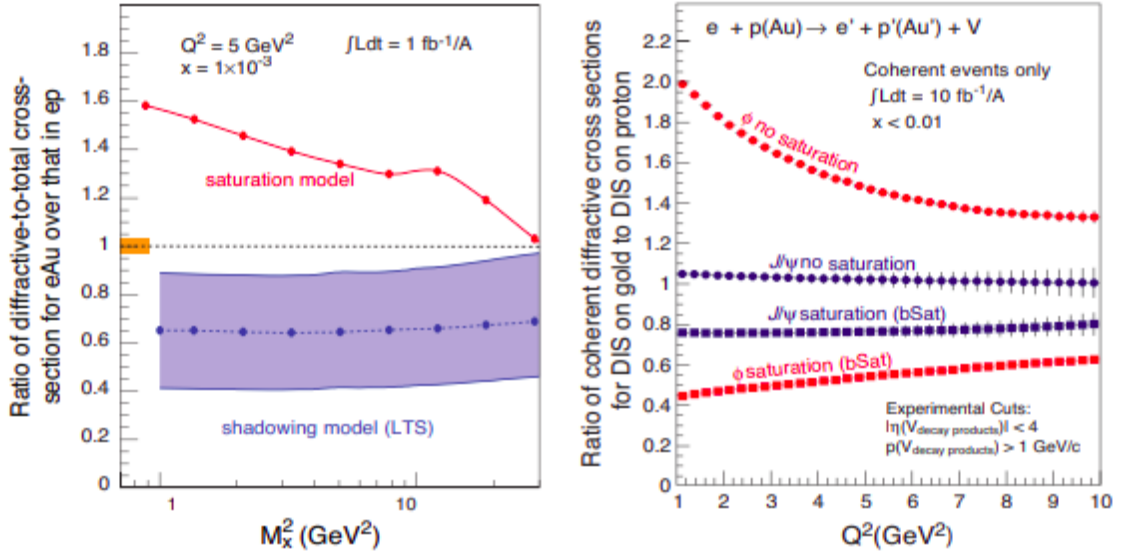an effective means to explore the properties of saturated gluon matter.

Figure 1.7: Left: The ratio of diffractive over total cross-section for DIS on gold normalized to DIS on proton plotted for different values of M_X^2, the mass squared of hadrons produced in the collisions for models assuming saturation and non-saturation. The statistical error bars are too small to depict and the projected systematic uncertainty for the measurements is shown by the orange bar. The theoretical uncertainty for the predictions of the LTS model is shown by the grey band.
Right: The ratio of the coherent diffractive cross-section in e+Au to e+p collisions normalized by $A^{4/3}$ and plotted as a function of Q^2 for both saturation and non-saturation models. The $1/Q$ is effectively the initial size of the quark-antiquark systems (ϕ and J/Ψ) produced in the medium [7].

1.5.2 The Tomography of the Nucleus

The EIC, equipped with its ability to observe diffractive and exclusive processes using different types of ion beams, will offer a groundbreaking opportunity to obtain the initial three-dimensional images of sea quarks and gluons within a rapidly moving atomic nucleus, achieving a resolution at sub-femtometer scale. For example, the EIC could obtain the spatial distribution of gluons in a nucleus by measuring the coherent diffractive production of J/Ψ in electron-nucleus scattering, similar to the case of electron-proton scattering shown in Figure 1.5.

15

1.5.3 Propagation of a Color Charge in QCD Matter

One of the primary pieces of evidence that led to the discovery of the quark gluon plasma (QGP) [15] at RHIC is jet quenching, which is characterized by a significant suppression of high-energy hadrons produced in the extremely hot matter formed in relativistic heavy-ion collisions. This suppression is attributed to the energy loss experienced by colored partons as they traverse the QGP. However, it remains puzzling that the production of both heavy and light mesons is similarly suppressed, despite the fact that heavy quarks are less likely to lose energy through medium-induced gluon radiation. EIC studies of related phenomena in well-understood cold nuclear matter can help unravel some of the unresolved mysteries concerning interactions between heavy and light quarks in hot matter. The use of various ion beams in electron-nucleus collisions at the EIC would enable the exploration and determination of the correct mechanisms through which quarks and gluons lose energy and hadronize in nuclear matter (as depicted in the schematic in Figure 1.8 (Left)).

Figure 1.8 (Right) illustrates the ratio of produced mesons in electron+nucleus and electron+deuteron collisions for both pions (light mesons) and D^0 mesons (heavy mesons), at low and high virtual photon energies ν, as a function of z, representing the momentum fraction of the observed meson carried by the virtual photon. The lines and blue circle symbols in the plot correspond to calculations assuming meson formation outside the nucleus (as depicted in the top sketch of Figure 1.8 (Left)), while the square symbols are simulated based on a model where a color-neutral pre-hadron is formed inside the nucleus (as depicted in the bottom sketch of Figure 1.8 (Left)). The position of measurements within the shaded area would provide direct insight into the meson formation process. Unlike the expected suppression in pion production across all values of z, the ratio of heavy meson production could exceed unity due to the distinct hadronization properties of heavy mesons. The discovery of such a pronounced difference in multiplicity ratios between light and heavy mesons at the EIC would contribute to our understanding of the hadronization process and the factors governing the transition from quarks to hadrons.
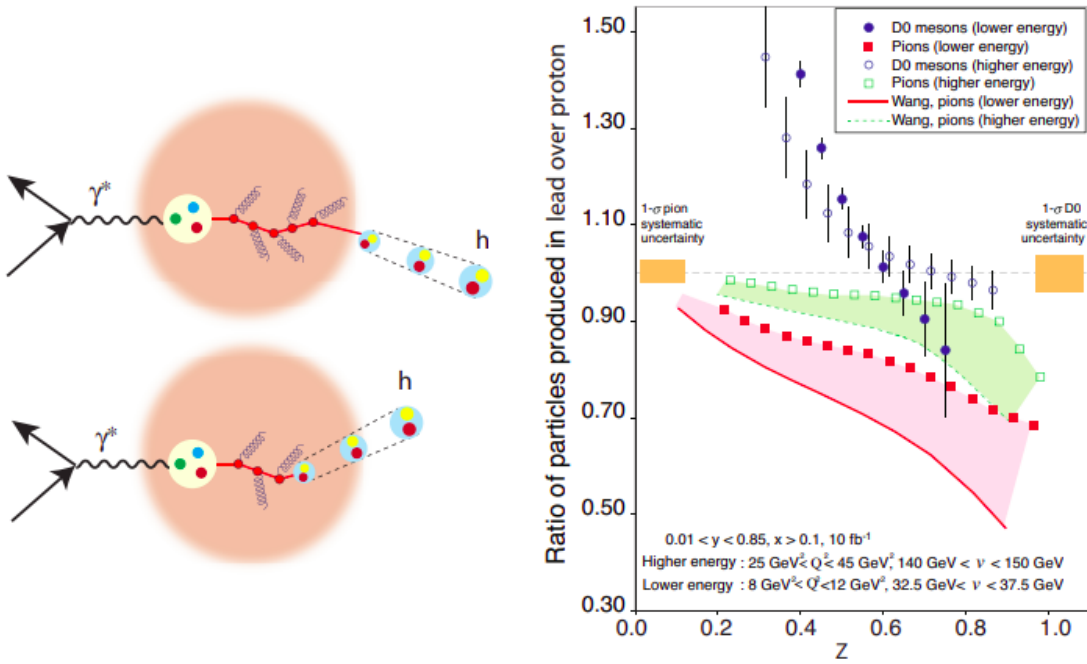
Figure 1.8: Left: A schematic illustrating the interaction of a parton moving through cold nuclear matter: the hadron is formed outside (top) or inside (bottom) the nucleus. Right: The ratio of the semi-inclusive cross-section for producing a pion (red) composed of light quarks, and a D^0 meson (blue) composed of heavy quarks in e+lead collisions to e+deuteron collisions, plotted as a function of z, the ratio of the momentum carried by the produced hadron to that of the virtual photon (γ^*), as shown in the plots on the left [7].

1.5.4 The Distribution of Quarks and Gluons in the Nucleus

The EMC [17] experiment conducted at CERN and subsequent experiments in the following decades have provided clear evidence that the distribution of quarks within a fast-moving nucleus is not simply a combination of their distributions within individual nucleons. Instead, the ratio of nuclear structure functions to nucleon structure functions exhibits a non-trivial dependence on Bjorken x, deviating significantly from unity. Particularly, there is a suppression of this ratio as x decreases, commonly referred to as nuclear shadowing. However, it is still unknown whether the same phenomenon applies to gluons. The EIC, with its broader kinematic range in both x and Q^2, has the potential to measure the suppression of structure functions at much lower values of x, approaching the region of gluon saturation. Additionally, the EIC could provide the first reliable quantification of the nuclear gluon distribution across a wide range of momentum fractions x.

1.6   Deep Inelastic Scattering

Deep Inelastic Scattering is the name given to a process used to probe the insides of hadrons (particularly the baryons, such as protons and neutrons), using electrons, muons and neutrinos. It provided the first convincing evidence of the reality of quarks, which up until that point had been considered by many to be a purely mathematical phenomenon [9].

Deep refers to the high energy of the lepton, which, thanks to its very short wavelength, is able to probe distances that are small compared with the size of the target hadron, so deep within it.

Inelastic means that the target absorbs some kinetic energy. In fact, at the very high energies of leptons used, the target is "shattered" and emits new particles.

Scattering refers to the projectile lepton's deflection. Measuring the angles of deflection gives information about the nature of the process.

1.6.1   Structure Functions

In general, the inclusive DIS process can be written as:

$$e(l) + N(p) \longrightarrow e(l') + X(p_X) \tag{1.1}$$

where e refers to the electron or positron, N is the nucleon in the initial state with momentum p, and a system X (which is not necessarily required to be measured) is produced with momentum p_X. In case of an unpolarized nucleon, the cross-section for this process can be written in terms of the structure functions F_2 and F_L in the one photon exchange approximation neglecting electroweak effects as

$$\frac{d\sigma}{dxdQ^2} = \frac{4\pi\alpha^2}{xQ^4}[(1 - y + \frac{y^2}{2})F_2(x, Q^2) - \frac{y^2}{2}F_L(x, Q^2)] \tag{1.2}$$

Instead of structure functions, the reduced cross-section σ_r is often used

$$\sigma_r = \frac{d\sigma}{dxdQ^2}\frac{xQ^4}{2\pi\alpha^2[1 + (1-y)^2]} = F_2(x, Q^2) - \frac{y^2}{1 + (1-y)^2}F_L(x, Q^2) \tag{1.3}$$

With longitudinally polarized electron and nucleon beams, it is also possible to extract the structure function g_1:

$$\frac{1}{2}[\frac{d\sigma^{\rightleftarrows}}{dxdQ^2} - \frac{d\sigma^{\rightrightarrows}}{dxdQ^2}] = \frac{4\pi\alpha^2}{Q^4}y(2-y)g_1(x, Q^2) \tag{1.4}$$

Here terms suppressed by $x^2 m_N^2/Q^2$ have been neglected, and $\sigma^{\rightleftarrows}$ refers to the case where the nucleon and electron spins are opposite (and parallel to the z axis), and $\sigma^{\rightrightarrows}$ to the scattering process in case of aligned spins. The kinematical variables x,y and Q^2 are

introduced below, and m_N is the nucleon mass and α is the fine structure constant. At large Q^2 and to leading order in the strong coupling constant α_s the F_2 structure function is proportional to the unpolarized quark and antiquark distributions in the nucleon, and g_1 is sensitive to the longitudinally polarized distributions. In this limit $F_L = 0$, and it obtains a first contribution at next to leading order in perturbative expansion, and is thus particularly sensitive to the gluon distribution. In diffractive (and also semi-inclusive) scattering, the process becomes

$$e(l) + N(p) \longrightarrow e(l') + N'(p') + X(p_X) \qquad (1.5)$$

where N' refers to the nucleon or the nucleon remnants in the final state with momentum p' and a specific system X is produced. The electron mass is neglected in the following discussion, and the nucleon mass $p^2 = m_N^2$ is kept non-zero unless otherwise stated.

p is a four vector and **p** and $\mathbf{p}_\perp$ refer to the three-momentum and the transverse momentum, respectively. The momentum vectors are illustrated in Figure 1.9 [9]..
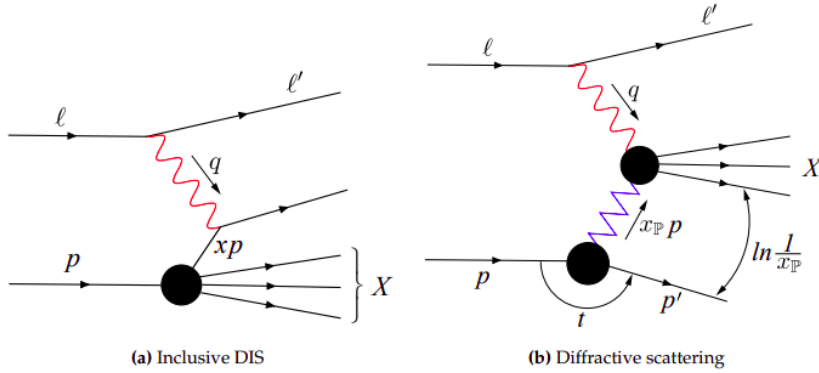

(a) Inclusive DIS   **(b)** Diffractive scattering

Figure 1.9: Kinematical variables of inclusive and exclusive DIS. The dots correspond to interactions.

1.6.2   Invariants

Let us first consider inclusive scattering where the final state X is not completely determined and the scattered nucleon (nucleon remnants) are not reconstructed. The centre of-mass energy squared for the DIS process can be written using the momenta defined in Eq. (1.1) as:

$$s = (l + p)^2 = m_N^2 + 2p \cdot l \approx 2\sqrt{E_e E_n} \tag{1.6}$$

in which E_e and E_n are the electron and the nucleon energies respectively, and the approximation is valid in the high energy limit where the nucleon mass can be neglected.

As the scattering process is mediated by a virtual photon, the center-of-mass energy W for the photon-nucleon system is generically more useful:

$$W^2 = (p + q)^2 = m_N^2 - Q^2 + 2p \cdot q \tag{1.7}$$

Here the virtual photon momentum is q = l - l' and its virtuality $-Q^2 = (l - l')^2$. The other useful Lorentz invariant quantities describing the DIS process are:

$$x \equiv \frac{Q^2}{2p \cdot q} = \frac{Q^2}{2m_N \nu} = \frac{Q^2}{Q^2 + W^2 - m_N^2} \tag{1.8}$$

$$y \equiv \frac{p \cdot q}{p \cdot l} = \frac{Q^2 + W^2 - m_N^2}{s - m_N^2} \tag{1.9}$$

These invariants have intuitive physical interpretations in particular frames. The Bjorken variable x can be interpreted in the parton model in the infinite momentum frame where the nucleon carries a large longitudinal momentum. In such a frame, x is the fraction of the nucleon momentum carried by the struck parton if the quark masses are neglected. In electron-nucleon collisions, $0 < x < 1$.

The variable y is called *inelasticity*. When expressed in the nucleon rest frame, one finds $y = 1 - \frac{E_l'}{E_l}$, where E_l and E_l' are the energies of the incoming and outgoing leptons in this frame, respectively. Consequently, $0 \leqslant y \leqslant 1$, and in particular, the highest possible photon-nucleon center-of-mass energies are reached at the y $\rightarrow$ 1 limit. A closely related variable ν also exists: $\nu \equiv \frac{p \cdot q}{m_N}$ describes, in the nucleon rest frame, the electron energy carried away by the virtual photon: $\nu = E_l - E_l'$.

The invariants presented above are not independent, and in inclusive scattering the collision kinematics is completely determined by three variables, e.g. s, Q^2 and x. This becomes apparent when noticing that the invariants defined above satisfy e.g. the following relations:

$$Q^2 = xy(s - m_N^2) \tag{1.10}$$

$$W^2 = \frac{1-x}{x}Q^2 + m_N^2 \tag{1.11}$$

The smallest kinematically allowed virtuality Q_{min}^2 can be determined if the electron mass m_e is non-zero: $Q_{min}^2 = m_e^2 \frac{y^2}{1-y}$.

Let us then discuss diffractive production of a system X with an invariant mass M_X^2. In the unpolarized case where the cross-section is symmetric in azimuthal angle, we can describe the kinematics by introducing the following new invariants:

$$t \equiv -(p'-p)^2 \tag{1.12}$$

$$x_{\mathbb{P}} \equiv \frac{(p-p')\cdot q}{p\cdot q} = \frac{M_X^2 + Q^2 - t}{W^2 + Q^2 - m_N^2} \tag{1.13}$$

$$\beta \equiv \frac{Q^2}{2q\cdot(p-p')} = \frac{Q^2}{M_X^2 + Q^2 - t} \tag{1.14}$$

In the infinite momentum frame, $x_{\mathbb{P}}$ has the interpretation that in the scattering process an exchange of vacuum quantum numbers (a *pomeron* exchange) takes place, and the pomeron carries a fraction of $x_{\mathbb{P}}$ of the nucleon longitudinal momentum. Similarly, in the partonic language β is the longitudinal momentum of the struck parton inside the pomeron. These invariants are not independent, and can be related to the invariants of inclusive DIS discussed above via e.g.

$$x = \beta x_{\mathbb{P}} \tag{1.15}$$

An experimental signature of a diffractive event is the presence of a rapidity gap between the outgoing nucleon (nucleon remnants) and the system X. This gap size is $\Delta y \backsim ln1/x_{\mathbb{P}}$ [9].

1.6.3   Laboratory Frame

In the laboratory frame the collisions are asymmetric, and the inclusive DIS invariants can be determined by measuring the energy and the scattering angle of the outgoing electron. In the limit of small nucleon mass, the invariants read

$$s = 4E_eE_n \tag{1.16}$$

$$Q^2 = 2E_eE_e'(1 - cos\theta_e) \tag{1.17}$$

$$W^2 = 4E_eE_n - 2E_e'[E_n + E_e + (E_n - E_e)cos\theta_e] \tag{1.18}$$

$$x = \frac{E_e E'_e (1 - cos\theta_e)}{2E_e E_n - E'_e E_n (1 + cos\theta_e)} \tag{1.19}$$

$$y = \frac{2E_e E_n - E'_e E_n (1 + cos\theta_e)}{2E_e E_n} \tag{1.20}$$

Here E_e and E'_e are the incoming and outgoing electron energies, and the electron scattering angle is θ_e, with $\theta_e = 0$ corresponding to the forward scattering, or photo-production region $Q^2 \approx 0$. Similarly the incoming nucleon energy is E_n. In exclusive processes it is possible to also measure the momentum of the produced particle and its invariant mass by measuring the decay products. Although the kinematical variables can be reconstructed using the scattered electron only, a common method to determine y and Q^2 is to express these invariants in terms of the scattering angles of both the electron and the produced particle using the double angle method:

$$Q^2 = 4E_e^2 \frac{sin\theta_e (1 - cos\theta_V)}{sin\theta_V + sin\theta_e - sin(\theta_e + \theta_V)} \tag{1.21}$$

$$y = \frac{sin\theta_e (1 - cos\theta_V)}{sin\theta_V + sin\theta_e - sin(\theta_e + \theta_V)} \tag{1.22}$$

Here θ_V is the scattering angle of the produced particle. These expressions are again valid in the limit where the nucleon mass can be neglected. Note that once Q^2 and y are determined, x and W^2 can be obtained using Eqs. 1.10 and 1.11.

The squared momentum transfer t can be written as

$$t = -\frac{(\mathbf{px}_\perp - \mathbf{l}'_\perp)^2 + x_{\mathbb{P}}^2 m_N^2}{1 - x_{\mathbb{P}}} \approx -(\mathbf{px}_\perp - \mathbf{l}'_\perp)^2 \tag{1.23}$$

Here $p_{X\perp}$ is the transverse momentum of the produced particle and $\mathbf{l}'_\perp$ the transverse momentum of the scattered electron, and the approximation is valid at high energies where x_P is small and the momentum transfer is approximatively transverse. Note that the kinematical lower bound for t reads

$$-t > -t_{min} = \frac{x_{\mathbb{P}}^2 m_N^2}{1 - x_{\mathbb{P}}} \tag{1.24}$$

When t, Q^2 and W^2 are determined, $x_{\mathbb{P}}$ can be obtained by using Eq. 1.13.

In exclusive and semi-inclusive processes the particle X is identified by measuring the invariant mass of the decay products. In inclusive diffraction the invariant mass M_X^2 is determined by measuring the total energy E_X and the total momentum p_X of the produced particles:

$$M_X^2 = E_X^2 - \mathbf{px}^2 \tag{1.25}$$

In these events, it is also possible to construct inelasticity using the hadron method

$$y_h = \frac{E_X - \mathbf{px}_z}{2E_e} \qquad (1.26)$$

The hadron method can also be used to determine inelasticity in exclusive particle production in the photoproduction limit where the scattered electron cannot be detected. Generically in inclusive diffraction $M_X^2 + Q^2 \gg |t|$, and consequently t can be neglected when determining $x_{\mathbb{P}}$ and β using Eqs. 1.13 and 1.14. [9].

1.6.4 Breit frame

A natural frame to describe hard scattering process in DIS is the Breit (or brick wall) frame, where the incoming photon carries no energy, and the parton to which the photon couples to behaves as if it bounced off a brick wall. Let us choose that the ultrarelativistic nucleon moves along the positive z axis, and the photon propagates to the -z direction. The nucleon momentum in this frame is $p_z = \frac{1}{2x}Q$, and the parton longitudinal momentum k_z can be written as $k_z = xp_z = \frac{1}{2}Q$. Similarly, the photon four-momentum reads $q = (0,0,0,-Q)$. Now, after the photon absorption $\mathbf{k}' = -\mathbf{k}$, where $\mathbf{k}'$ is the parton momentum after the scattering. Note that in this frame there is no energy transfer to the proton. The Breit frame is not the center-of-mass frame for the parton-photon scattering. This is advantageous when separating the produced particles from the beam remnants. In the Breit frame, the produced particles populate the region of negative z momentum, while the beam remnants generically have a positive momentum z component.
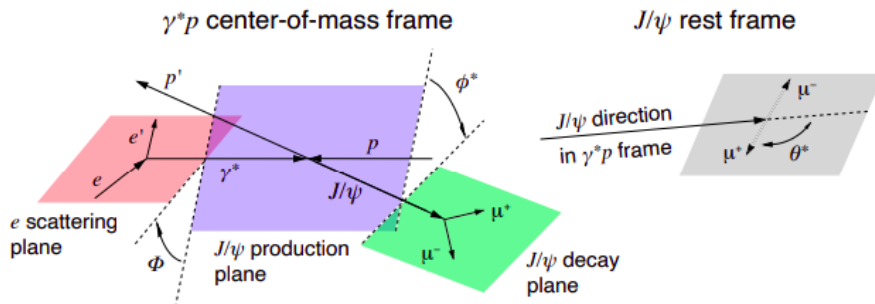

Figure 1.10: Planes in exclusive vector meson production.

Chapter 2

EIC Project

The EIC is an upcoming accelerator project that is set to be one of the largest and most sophisticated ones built in the coming decades. Its exceptional design luminosity and polarized beams will enable it to tackle significant unresolved issues in our understanding of the fundamental nature of matter.

2.1   The ePIC Reference Detector

To access the physical observables outlined in Section 1.3 and utilize theoretical calculations, the EIC detectors play a vital role. These measurements necessitate the use of large, advanced, and distinctive instruments. The experience gained from the first $e + p$ collider facility, HERA at DESY, Germany, and the advancements in detector concepts over the past few decades since the initiation of $e + p$ collisions at HERA in 1992 have greatly contributed to this objective.

The detectors will be situated at the interaction regions where the electron and ion beams are expected to collide. Since space is limited in these regions due to the requirements of high luminosity, the EIC detectors need to be positioned there. They must possess robust integration of forward and backward detectors, as well as multiple hermetic functionalities such as precise energy measurement, particle tracking, and identification. These capabilities are essential for determining the energy-momentum four-vector of final state particles across a wide energy range, spanning approximately 10 MeV to 10 GeV.

In addition to the main detector facilities, specific instrumentation will be crucial for conducting the scientific program. Special purpose detectors located close to the beams will be used to determine the collision luminosity. Moreover, for spin-dependent measurements, precise knowledge of the polarizations of the electron and ion beams is essential, which is achieved through the use of special purpose polarimeters.

The design of the EIC detectors revolves around solenoidal superconducting magnets

with bipolar fields. This can be accomplished either by modifying the BABAR/sPHENIX magnet at 1.5 T or by constructing a new superconducting magnet with a similar magnetic field strength. The solenoidal configuration naturally lends itself to tracking, vertexing, particle identification, and calorimetry systems organized in a configuration with barrel and end cap detectors. These detectors must be designed to operate with high efficiency in the presence of a substantial background generated by the intense circulating beams as they pass near the detectors.

Unlike symmetric *ee* and *pp* colliders, the EIC's asymmetric collisions result in unique detector requirements. The hadron endcap, barrel, and electron end cap detector systems observe distinct distributions of particles in terms of both momentum and particle types. Consequently, the performance requirements for these detector systems vary significantly between the different regions of the detector.

Accurately reconstructing event and particle kinematics (x, Q^2, y, W, p_t, z, Φ, θ) is crucial for measuring the various physics processes at the EIC. These variables, defined in Section 1.6, play a vital role in the analysis. The important variables x, Q^2, y, and W can be determined either from the scattered electron or from the final hadronic state. To explore the complete x-Q^2 plane at different center-of-mass energies and with significantly asymmetric beam energy combinations, the detector needs to be capable of reconstructing events across a wide range of rapidity. This places requirements on both the acceptance and resolution of the detector. At the EIC, it is essential to have good coverage of the rapidity range ($|\eta| > 2$) to avoid missing a significant portion of the x-Q^2 phase space. Therefore, particular attention is given to the design of the lepton and hadron end-caps to ensure comprehensive coverage.

Figure 2.1 demonstrates the relationship between pseudo-rapidity, scattering angle, and the x-Q^2 phase space for the detector components in the interaction region. The central detector, covering approximately $|\eta| < 1$, is known as the barrel detector. The forward end-cap, covering hadrons, and the backward end-cap, covering electrons, complete the setup. Additionally, there are very small angle counters situated at a greater distance from the interaction point, forming the very forward and very backward detectors. Geometrical acceptance is not the only factor to consider, as there are other constraints specific to high-energy particles in the forward region. These include the minimum detectable particle momentum, transverse momentum acceptance, and momentum resolution. These limitations can be addressed by adjusting the magnetic field values through different settings of the central solenoid. To facilitate the EIC physics program, ancillary systems such as the luminosity monitor and lepton and hadron polarimeters are also necessary. The proposed general-purpose detector, which is still in the conceptual stage, incorporates a range of equipment technologies capable of meeting the majority of EIC requirements. These technologies have been extensively studied and form the basis of a detector design that can serve as a reference for the project[8].
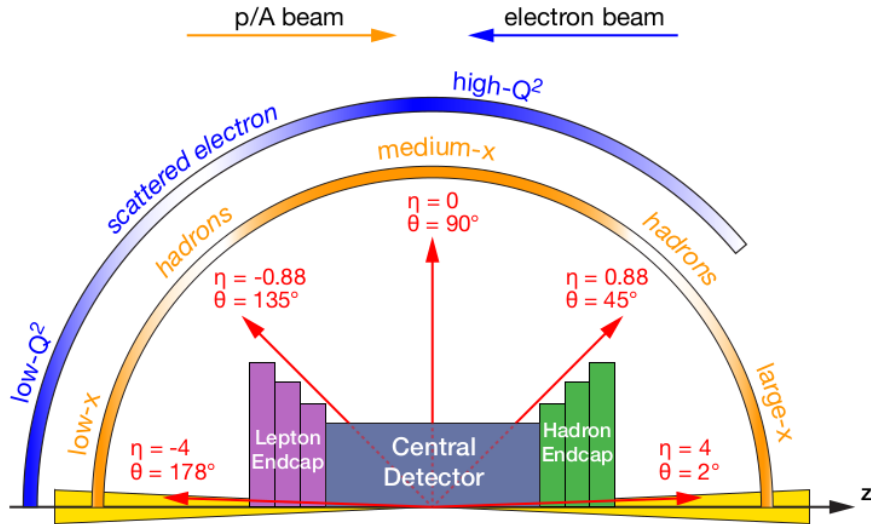
Figure 2.1: A schematic showing how hadrons and the scattered lepton for different x–Q^2 are distributed over the detector rapidity coverage [8].

2.1.1 General EIC Detector Considerations

From the experimental point of view, the broad physics EIC program can be accomplished by the study of
(I) inclusive,
(II) semi-inclusive and
(III) exclusive processes,
all of them with an initial state of electrons and light or heavy nuclei, with polarized electron and light nuclei beams and spanning a wide range of center of mass energies. The main requirements for the experimental apparatus are based on these processes and the requirements of the wide kinematic coverage, adding more and more complexity moving from reactions described in point (I) to (III) [8]:

- Precise identification of the scattered electron and fine resolution in the measurement of its angle and energy are a key requirement for all experimental channels; other essential tools for the whole physics scope are the central magnet and the tracking system required for momentum measurements and full rapidity coverage with electromagnetic and hadronic calorimetry;

- More is needed to access the semi-inclusive processes (II): excellent hadron identification over a wide momentum and rapidity range, full 4π acceptance for tracking and momentum analysis and excellent vertex resolution by a low-mass vertex detector;

27

- Exclusive reactions (III) impose the necessity to accurately reconstruct all particles in the event using a tracker with excellent space-point resolution and momentum determination, electromagnetic calorimetry with excellent energy resolution, hadronic calorimetry in the end-caps, the complete hermeticity of the setup with the additional requirement of very forward detectors such as Roman pots (cylindrical vessels that can house the detectors), and large acceptance zero-degree calorimetry to effectively detect neutrons from the breakup of nuclei or neutral decay products from tagged DIS processes;

- For the entire experimental program a precise determination and monitoring of the luminosity will be essential;

- Measurements with polarized beams require the use of electron, proton, and light nucleus polarimeters;

- The strategy for detector read-out and data acquisition has to be defined taking into account the data rate of the experiment, as well as the rapid developments in the field of digital electronics and computing power, suggesting an integrated approach to both the read-out and data acquisition and software and computing.

A reference central detector design, largely matching the physics requirements, is presented as a 3D model in Figure 2.2 and in 2D schematic form in Figure 2.3
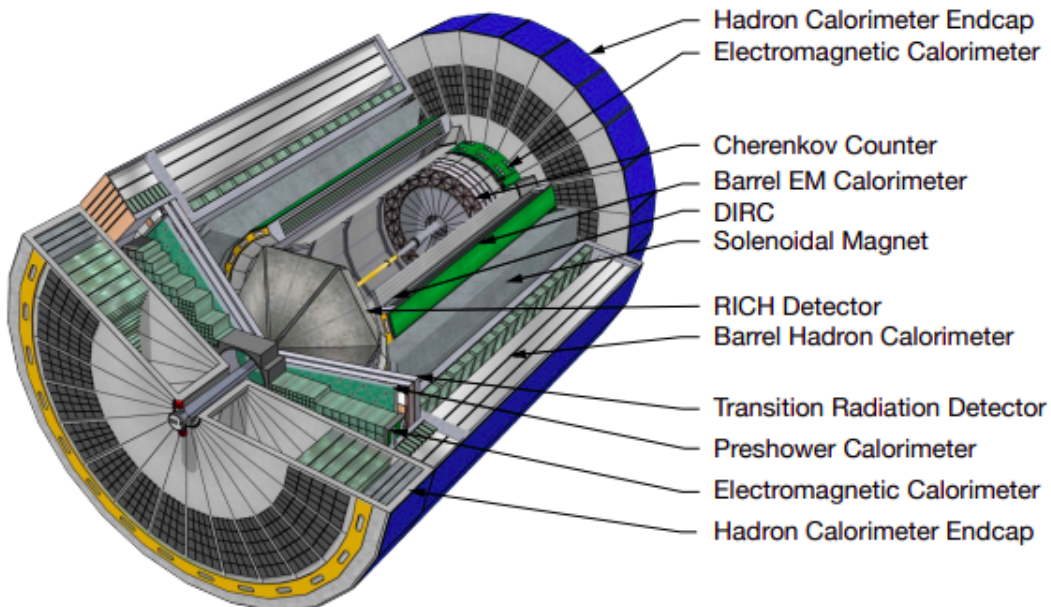

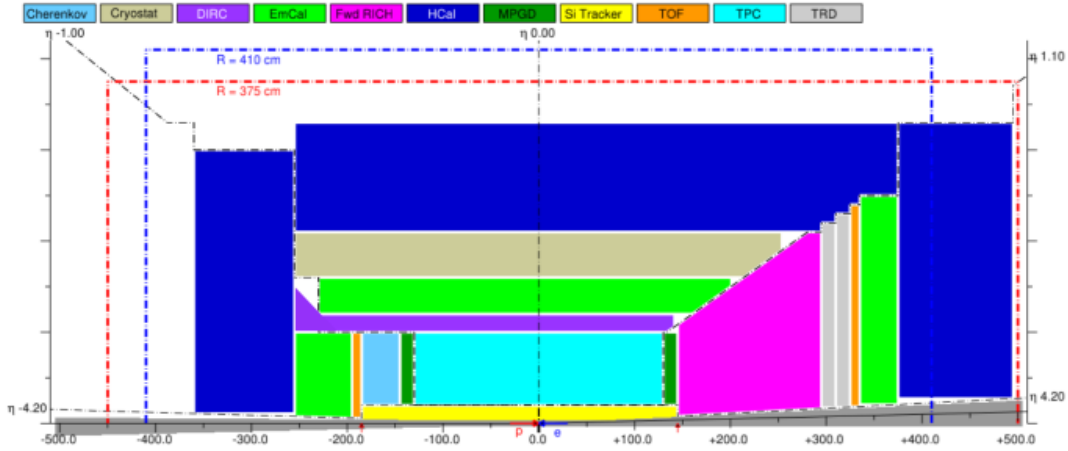Figure 2.2: Illustration of a generic EIC concept detector [8].

28

Figure 2.3: A 2D sketch of an EIC detector layout, horizontal cross cut. The beam pipe footprint (in dark gray) is to scale. The blue dashed line shows the doorway size between the assembly and the installation halls. The red dashed line shows the realistic central detector envelope with the available [-4.5, 5.0] m space along the beam line[8].

The following characteristics are assumed:

The central detector instruments the pseudo-rapidity region $-4 < \eta < 4$ with full coverage of the range $|\eta| < 3.5$. This acceptance range matches the needs of the inclusive, semi-inclusive, jet physics and spectroscopy studies. It is complemented by the very forward and backward detectors ensuring the hermeticity and the forward tagging required by specific topics of the physics program, in particular exclusive reactions and diffractive channels. The main requirements of the central detector are dictated by the event geometry and the physics program. They are related to [8]:

(I) tracking and momentum measurements
(II) electron identification, (III) hadron identification and (IV) jet energy measurements, while (V) the overall detector size is imposed by collider design considerations:

1. Very fine vertex resolution, at the 20 μm level for the three coordinates, is needed, while a moderate momentum resolution around 2% for $p_T > 0.1$ GeV/c matches the physics requirements; in the reference detector this is obtained with Si vertexing surrounded by a TPC and completed by disc-shaped detectors in the forward and backward regions;

2. The purity requirements for electron/hadron separation are at the 10^{-4} level in the backward and barrel region and, for this reason, the figures for the electron energy resolution are very p demanding, in particular in the backward region where an r.m.s. of $2\%/\sqrt{(E)}$ is needed, in the reference detector this is realized by

29

PbWO$_4$ (PWO) crystals; in the same direction, provided the requested light collection system, and the material budget should not exceed 5% X_0 in front of the electromagnetic calorimeter;

3. The identification of the different hadron species in the whole central detector coverage, namely for hadrons with momenta up to 50 GeV/c, is 3σ π/K separation over the whole range as a reference figure. In the reference detector this is obtained with various technologies: a focusing aerogel RICH in the backward arm, a high performance Detection of Internally Reflected Cherenkov light (DIRC) in the barrel, a dual RICH with aerogel and fluoro-carbon gas in the forward arm;

4. The measurement of the jet energy in the forward direction is a necessity, a resolution of the order of $50\%/\sqrt{(E)}$ is required to match the needs. Sampling calorimeters with ion converter are assumed in the reference detector;

5. The detector extension along the beam lines impacts on the required length around the IP that has to be kept free of machine elements, typically referred to as L*. The reference figure is [-4.5, 5.0] m space along the beam line, assuming the iteration point at zero.

2.1.2 Detector Challenges & Performance Requirements

Beam Energies, Polarization, Versatility, Luminosities

The goal of the EIC is to achieve a level of comprehension of the inner workings of the proton and complex atomic nuclei that is akin to our understanding of the electronic structure of atoms. Unlike the distinct separation of interactions and structures in molecules and atoms, protons and other types of nuclear matter exhibit a intertwined mixture where these elements cannot be easily distinguished. As a result, the observable characteristics of nucleons and nuclei, such as mass and spin, arise from the intricate dynamics of this interconnected system.

The EIC can uniquely address three profound questions about nucleons and how they are assembled to form the nuclei of atoms, such as:

- How does the mass of the nucleon arise?

- How does the spin of the nucleon arise?

- What are the emergent properties of dense systems of gluons?

These questions can be answered by an EIC with highly polarized beams of electrons and ions, with sufficiently high luminosity and sufficient, and variable, center-of-mass energy.

This confirms the accelerator requirement of a large luminosity, 10^{33-34} cm^{-2}s^{-1} over a

large range of center of mass energies, between 20 and 140 GeV, high electron and (light) ion beam polarizations of above 70%, and a large range of accessible ion beams, from deuterium to the heaviest nuclei (uranium or lead).

The successful outcome of the EIC depends on:

1. the luminosity,

2. the center-of-mass energy and its range,

3. the lepton and light ion beam polarization, and

4. the availability of ion beams from deuteron to very heavy nuclei

Integrated Detector and Interaction Region

The scientific objectives of the EIC necessitate specific requirements for both the accelerator and the detectors. Since all particles in the final state contain valuable information about the 3D structure of nuclear matter and the emerging phenomena, it is crucial to design the interaction region and the detector at the EIC in a way that enables the identification and measurement of all particles with as close to 100% acceptance as achievable, while maintaining the necessary resolutions.

The fundamental physics process at the EIC is Deep Inelastic Scattering (DIS), as discussed in section 1.6. In this process, an ion consisting of nucleons, which in turn comprise partons such as quarks and gluons, travels in one direction and interacts with an electron moving in the opposite direction. The electron undergoes a hard collision with a parton inside the ion. Based on the final state, we can categorize the particles into three classes:

1. The scattered electron,

2. Particles associated with the initial state ion, and

3. Particles associated with the struck parton

Achieving high acceptance in the forward regions of a collider is challenging due to the necessary accelerator elements for delivering colliding beams. The luminosity at the interaction point is inversely proportional to the distance between the nearest quadrupole magnets, which affects the acceptance for forward particles. The closer the beam elements are to the interaction point, the more they obstruct acceptance at shallow angles relative to the beam axis, particularly for particles associated with the initial state ion.

To address these challenges, a unique and innovative integration of the detector in the interaction region is required, extending beyond the main detector over a large region

(approximately ± 40 m). The central detector region of the EIC, similar to traditional collider detectors, is designed to measure the final state particles resulting from the hard collision between the electron and the parton in the ion. It is divided into three sections: the Electron-endcap, the Hadron-endcap, and the Barrel, corresponding to different regions in x and Q^2 for the scattered electron.

In addition to determining x and Q^2, the central detector aims to measure two transverse kinematic variables (transverse momentum and impact parameter) and identify the flavor of the partonic collision, which are crucial for the 3D QCD nucleon and nuclear structure program of the EIC. Precise identification and measurement of single hadrons among the particles associated with the scattered partons are also required.

There are two types of forward final state particles that need to be reconstructed. The first type consists of particles resulting from interactions in which the beam particle receives a large transverse momentum boost and fragments into multiple parts. These particles quickly separate from the beam and exhibit different kinematics and charge-to-mass ratios. The second type includes beam particles that remain intact during the collision, lose a small fraction of their longitudinal momentum, and acquire a small transverse momentum.

To detect and analyze these forward final state particles, a highly-integrated extended "far-forward" detector region is situated downstream of the ion beam, covering approximately 30 m. This region, combined with the central detector, provides nearly complete coverage for final state particles associated with the incident ion-beam particle.

Similarly, the "far-backward" detector region, located along the outgoing lepton beam, is highly integrated to capture measurements close to the beam line in the electron-beam direction. This enables monitoring of the luminosity and enhances the low-Q^2 coverage of the detector. Electron-ion collisions, where the electron is scattered at a very shallow angle, correspond to cases where the exchanged photon is nearly real. These photo production processes are of interest on their own and can also facilitate a program of hadron spectroscopy.

To advance our understanding of 3D QCD nuclear and nucleon structure and explore new states of QCD at the EIC, it is crucial to have a large acceptance (near-100%) not only in the central region but also in the regions close to both the ion-beam and electron-beam directions. Hence, a total acceptance detector is necessary.

Rate & Multiplicity

The EIC total e+p cross-section is estimated using the PYTHIA6 [18] event generator. For each collision, Figure 2.4 shows the particle production rates for the 20 GeV on 250 GeV beam energy configuration. Events were simulated using PYTHIA6, and the total cross section reported by PYTHIA6 was used to scale event counts to rates. No cuts, for example on event Q^2 or particle momentum, were applied. The η range spans the expected acceptance of the main EIC detector. The term "charged" on the plot refers to

electrons, positrons, and charged long-lived hadrons, while "neutral" refers to photons, neutrons, and K_0^L. The EIC detector response to the collisions and the data rate were studied using full detector GEANT 4 simulations of a generic EIC detector model [1417, 1419]. The subsystem multiplicity distributions and the average data rate are studied in a simulation combining the EIC tune of PYTHIA6, which samples ≈ 50 μb of the e+p collision cross section, and the full detector GEANT simulation. At the top instantaneous luminosity of 10^{34} cm^{-2} s^{-1}, the collision-induced zero-suppressed streaming data rate from EIC collisions is around 100 Gbps, which is the minimal amount of raw data that has to be recorded to disk in order to record all minimum-bias EIC collisions in the central detector without the assumption of online reconstruction and reduction.
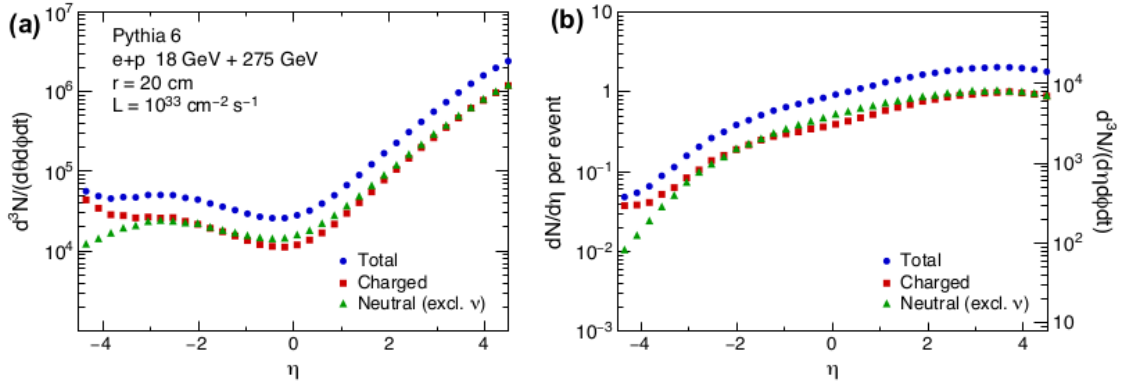

Figure 2.4: Particle production rates as a function of pseudo-rapidity at EIC for 18 GeV on 275 GeV e+p collisions and a luminosity of 10^{-33} cm^{-2} s^{-1}.
Particles per second per unit (ϕ, θ) - the η-dependent flux at a distance of 1m from the interaction point (left).
Mean numbers of particles per event (left axis) and particles per second per unit (η, ϕ) (right)[8].

Backgrounds

The combination of the relatively low signal rate of the EIC collisions and the requirement for demanding systematic control for EIC measurements calls for low background and detector noise at an EIC experiment. In turn, the types and levels of backgrounds are one of the main considerations on the detector design and it is a major consideration for IR integration, such as the arrangement of the beam magnets as well as other beam parameters and optics [8].

1. Ionization radiation dose and neutron flux from the EIC collisions
   The ionization radiation dose and neutron flux from the e+p collisions are studied

using EICROOT and a generic EIC detector model in the RHIC IP6 experimental hall. The simulation is generated with the EIC tune of PYTHIA6 with 20×250 GeV beam energy and is based on the GEANT 3 package with the HADR = 5 option. As shown in Figure 2.5, the near-beam-line regions experience relatively high ionizing radiation. The above-100 keV neutron flux is shown in Figure 2.6. The near-beam-line regions, in particular the vertex tracker and the forward-backward calorimeters also experience relatively high neutron flux, exceeding 10^{10} neutrons/cm^2 per year from the e+p collisions at the top luminosity (10^{-34} cm^{-2} s^{-1}).
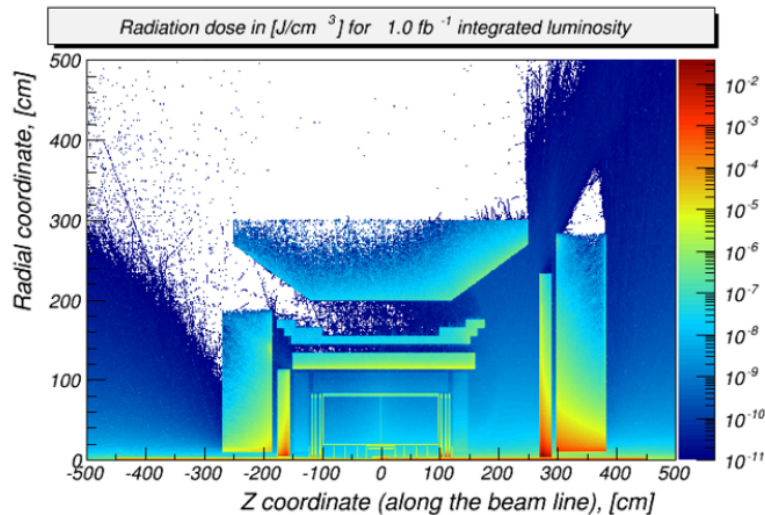
Figure 2.5: Ionizing radiation energy deposition from e+p collision at s ep = 140 GeV studied using the BeAST detector concept, which also applies to the reference EIC detector[8].

2. Synchrotron radiation

Various sources of synchrotron radiation could have an impact on the background level at the IP. When the trajectory of a charged particle is bent, synchrotron photons are emitted that are tangential to the particle's path. Bending and focusing of the electron beam is the main cause of synchrotron radiation within the IR. It is important to place the IP far away from strong bending magnets in the arcs to minimize synchrotron radiation. The tracking detectors in the central detector as well as the calorimeter have to be properly shielded against synchrotron radiation, therefore a number of absorbers and masking must be applied along the electron beam direction. Synchrotron radiation also deposits several kilowatts of power into the beam pipe in the central detector region, which must then be cooled. Addi-
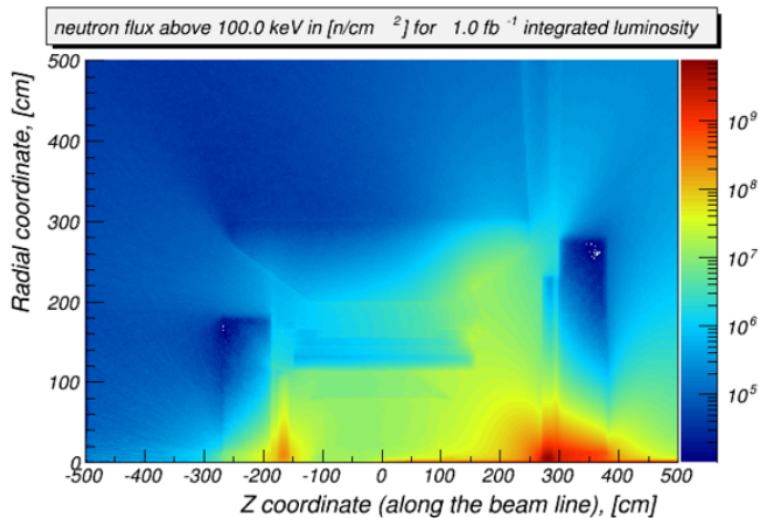
Figure 2.6: Neutron flux from the e+p collision at $\sqrt{s_e p} = 140$ GeV studied using the BeAST detector concept with the assumed location in the RHIC, located/placed in the RHIC IP6 experimental hall[8].

tionally, synchrotron radiation can degrade vacuum quality by causing material desorption from vacuum chamber walls and/or heating residual gas. This radiation is also a direct and indirect source of background in the luminosity monitor, and low-Q^2 tagger located on the downstream electron side of the IR. However, background from the contribution from the upstream electron beam scattering off residual gas must still be assessed.

Figure 2.7 shows a view of the upstream electron beamline and IP, with synchrotron radiation generated by the last upstream dipole and FFQ quadrupoles. Electrons enter from the lower left on the figure, at the location of the last dipole, ≈ 40 m from the IP. The IP itself is obscured by the hourglass shape of the central region of the beam pipe.

3. Beam-gas interactions
Beam-gas interactions occur when proton or ion beam particles collide with residual gas. Ion beam interactions with gas cause beam particle losses and halo, which reach detectors. This is an important source of neutrons that thermalize within the detector hall. The large synchrotron radiation load could heat the beam pipe and residual gas particles from the beam pipe walls could be released, which would lead to a degradation of the vacuum. A crossing angle and short section of shared beam pipe in the EIC design minimize the beam-gas problem. A model of the interaction region-1 (IR1), $\pm$ 30m, including all magnets, the tunnel walls, the
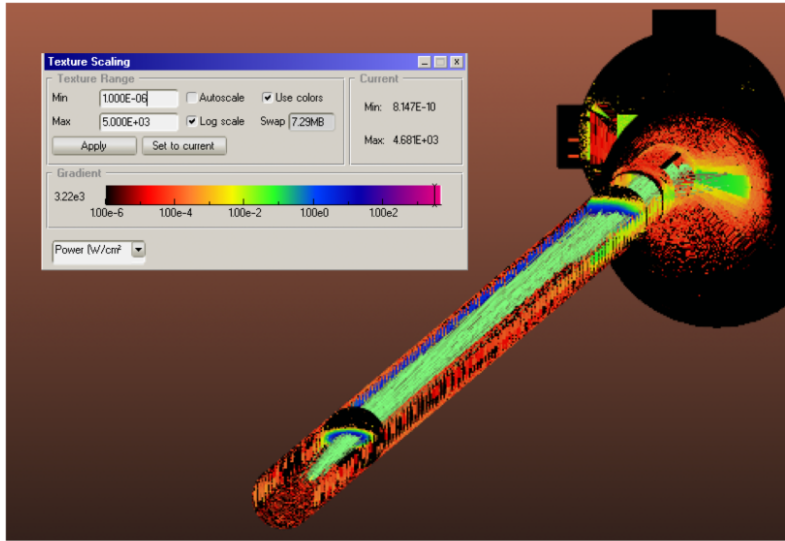
Figure 2.7: SYNRAD [20] generation of synchrotron radiation from 0.260 A of 18 GeV electrons. The color scale is logarithmic, with blue approximately 1 W/cm^2 . Electrons enter from the lower left in the figure, the initial radiation fan is generated from the last dipole, at approximately 40 m upstream of the IP. Individual photons are traced by the green lines. The vertical striations on the beam pipe result from the sawtooth inner profile of the pipe, which ensures photons hit the wall locally head-on [8].

detector cavern, and a simplified representation of the detector have been created in FLUKA. This is illustrated in Figure 2.8.
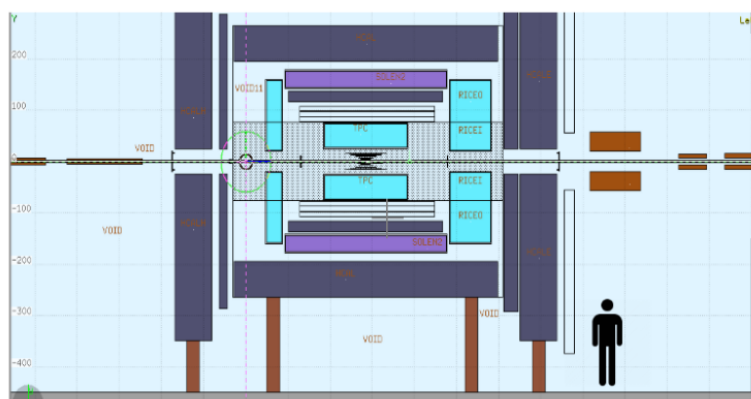

Figure 2.8: Elevation view of the FLUKA model of the EIC Detector. The Si Vertex Tracker (SiVT) in this rendition includes six layers[8].

36

The energy spectrum of beam-gas induced neutron at the central Si Vertex Tracker (SiVT) is illustrated in Figure 2.9. The energy distribution shows a clear peak of fully thermalized neutrons below 1 eV, as well as a knee around 10 MeV from evaporation neutrons. Neutron damage to Si sensors occurs primarily via displacement of nuclei from their ideal lattice positions. This can happen both by direct nSi scattering, and also by recoil from Si (n,γ) reactions. The latter can dislodge nuclei, even for neutron energies well below 1 eV.
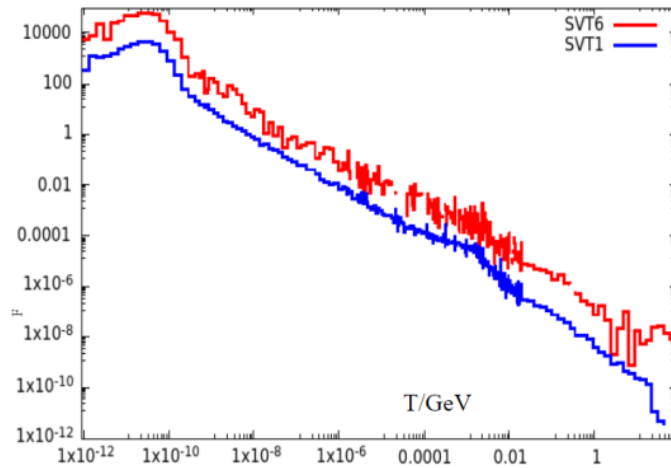

Figure 2.9: Neutron energy spectra from FLUKA simulations in two layers of the SiVT : (1) Outer-most Si layer (SVT1) and (2) Inner-most Si layer (SVT6). The vertical scale is fluence in units of neutrons/GeV/sr/cm^2/proton at pressure P$_F$ = 100 mbar. The horizontal scale is neutron energy in GeV. Absolute realistic flux in neutrons/s/sr/cm^2/GeV is obtained by multiplying the vertical axis by $6.25 \cdot 10^7$ protons/s [8] (see Figure 2.10 caption).

The damage induced by neutrons is frequently quantified by an equivalent flux of 1MeV neutrons. This is shown in the lower panel of Figure 2.10.

It is possible to further estimated the data rate across the whole experiment that originated from the beam-gas interactions. The full detector simulation model is used to simulate the proton beam hydrogen gas interaction generated with PYTHIA8 in the p + p fixed-target configuration. The hydrogen gas pressure is assumed to be a constant 10^{-9} mbar across the experimental region $|z| < 450$ cm, which leads to approximately 10 kHz inelastic beam gas interaction rate. The result collision is propagated through the detector model as illustrated in Figure 2.11. The result data rate is summarized in Figure 2.12.

4. Beam halo
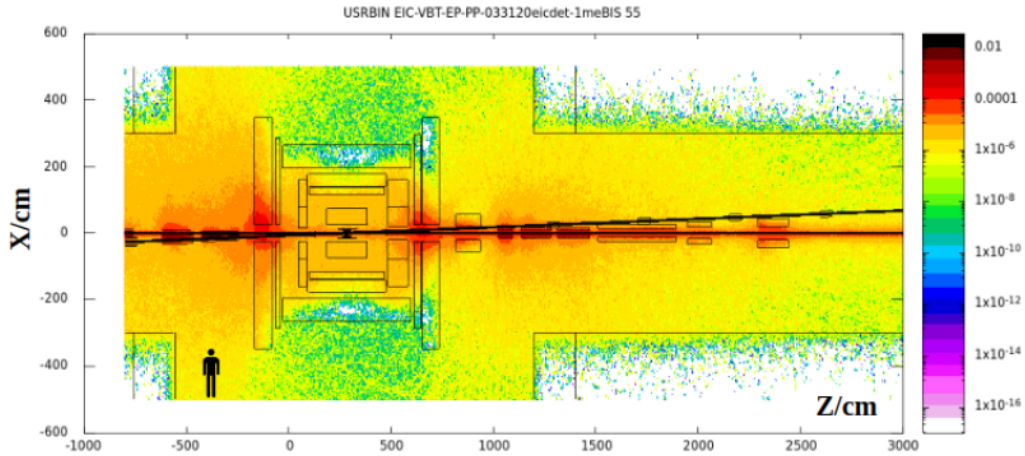Particles produced in elastic collisions of both electron and proton beams with

Figure 2.10: Map for 1-MeV-equivalent Neutron fluence from p + Air interactions in the beam pipe at proton energy E p = 275 GeV and an artificial pressure PF ("P-FLUKA") in a thin cylinder along the beam line. The IP is located at Z = 285 cm. Neutron fluence is given by the color chart at the right side of the plot in units of neutrons/cm^2/proton at PF = 100 mbar [8].
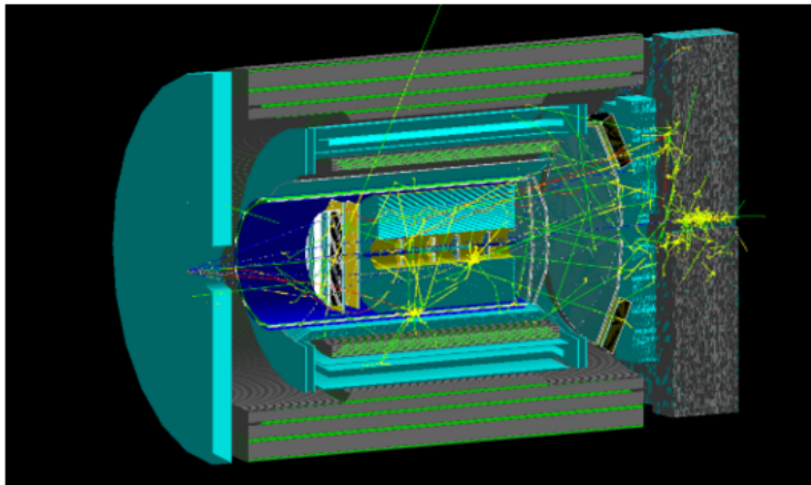

Figure 2.11: GEANT4 simulation of a beam gas interaction background in an EIC detector model. The interaction originate after the last focusing magnet at $z = 4m$. The produced particle shower will cascade through the central detector stack and induce high multiplicity background throughout the forward and backward spectrometers[8].

residual gas or beam-beam interactions can form a halo distribution around the beam. There also can be halo muons produced in inelastic p-A collisions. Often
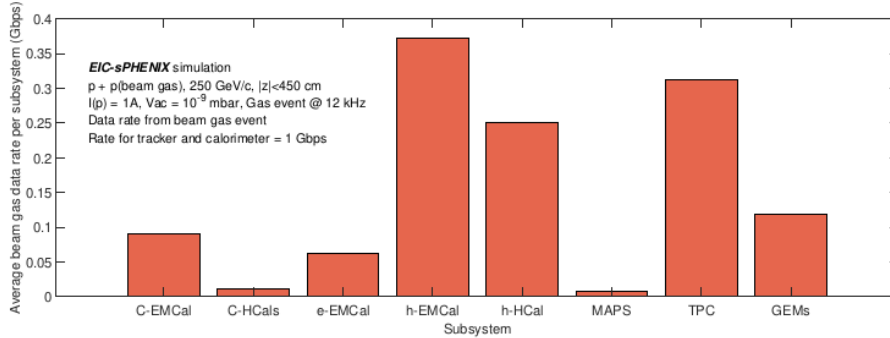
Figure 2.12: Signal data rates from tracking and calorimetric detectors from beam gas col- lisions via full detector GEANT 4 simulation of a detector concept based on sPHENIX, which also apply to the reference EIC detector as in this report. This simulation assumes constant 10^{-9} mbar vacuum in the experimental region of $|z| < 450$ cm, which would be modified with a dynamic vacuum profile in the future[8].

the result is an on-momentum electron or ion with large scattering angle. These particles can then generate additional background by interacting with the beam pipe and can impact the stability of the beam. Beam halos are being studied to determine whether "scraping" the halo with collimators is required, as well as proper placement of those collimators.

2.2 Detector Concepts

2.2.1 Tracking and Vertexing Detector Systems

The tracking and vertexing systems being considered for the EIC utilize both semiconductor and gaseous tracking detector technologies, and there are also detectors that combine these technologies. In the semiconductor detectors, electron/hole pairs are collected when charged particles pass through silicon-based sensors. To meet the requirements of high tracking and vertexing resolution (better than 5 μm for tracking and around 3 μm for vertexing), these detector systems need to have high granularity while keeping the material budget low (below 0.8% in the barrel and 0.1% in the endcap) relative to a radiation length. Monolithic active pixel sensors (MAPS) have evolved from the 180 nm technology used in STAR and ALICE to the 150/180 nm Depleted MAPS (D-MAPS), and a third-generation 65 nm process is currently being developed jointly by the EIC and ALICE ITS3 vertex tracker upgrade.

In gaseous tracking chambers, the ionization created by particle tracks drifts to anode planes located in the endcaps, where it is collected, potentially with additional amplification. The sPHENIX experiment is constructing a double-sided time projection chamber (TPC) that features a central cathode plane and gas amplification modules in the endcaps, which could be modified for use at the EIC. Upgrades to the read-out pads for the EIC would focus on micro-pattern gaseous detectors such as gas electron multipliers (GEMs), μMEGAs, or μRWELL, which can amplify the electrons before they are read out on high granularity anode printed circuit boards. Gaseous tracking detectors also assist in particle identification by utilizing information on ionization energy loss.

Two primary concepts for tracking detectors are presented. The first option is an all-silicon tracking detector, consisting of barrel and endcap silicon detectors, which can be implemented in a compact form. The second option is a hybrid tracking system that combines a silicon vertex detector within a TPC, providing dE/dx measurements that aid in particle identification. In both options, alternative tracking possibilities exist in the backward and forward tracking endcaps. [8].

2.2.2 Particle Identification Detector Systems

The second major detector system is designed to distinguish electrons from pions, kaons, and protons, achieving significant pion/electron suppression and better than 3σ π/K/p separation across all rapidity regions. The use of specific ionization (dE/dx) in time projection chambers with specific gas mixtures enables improved resolution that approaches the limit of Poisson statistics. However, specialized particle identification detectors based on Cerenkov light emission and time of flight measurements are necessary.

Cerenkov detectors detect light emitted by particles traveling faster than the speed of light in a gas, aerogel, or quartz radiator medium. Integration with the tracking system is

essential, as the originating track must be accurately known. Different radiator media are required in the electron endcap, barrel, and hadron endcap due to the varying momentum ranges of the particles detected in those regions.

A hadron blind detector, which lacks focusing and utilizes Cesium-Iodide (CsI) photocathodes evaporated on GEMs [23], can effectively separate electrons from hadrons. A similar approach with focusing is employed in the CsI ring imaging Cerenkov (CsI RICH) detector. Novel techniques using nano diamond powder instead of CsI are also being considered. Another option is the dual RICH (dRICH) with both gas and aerogel radiators, which overcomes performance limitations associated with Cerenkov thresholds. The modular RICH (mRICH) concept employs a Fresnel lens for focusing. Additionally, the measurement of internally reflected Cerenkov light (DIRC) is being explored for a high-performance DIRC (hpDIRC), which would outperform the DIRC detectors at BaBar[25] and PANDA[22].

Various other particle identification technologies are also under development. Time-of-flight particle identification at low momentum can be achieved through precise timing measurements using large area picosecond photon detectors (LAPPD[24]) in the endcaps. GEM transition radiation detectors (GEM-TRD) combined with neural networks have demonstrated the ability to separate electrons and pions.

Based on these particle identification technologies, several combined concepts are proposed. In the forward direction, a gas-based Cerenkov detector is included but requires another technology such as the dRICH, which will be further explained in sections 2.4 and 3.1. In the central region, a combination of the DIRC and time-of-flight (TOF) detectors needs to be supplemented by ionization loss measurements in the hybrid tracking detector system or other identification technologies in the more compact all-silicon tracking detector system. In the backward or rear direction, several options fulfill the requirements, including the mRICH with LAPPD. [8].

2.2.3 Calorimeter Detector Systems

The third major detector system focuses on calorimetry, which measures particle energy and includes both electron and hadron calorimetry components. Only light-collecting calorimeters are discussed in this context. Electromagnetic calorimetry (ECAL) plays a crucial role in accurately determining electron scattering kinematics, separating electrons from hadrons, measuring neutral particles, and distinguishing the two photons resulting from neutral pion decay. Hadron calorimetry (HCAL) is essential for determining the total energy in hadronic jets, especially for neutral components that cannot be tracked.

Various ECAL technologies are considered, including homogeneous detectors such as PbWO4, scintillating glass, and lead glass, as well as sampling calorimeters using scintillator fibers in tungsten powder or layered shashlyk detectors. Due to space limitations, materials with short radiation lengths are preferred. Additionally, silicon photomultipliers (SiPMs) are favored over regular photomultipliers due to their smaller size and

compatibility with magnetic fields. In the backward region, PbWO4 seems to be the only viable option. In the central region, a projective geometry is necessary, while in the forward region, high granularity is required to resolve photons from pion decay.

For HCAL, existing technologies such as scintillating/depleted uranium sampling calorimeters used in experiments like ZEUS are considered sufficiently effective. Efforts are being made to replace lead with steel and design the HCAL as a support structure for ECAL. In the hadron endcap, a denser material is preferred, and a small prototype of a compensating calorimeter with improved resolution has been constructed based on the experience gained from the STAR Forward upgrade [8].

2.2.4 Auxiliary Detector Systems

In addition to the primary central detector systems, there is a need for specialized auxiliary detector systems at the EIC, and these systems must be closely integrated into the accelerator lattice. This is particularly important for the electron and hadron polarimeters, as well as for the far-forward and far-backward regions of the detector.

In the far-forward region, silicon detectors placed in roman pots will be utilized to detect highly forward-directed hadrons with an angular range of up to 5 mrad. These detectors will employ low-gain avalanche diodes (LGADs) with high timing resolution. Similar detector technologies will be used in the off-momentum detectors to identify nuclear breakup of Lambda decay products. The detection of neutrons and low-energy photons in the forward direction will be carried out using the Zero-Degree Calorimeter (ZDC), which includes both ECAL and HCAL components. Technologies from the ALICE FoCal and the LHC ZDC are being considered for this purpose.

In the far-backward region, bremsstrahlung photons will be detected in an electromagnetic zero-degree calorimeter or a pair spectrometer to determine the luminosity, an important normalization factor for many measurements. Very low Q^2 electrons will be identified using position-sensitive detectors placed in the far-backward region or through segmentation in the zero-degree calorimeter.

Throughout other sections of the EIC, electron and hadron polarimeters will be used to nondestructively measure the polarization of the beams with a systematic precision better than 1%. To provide timely feedback to the accelerator operators, a statistical precision of similar magnitude will be achieved on short timescales. For the electron beam, a Compton polarimeter will be employed, utilizing a diode laser with a high repetition frequency and a fiber amplifier capable of reaching powers up to 20 W. Position-sensitive detectors such as diamond strip or HV-MAPS detectors can be used to measure both longitudinal and transverse polarization. For the hadron beam, the existing polarimeters at RHIC will serve as a starting point, using the atomic hydrogen jet for absolute measurements and a fast carbon ribbon for relative measurements. At the higher proton currents of the EIC, additional hydrogen jet detectors and alternative ribbon targets will be required. For 3He beams, the hydrogen jet may be replaced by a polarized 3He target.

To manage the data acquisition bandwidth and the selection of events relevant to physics analyses, the EIC will adopt a streaming readout approach that does not rely on trigger electronics to determine whether or not to record events. This approach is similar to the ongoing LHCb upgrade. On the software side, new artificial intelligence approaches are being explored. [8].

2.3 PID

In addition to tracking and calorimetry, Particle IDentification (PID) plays a vital role in the majority of particle physics experiments. Ephemeral particles are reconstructed by examining their decay location and/or decay products. Certain enduring particles (leptons and photons) can be identified by the distinct traces they leave across various layers within a typical experiment. Differentiating between long-lived charged hadrons (such as pions, kaons, and protons) presents a greater challenge, yet their identification is often crucial, particularly for accurately measuring rare processes with substantial data sets. Typically, specialized detectors are employed for this purpose, relying on the simultaneous determination of a particle's mass through measurements of both its momentum p and velocity $\beta = v/c$. Velocity can be determined using one of four techniques: measuring ionization-induced energy deposition, analyzing time-of-flight, detecting Cherenkov radiation patterns, or capturing transition radiation [36]. An illustrative comparison of the methods is shown in Figure 2.13:
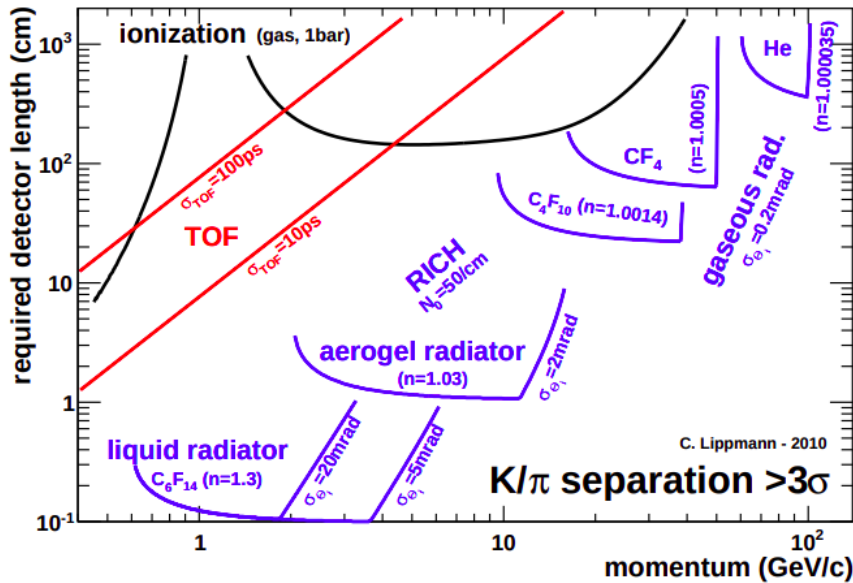
Figure 2.13: Approximate minimum detector length required to achieve a K/π separation of n$\sigma \geqslant 3\sigma$ with three different PID techniques. For the energy loss technique we assume a gaseous detector. For the TOF technique, the detector length represents the particle flight path over which the time-of-flight is measured. For the Cherenkov technique only the radiator thickness is given. The thicknesses of an expansion gap and of the readout chambers have to be added [36].

2.3.1 PID by Difference in Interaction

In a "conventional" particle physics experiment, particles are identified (including electrons, muons, their antiparticles, and photons) or, at the very least, categorized into groups (charged or neutral hadrons) based on the distinct characteristics they exhibit within the detector. The experiment consists of several key components, as depicted in Figure 2.14, each of which examines specific particle properties. These components are arranged in layers, and the particles pass through them sequentially, starting from the collision point and moving outward. The sequence includes a tracking system, followed by an electromagnetic (EM) and a hadronic calorimeter, and finally a muon system. All layers are situated within a magnetic field to bend the paths of charged particles, enabling the determination of their momentum and charge polarity.
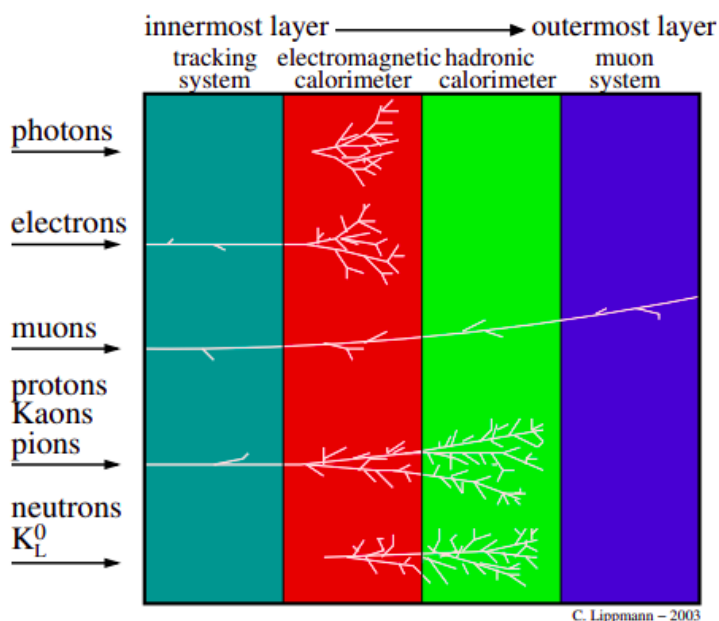

Figure 2.14: Components of a "traditional" particle physics experiment. Each particle type has its own signature in the detector. For example, if a particle is detected only in the electromagnetic calorimeter, it is fairly certain that it is a photon [36].

Tracking system

The tracking system plays a crucial role in determining the charge of particles. It works in tandem with a magnetic field to ascertain the polarity of the charge and measure the particle's momentum. Additionally, the tracking system is capable of detecting photons that undergo conversion into an electron-positron pair, allowing their identification

within the system. Moreover, charged kaon decays may be detected in a high-resolution tracking system through their characteristic "kink" topology: e.g. $K^{\pm} \to \mu\nu_{\mu}$ (64%) and $K^{\pm} \to \pi^{\pm}\pi^0$ (21%). The charged parent (kaon) decays into a neutral daughter (not detected) and a charged daughter with the same sign. Consequently, the identification of kaons primarily relies on identifying kinks within the tracking system. By analyzing the kinematics of these kink patterns, it becomes possible to distinguish kaon decays from the main source of background kinks originating from the decays of charged pions. [35] [36].

Calorimeters

Calorimeters play a crucial role in particle physics experiments by detecting neutral particles, measuring the energy of particles, and determining whether they undergo electromagnetic or hadronic interactions.

Calorimeters can be broadly categorized into two types: sampling calorimeters and homogeneous calorimeters. Sampling calorimeters consist of alternating layers of dense passive absorber material and active detector layers. In contrast, homogeneous calorimeters utilize the absorber material itself as the detection medium.

When it comes to photons, electrons, and positrons, all of their energy is deposited in the electromagnetic (EM) calorimeter. The resulting particle showers appear identical, but an electron can be distinguished by the presence of a track in the tracking system that is associated with the shower. In such cases, the energy deposition in the calorimeter must match the momentum measured in the tracking system.

In the case of hadrons, they primarily deposit their energy in the hadronic calorimeter, with a portion also deposited in the EM calorimeter. However, it is not possible to distinguish individual members within the charged and neutral hadron families solely based on the information obtained from a calorimeter [36].

Muon system

The muon and electron are nearly identical, with the main distinction being their mass, which is approximately 200 times greater for muons. Consequently, the critical energy (E_c), which refers to the energy at which the rates of energy loss through ionization and bremsstrahlung are equal in a given material, is significantly higher for muons. For example, on copper, E_c is around 400 GeV for muons compared to only about 20 MeV for electrons. Due to this disparity, muons generally do not generate electromagnetic showers and can be easily identified by their presence in the outermost detectors. In contrast, other charged particles are typically absorbed in the calorimeter system [36].

Other Particles

Neutrinos typically exhibit minimal interaction within a particle detector, such as the one depicted in Figure 2.14, and as a result, they pass through undetected. However, their presence can often be inferred by observing the momentum imbalance among the detectable particles. In the case of electron-positron colliders, it is generally feasible to reconstruct the momentum of the neutrino in all three dimensions as well as its energy. Quark flavor tagging, on the other hand, involves identifying the specific flavor of the quark that initiated a jet. The most important example is B-tagging, the identification of beauty quarks [36].

2.3.2 PID by Mass Determination

The three primary charged hadrons (pions, kaons, and protons) and their antiparticles exhibit identical interactions within an experimental configuration like the one depicted in Figure 2.14 (charge deposition in the tracking system and a hadronic shower in the calorimeter). Additionally, these particles are considered to be effectively stable. However, their identification is crucial, especially when studying hadronic decays.

To identify any stable charged particle, including charged hadrons, it is necessary to determine its charge (ze) and mass (m). The charge sign can be determined by analyzing the curvature of the particle's track. Since the mass cannot be directly measured, it must be inferred from other variables.

These are in general the momentum p and the velocity $\beta = v/c$, where one exploits the basic relationship

$$p = \gamma m v \longrightarrow m = \frac{p}{c\beta\gamma} \tag{2.1}$$

Where c is the speed of light in vacuum and $\gamma = (1\beta^2)^{1/2}$ is the relativistic Lorentz factor. The resolution in the mass determination is:

$$(\frac{dm}{m})^2 = (\frac{dp}{p})^2 + (\gamma^2\frac{d\beta}{\beta})^2 \tag{2.2}$$

Since in most cases $\gamma \gg 1$, the mass resolution primarily relies on the accuracy of the velocity determination rather than the momentum determination. The momentum is derived by analyzing the track's curvature within the magnetic field. On the other hand, the particle velocity is obtained using one of the following methods:

- measurement of the energy deposit by ionization,

- time-of-flight (TOF) measurements,

- detection of Cherenkov radiation or

- detection of transition radiation.

Each of these techniques not only offers particle identification (PID) for charged hadrons but also for charged leptons. Fortunately, the challenge of distinguishing between muons and pions, which have a similar mass $(m_\mu \approx m_\pi)$, can be overcome through alternative methods that enable straightforward identification of muons.

The application of these methods is limited to specific ranges of momentum. Within a given momentum range, the effectiveness of a technique can be evaluated using separation power, which quantifies the distinguishability of particles. This power is defined in terms of the detector response, denoted as R. If R_A and R_B represent the mean values of the detector response measured for particles of type A and B respectively,

and $< \sigma_{A,B} >$ denotes the average of the standard deviations of the measured distributions, the separation power n_σ can be calculated as follows:

$$n_\sigma = \frac{R_A - R_B}{< \sigma_{A,B} >} \tag{2.3}$$

A summary of the momentum coverage and required detector lengths using the example of K/π separation with the requirement $n_\sigma > 3$ is given in Figure 2.13.

2.3.3 Energy loss and ionization

As a high-speed charged particle traverses a substance, it engages in a sequence of inelastic Coulomb collisions with the atomic electrons of the material. Consequently, the atoms become excited or ionized, and the particle gradually loses a fraction of its kinetic energy. The average energy loss per unit path length, denoted as $\frac{dE}{dx}$, corresponds to the average number of electron/ion pairs (or electron/hole pairs in the case of semiconductors) $< N_I >$ generated along the particle's trajectory over a given distance x [27]:

$$x < \frac{dE}{dx} >=< N_I > W \tag{2.4}$$

where W represents the average amount of energy required to generate a single electron/ion pair (or electron/hole pair) in the material. Notably, W surpasses the ionization energy E_I (or the band gap energy E_g in the case of a solid) of the substance due to a portion of the energy loss being dissipated through excitation, which does not result in the production of free charge carriers. Typical values of W are approximately 30 eV for gases, remaining constant for incident particles with relativistic velocities ($\beta \approx 1$), but increasing for lower velocities. For semiconductors, the values of W are roughly proportional to the band gap energy:

$$W = 2.8E_g + 0.6eV \tag{2.5}$$

and are much lower than for gases: e.g. on average 3.6 eV in silicon and 2.85 eV in germanium [28]. Consequently, the ionization yield in semiconductor detectors is much larger than in gaseous devices. The interactions of the charged particle with the atomic electrons can be modeled in terms of two components: primary and secondary interactions. In primary interactions direct processes between the charged particle and atomic electrons lead to excitation or ionization of atoms, while secondary processes involve subsequent interactions. The primary interactions can be characterised by the Rutherford cross-section (with the energy dependence $d\sigma/dE \propto E^{-2}$) for energies above the highest atomic binding energy, where the atomic structure can be ignored. In this case the particle undergoes elastic scattering on the atomic electrons as if they were free. According to the steeply falling Rutherford spectrum most of the primary electrons emitted in such collisions have low energy. However, a significant probability for producing primary electrons with energies up to the kinematic limit for the energy transfer E_{max} exists. E_{max} is given by:

$$E_{max} = \frac{2\beta^2\gamma^2 m_e c^2}{1 + x^2 + 2\gamma x} \tag{2.6}$$

where m_e is the electron mass, $x = m_e/m$ and m is the mass of the incident particle. In such collisions where the impact parameter is extremely small, the energy transferred

to the electron surpasses E_I (or E_g) and generates additional ionization through the production of δ-rays or *knock-on* electrons in subsequent interactions. These δ-rays may even exit the sensitive volume of the detector, but the presence of a magnetic field can cause them to curve and remain in proximity to the track of the primary charged particle. In this scenario, they contribute to the measurement of the deposited energy.

On the other hand, in collisions with a large impact parameter, the atomic electrons receive significantly less energy, which is primarily utilized for excitation without the creation of free charges. However, in gases, there may be instances of tertiary ionization through collisions between an atom in an excited state and other atoms, known as Penning ionization [37].

2.3.4 Time-of-Flight

Time-of-flight (TOF) measurements yield the velocity of a charged particle by measuring the particle flight time t over a given distance along the track trajectory L. The particle velocity $\beta = v/c = L/tc$ depends on its mass m and momentum p through:

$$\beta = \frac{1}{\sqrt{(\frac{mc}{p})^2 + 1}} \tag{2.7}$$

Thus, one can calculate the mass m from measurements of L, t and p:

$$m = \frac{p}{c}\sqrt{\frac{c^2 t^2}{L^2} - 1} \tag{2.8}$$

If two particles with masses m_A and m_B, respecively, carry the same momentum, their flight time difference can be calculated as:

$$|t_A - t_B| = \frac{L}{c}|\sqrt{1 + (\frac{m_A c}{p})^2} - \frac{L}{c}|\sqrt{1 + (\frac{m_B c}{p})^2}| \tag{2.9}$$

With $p \gg mc$ the approximation $\sqrt{1 + (mc/p)^2} \approx 1 + (mc)^2/2p^2$ can be used, and with Eq. 2.3 the separation power becomes:

$$n_{\sigma TOF} = \frac{|t_A - t_B|}{\sigma_{TOF}} = \frac{Lc}{2p^2 \sigma_{TOF}}|m_A - m_B|^2 \tag{2.10}$$

Here σ_{TOF} is the resolution of the TOF measurement. Misidentification of particles occurs at higher momenta, where the time difference $|t_A t_B|$ becomes comparable to σ_{TOF}. Assuming a time resolution of 100 ps (60 ps) and requiring a separation of $n\sigma_{TOF} = 3$, the upper limits for the momentum are 2.1 GeV/c (2.7 GeV/c) for K/π separation and 3.5 GeV/c (4.5 GeV/c) for K/p separation (see Figure 2.15). A lower momentum threshold is defined by the curvature of the tracks in the magnetic field. Assuming a path length L = 3.5 m and a magnetic field of 0.5 T, only particles with a momentum larger than about 300 MeV/c reach the TOF wall.
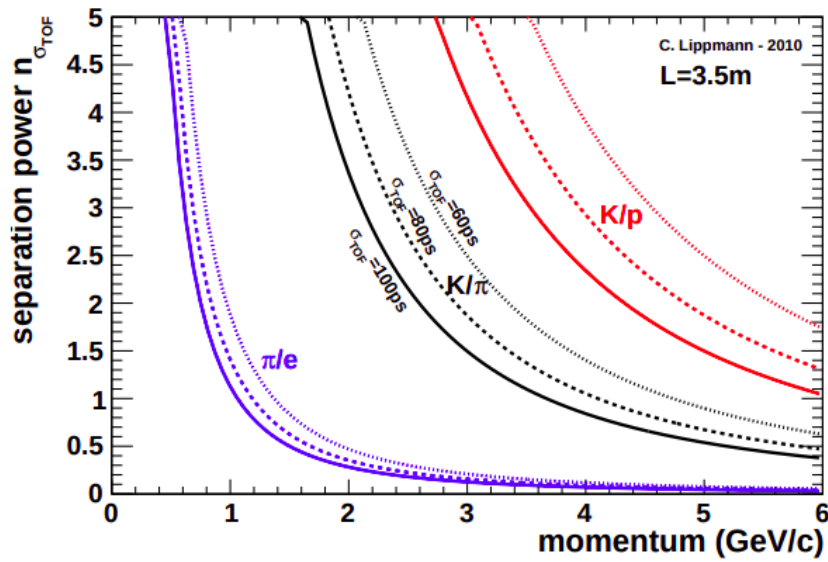
Figure 2.15: Particle separation with TOF measurements for three different system time resolutions ($\sigma_{TOF} = 60$, 80 and 100 ps) and for a track length L = 3.5 m. Infinitely good precisions on momentum and track length measurements are assumed.

2.3.5   Cherenkov Imaging

Cherenkov radiation is a shock wave resulting from a charged particle moving through a material faster than the velocity of light in the material. The Cherenkov radiation propagates with a characteristic angle with respect to the particle track Θ_C, that depends on the particle velocity:

$$cos(\Theta_C) = \frac{1}{\beta n} \tag{2.11}$$

where n is the refractive index of the material. In general, the refractive index varies with the photon energy: $n = n(E)$(chromatic dispersion). Since $|cos(\Theta_C)| \leq 1$, Cherenkov radiation is only emitted above a threshold velocity $\beta_t = 1/n$ and $\gamma_t = 1/(1\beta_t^2)^{1/2}$. In general, Cherenkov detectors contain two main elements: a radiator through which charged particles pass (a transparent dielectric medium) and a photon detector. The number of photoelectrons ($N_{p.e.}$) detected in a given device can be approximated as [29]:

$$N_{p.e.} \approx N_0 z^2 L sin^2(\Theta_C) \tag{2.12}$$

where L is the path length of the particles through the radiator, ze is the particle charge and N_0 is a quantity called the quality factor or figure of merit. As Cherenkov radiation is a weak source of photons, the light transmission, collection and detection must be as efficient as possible. These parameters are contained in N_0, as well as the photon collection and detection efficiencies of the photon detector. Typical values of N_0 are between 30 and 180 cm^1. Three different types of Cherenkov counters can be distinguished:

- *Threshold counters* measure the intensity of the Cherenkov radiation and are used to detect particles with velocities exceeding the threshold β_t. A rough estimate of the particle's velocity above the threshold is given by the pulse height measured in the photon detector.

- *Differential counters* focus only Cherenkov photons with a certain emission angle onto the detector and in this way detect particles in a narrow interval of velocities.

- *Imaging Cherenkov detectors* make maximum use of the available information (Cherenkov angle and number of photons) and can be divided in two main categories: RICH (Ring Imaging CHerenkov) and DIRC (Detection of Internally Reflected Cherenkov light) devices.

Threshold Cherenkov detectors

The use of the Cherenkov effect can be seen from another angle when focusing on the threshold of light emission.

Since the value of the cosine of θ_C cannot be greater than 1, and is equal to $1/\beta n$, we can obtain β_{thr} as $1/n$, so at a value of $\beta_{thr} = 1/n$ above which Cherenkov light is emitted. This feature can be exploited in a very simple particle identification detector called threshold Cherenkov detector whose working principle is described in Figure 2.16.

In the case of a beam of pions, kaons and protons with same momentum with two threshold Cherenkov detectors C_1 and C_2 with different refracting index, the particles will emit Cherenkov light only if over threshold. So, if the indices ($n_2 > n_1$) are chosen properly, the kaons will emit light only in radiator C_2, pions in both, and protons neither, since:

$$n_1 < n_2$$
$$\beta_{thr1} > \beta_{thr2}$$
$$\beta_{pion} > \beta_{kaon} > \beta_{proton}$$
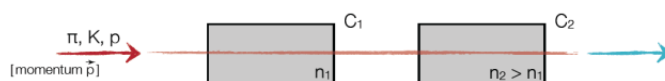
Figure 2.16: Working principle of a Threshold Cherenkov Counter.

This way we can distinguish the three particles by looking if Cherenkov light is emitted in the radiators.

This is the simplest kind of Cherenkov detector: while in others the Cherenkov light emisson angle θ_C is measured, in this case the particles are identifying via the presence or absence of light emitted in the various radiators.

Differential Cherenkov detectors

Differential Cherenkov detectors give a signal only for particles inside a certain β range. Selecting a range of beta means selecting a range of θ_C. They work only with a well-collimated beam and not for particles that are produced in an interaction such as the ones in colliders. In order to work ideally, the beam should be as collimated as possible, and working in the presence of a gas radiator, its refractive index will be such that the particle will be able to emit Cherenkov light. A spherical mirror positioned at the end of the detector will reflect the light produced along the radiator onto a focal plane of the mirror (as in Figure 2.17).

With a Gas radiator
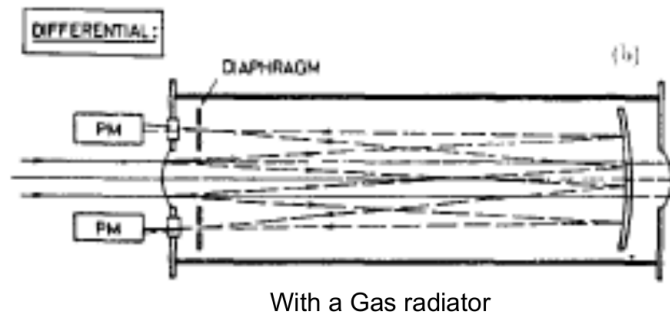
Figure 2.17: Details of a Differential Cherenkov detector. The working principle depends on the presence of a mirror.

All the rays reaching the spherical mirror with the same angle will be reflected and focalized onto the focal plane and a circumference image will be produced, in principle with a small annular width. On the contrary, by putting a plane nearer to the mirror, the detected signal will resemble a circular crown. By inserting a diaphram between the reflected light and the focal plane, such that only the light emitted with a certain θ_C will be reflected on that plane and by inserting a series of PMTs for signal detection, what is detected is the signal only of light emitted with the desired angle.
This way, thanks to a diaphragm, it is possible to select a range of θ_C.

Another possible arrangement is the one in Figure 2.18: depending on the angle and on the refractive index, light is detected if emitted in a certain range of θ_C. We have a θ_{min} (which corresponds to θ_{thr}) and a θ_{max} (which is the angle above which we will have total reflection), corresponding respectively to a β_{min} and a β_{max}: that way we select a range of $\beta_{min} < \beta < \beta_{max}$. Using diamond crystals we can select a $\Delta\beta = 0.04$ so this radiator allows to reach a narrow range, so a very good resolution $\Delta\beta$ / $\beta = 10^{-7}$. Cherenkov light is emitted in a small range of wavelength in the UV range and this dispersion of different wavelengths will produce a spectrum. Traveling inside the radiator, Cherenkov light will reach a wider spectrum and when it reaches the diaphragm

it will not be concentrated in a confined point. This will result in a larger error in the selection of the angle and therefore in the selection of the β, due to the larger $\Delta\theta$, so a larger $\Delta\beta$. In order to diminish this effect, some optics can be used to counter the dispersion effect.

This kind of detector is called DISC: with this adjustment a smaller $\Delta\theta$ and so a smaller β resolution are obtained. Knowing the momentum and fixing it, selecting β means selecting the particle, so reducing the resolution of β means reducing the resolution of the inferred particle mass.
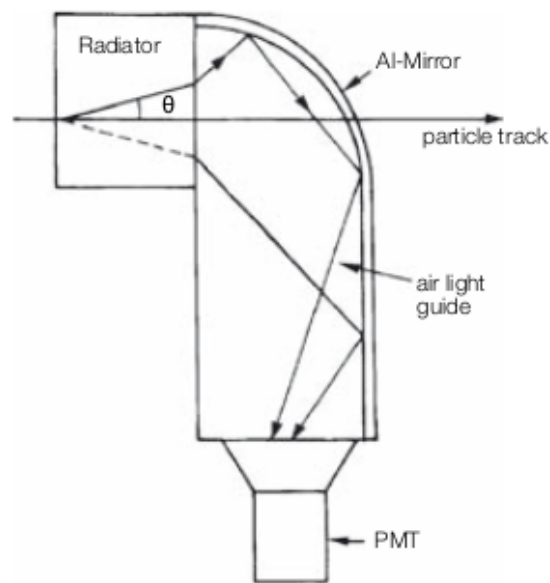
Figure 2.18: Details of a DISC Differential Cherenkov detector.

RICH detectors

For particles produced in a collision, it's not possible to use the previously described Cherenkov detectors.

An option is to use the (Ring Imaging Cherenkov) RICH which allows for the measurement of the β of a particle. Ring Imaging are used to exploit Cherenkov light emission by particles produced from an interaction and not in a collimated beam. The principle is such that the RICH produces an image due to the reflected light which corresponds to a circumference, and from this image, it's possible to measure β. The particle will emit light all along the track when inside the radiator only if over threshold. The light will be reflected by the mirror in a single point since the detector is located at the mirror's focal plane.

Due to this fact, what is produced in this case is a ring with in principle no thickness. The reconstruction of this circumference with a given radius is possible through the photons detected and a relationship between the radius of the circle and the dimension (radius) of the mirror and of the detector can be established, giving the opportunity to reconstruct the θ_C, since the radius of the Cherenkov ring is:

$$r = f\theta_C = (R_M/2)\theta_C = R_d\theta_C \tag{2.13}$$

where f is the focal length.
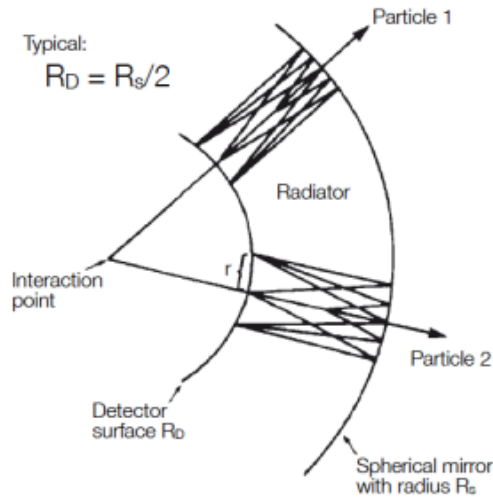
Figure 2.19: Working principle of a RICH Cherenkov detector.

θ represents the angle between the interaction point and the Cherenkov circle in Figure 2.19 and it corresponds to θ_C, because of the geometry and the relation $tan\theta_C \simeq \theta_C$ is also valid. From θ_C the value of β can be extracted.

Another technique is the proximity focusing Cherenkov detector that again produces a ring with a very negligible thickness, but that is possible under some requirements (Figure 2.20). It does not include a spherical mirror but a very thin plane radiator. Light light is produced when a charged particle crosses the radiator if it is above threshold; starting from when the particle enters it until it exits it. For this reason a thin radiator is preferable, in order to have a ring with a negligible thickness.

The example in Figure 2.20 describes a case with two particles with different β. that is with different θ_C: in principle I'll have

With enough photons, two distinct circumferences can be reconstructed and the two different θ_C angle can be calculated, knowing the distance between the radiator and the photon detector.

This technique is often used to detect more than one kind of particle, when the particle rate is relatively high.

It's an simple technique to accomplish because both a very thin radiator and enough photon statistics in order to reconstruct the ring are needed.

In addition, the rate must be sufficiently but not excessively high, as the emitted photons would create too many rings, making it impossible to reconstruct each circumference.
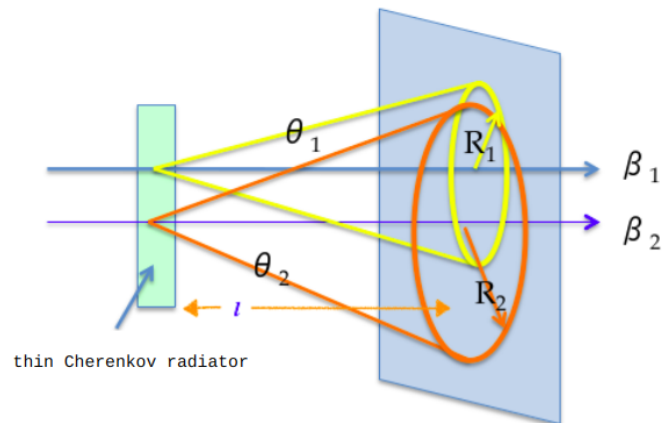
Figure 2.20: Proximity focusing Cherenkov detecor working principle.

2.3.6 Transition Radiation

Transition Radiation happens when a particle goes from crossing a medium with dielectric constant ϵ_1 to another with dielectric constant ϵ_2, in analogy to refraction, where a photon traverses the separation surface between two materials and its direction changes. In the same way, when a charged particle passes from one medium to another, there is photon emission: the relevant feature of these photons is that they are emitted at a given angle, which is proportional to $1/\gamma$. The energy of the radiated photons is proportional to γ and the number of emitted photons is proportional to Z^2. The threshold, equal to $\gamma > 1000$, is present because for lower gammas, the energy of the photons is such that the photons cannot be detected.

The transition radiation process is important in cases in which it is necessary to discriminate between charged particles, for example electrons and pions, as the presence of one of the two in high energy collisions, can indicate a different decay channel of a particle or a different particle decaying. A way to distinguish the signal from an e^- and a π is to detect the presence of transition radiation emission.

Since the γs are emitted every time a particle passes through a different medium, a TR detector can be built with several separation surfaces, in order to reach a sufficient number of photons. This is typically done by means of alternating thin layers of lithium foil and layers of air. Having a different dielectric constant and low atomic number Z, it is possible to keep the re-absorption as small as possible.

Taking as an example the electron, it can either go through the radiator without emitting Transition Radiation and only release energy via ionization, as described by the green curve, or emit photons in addition to dE/dx, as described by the red curve in Figure 2.21.

The blue line corresponds to a pion with no TR emission.

The plot describes the signal due to ionization starting from a time of 0.3 μs and decreasing until it reaches a constant value and disappearing after a few microseconds. We can see that pion and electron have the same behavior in the case of no TR emission, due to the fact that they both have unitary charge. In the case of transition radiation emission, instead, the behaviour of the electron presents a second peak at about 2.5 μs. The electron, just like all other charged particles, can emit detectable transition radiation only if its momentum is above the value given by the γ threshold.

Since the value of this threshold differs form one particle to another, for a fixed momentum, it is possible to distinguish two two kinds of particles based on their TR emission, or lack thereof.
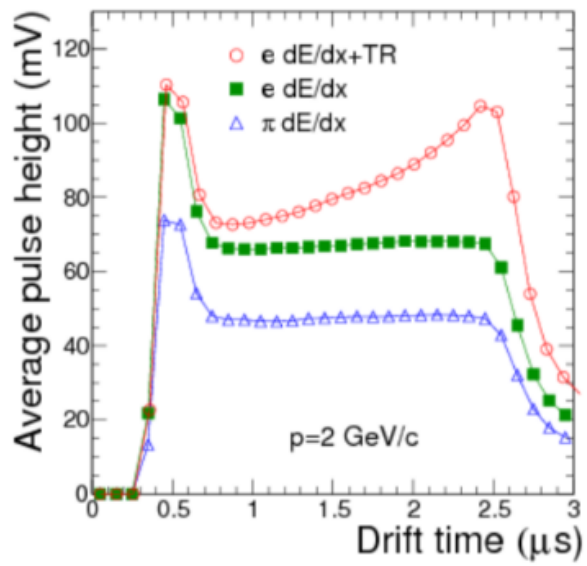
Figure 2.21: Signal from transition radiation emitting particle and non-emitting.

2.4 dRICH Dual Radiator in EIC Hadron-endcap

The dual-radiator Ring Imaging Cherenkov (dRICH) detector is classified as a day-1 detector due to its compliance with the Particle Identification (PID) requirements of the EIC physics program.

The dRICH detector is designed to enable continuous and comprehensive identification of hadrons, ensuring a separation of π/K/p particles by at least 3σ from around 3 GeV/c to approximately 60 GeV/c in the ion-side end cap of the EIC detector. Additionally, it offers precise identification of electrons and positrons, with e/π separation, covering a range from a few hundred MeV up to roughly 15 GeV/c. The baseline geometry encompasses polar angles from around 5 to approximately 25 degrees. Achieving such momentum coverage in the forward ion-side region is a crucial requirement for the EIC physics program. Presently, the dRICH is exclusively designed to serve as the hadron identification detector in the EIC, providing continuous coverage in RICH mode across the entire momentum range necessary for the forward end-cap.

The dRICH baseline configuration comprises six identical open sectors, with each sector featuring two radiators: aerogel with a refractive index of ≈ 1.02 and gas with a refractive index of ≈ 1.008. These radiators share the same outward focusing mirror, while the instrumented area is equipped with highly segmented photosensors consisting of $3\times3\ mm^2$ pixels. The arrangement of the photosensor tiles on a curved surface minimizes divergences.

The initial prototype configuration described a detector with a longitudinal length of approximately 160 cm. However, even at a reduced length of around 100 cm, the preliminary version of dRICH achieves performance that meets the key physics requirements, highlighting the remarkable flexibility of potential dRICH configurations.

To meet the EIC requirements, crucial elements include an effective exchange between the two radiators and the selection of a suitable photosensor that preserves the capability to measure single photons within a strong magnetic field. The dRICH focusing system is designed to position the detector outside the EIC spectrometer acceptance, reducing the demands in terms of material budget and radiation levels. This characteristic makes the dRICH an ideal candidate for utilizing magnetic field tolerant SiPMs with integrated cooling systems to mitigate significant dark count effects.

A small-scale prototype is being developed to investigate critical aspects of the proposed dRICH detector, in particular related to the interplay and long-term performance of the two radiators and simultaneous imaging. The prototype vessel is composed of standard vacuum parts to contain the cost and support pressures different from the atmospheric one. This would allow efficient gas exchange and, in principle, adjustment of the refractive index and consequent flexibility in the gas choice. The prototype supports the usage of various type of photosensors, in particular SiPM matrices and MCP-PMTs (Micro Channel plate PMT - in which a dynode structure is replaced by MCP). A program has been initiated to study the potential of SiPM sensors for Cherenkov applications - which

is the object of this dissertation - aiming to a study of the use of irradiated SiPM in conjunction with the dRICH prototype. Promising SiPM candidates will be irradiated at various integrated doses (up to the reference value of 10^{11} n_{eq} cm^{-2}) and will undergo controlled annealing cycles at high temperature (up to 180° C). The SiPM response before and after irradiation will be characterised and their imaging potential will be studied with a customised electronics. High frequency sampling and Time-of-Threshold-based readouts will be compared. An interesting option is the ALCOR front-end chip, which is designed to work down to cryogenics temperatures, features low-power TDCs that provide single-photon tagging with binning down to 50 ps. The irradiated sensors will be cooled down to the working temperature (down to -40° C) to instrument an area suitable for imaging tests with the dRICH prototype.

An initial survey of the most promising candidates available on the market requires pursuing in order to meet the EIC specifications.

A dedicated R&D campaign will be necessary following the initial survey of the most promising candidates.

Chapter 3

Sensors for dRICH

A key element of a general-purpose experiment at EIC is a detector providing particle identification in the hadronic end-cap. To meet these requirements a dual-radiator dRICH is being developed: it exploits Cherenkov light produced by two different mediums to cover the full momentum range without penalty owing to the Cherenkov threshold of the gas.

3.1 dRICH & Performance Requirements

The purpose of the EIC-PID is developing an integrated PID system that satisfies the requirements imposed by the EIC science program, and that is compatible with the detector concepts developed at the two candidate sites for the EIC, namely Brookhaven National Laboratory (BNL) and the Thomas Jefferson National Accelerator Facility (JLab). The current baseline design of the EIC-PID system, shown in Figure 3.1, includes a dual-radiator RICH (dRICH) and a modular-aerogel RICH (mRICH) that uses a Fresnel lens placed in the electron endcap. In addition, the measurement of Internally Reflected Cherenkov light (DIRC) detector is located in the barrel region, where a fast time-of-flight (TOF) system is foreseen to provide PID for low-momenta particles.

A scheme of the dRICH prototype is represented in Figure 3.1. A charged particle crossing the dRICH initially passes through the aerogel (n $\simeq$ 1.02) and produces a Cherenkov-photons cone of about 11 degrees aperture. The photons are reflected back by a first spherical mirror and focused on the photon detector array. The particle also passes through the gas (n $\simeq$ 1.00085), which fills the detector producING a Cherenkov-photon cone of about 2 degrees aperture. The first mirror has a central hole, to allow the photons produced in the gas at small angles to fly towards a second spherical mirror and be focused back on the same photon detector array. The information of the two imaged Cherenkov rings combined with the beam momentum will allow identification of pions, kaons, and protons. The prototype consists of two main parts: the gas chamber and the
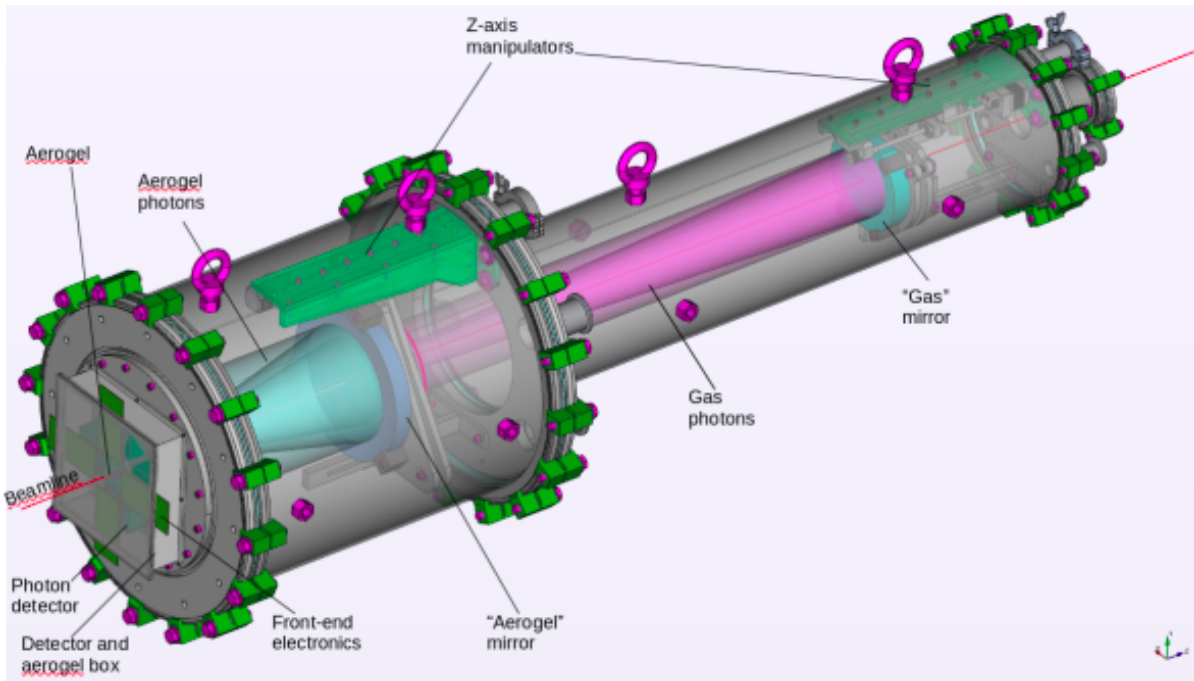
Figure 3.1: dRICH detector prototype.

detector box.

The gas chamber:

- mechanically sustains the dRICH, especially the spherical mirrors;

- includes the mechanics to regulate the mirrors angle and position along the detector axis;

- bears both under and over pressurization, to evacuate the air and introduce the gas;

- preserves light tightness.

The detector box:

- houses the aerogel box in a N_2 dry atmosphere;

- mounts the photon detector and the front-end electronics;

- supports a cooling system for the silicon photomultipliers (SiPM) matrices.

The design optimized for EIC is shown in Figure 3.2 and uses both an aerogel radiator and a gas radiator (C_2F_6) to cover the full momentum range in a single device[1].
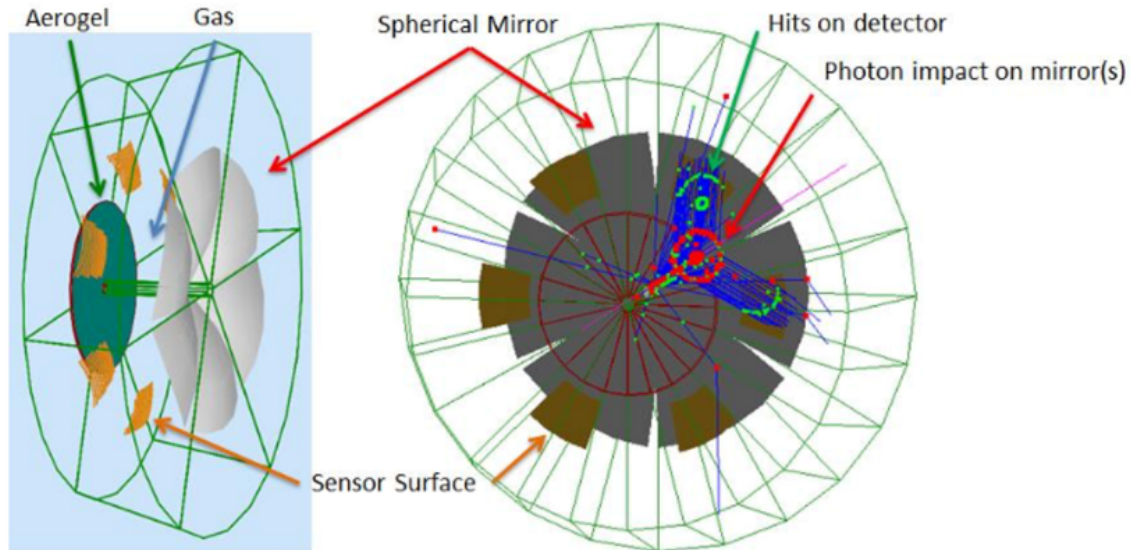
Figure 3.2: Dual RICH detector configuration after AI-driven optimization. Multiple mirror panels (gray) focus rings from both aerogel and C_2F_6 perfluorocarbon radiators onto the same focal plane [8].

Figure 3.3 shows the converged solution for the detector performance optimization in both the aerogel and the gas sections. Each term in the final resolution is isolated by its contribution of the Cherenkov angle resolution. The aerogel performance is dominated by the natural chromaticity of the radiator medium itself. All other contributing factors to the aerogel performance are negligible as compared to chromaticity which represents a fully optimal performance. The angular resolution of the gas section is more complex: emission terms are dominant and peak at the edges of the segmented RICH mirrors. The optimization of this factor is evident by the fact that the Emission resolution term is of equal height at the two extremes of the polar angle acceptance.

Figure 3.4 indicates the calculated performance of the dRICH detector for e-π, π-K, and K-p separation. Several features are worth noting:

1. The dRICH is not merely limited to hadron-PID application, but also provides excellent eID (electron identification) out to roughly 20 GeV/c momentum

2. The dRICH does not have gaps in the performance either at low momentum (due to aerogel) nor at intermediate momentum due to the index match of the aerogel and gas radiator performance

3. The π-K performance achieves the full goals of the requirements matrix

66
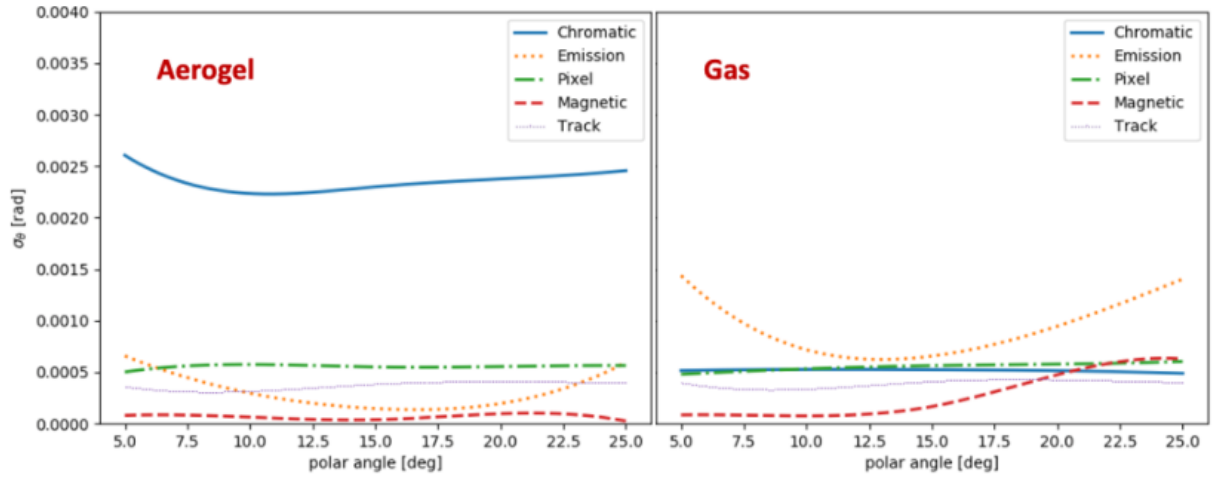
Figure 3.3: Resolution contributions for the Dual RICH. As is true for most aerogel implementations (left panel), the chromatic dispersion of the radiator itself is the limiting factor in the resolution. Conversely, for the gas detector, the emission term dominates due to off-axis focusing[8].
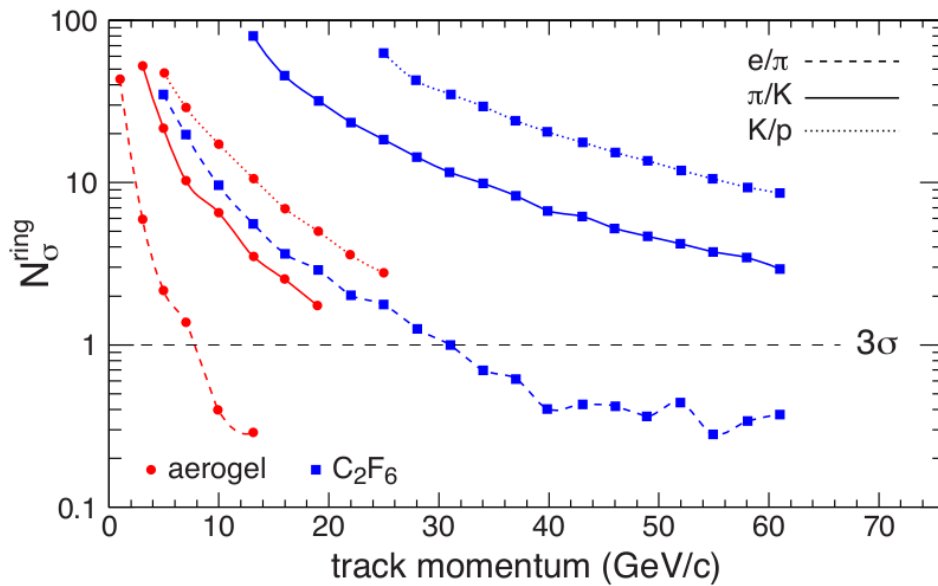
Figure 3.4: Performance of the Dual RICH for a variety of particle species. In each case, the combination of aerogel and gas provides uninterrupted PID across the full range. The device also serves for eID across more than the required momentum range[8].

67

As is the case for most modern gas Cherenkov detectors, the dRICH design utilizes the superior performance of perfluorocarbon radiator gas (C_2F_6). Future environmental concerns may concern the followign issues:

- It may be required to recover and purify the radiator gas to avoid release to the environment, which is a significant cost and complexity

- Environmental concerns in the worst case could drive the cost and availability of the gas beyond tolerable levels

Current calculations demonstrate that these issues could be avoided by running an environmentally friendly gas at high pressure. While current calculations indicate that the dRICH performance would be insignificantly affected by a switch to Argon gas at 3 atm, this will nonetheless impose an engineering challenge to maintain a low material budget[8].

3.2 Solid state silicon detectors for timing applications

Solid-state detectors, mainly based on silicon and germanium technologies, are widely used in modern High Energy Physics (HEP) as excellent light and charged particles detectors. The inherent characteristics of the materials used, ensure applications such as precise measurements of time, position, and energy.

A solid-state detector is essentially an ionization chamber, where the signal is produced by the movement of charge carriers. To make this possible, solid semiconductor materials are used, within group IV of the periodic table. Each atom in the crystal shares four valence electrons with four neighbor atoms. These materials behave like insulators at very low temperatures (near 0K); at these temperatures, the electronic valence band structure is full. there are no electrons available for electrical conduction in the conduction energy band. At higher temperatures, due to thermal vibration, some of the bonds between the atoms of the lattice break, creating an electron-hole pair which is therefore available for the electrical conduction of the material. At the temperature of 300K the density of electrons-holes for Silicon is about $10^{10} cm^{-3}$ which corresponds to an intrinsic resistivity of about 350 $K\Omega$ cm. The energy gap between the valence band and the conduction band, under these conditions, is 1.115 eV . Being very abundant in nature, and having been the subject of studies for years, Silicon, which can be operated at room temperatures, is mostly used in the electronics industry and in HEP.

3.2.1 P-N junction and charge diffusion

A doped structure is used instead of a pure silicon crystal in the majority of applications, where certain atoms are swapped out for elements from the III (acceptors) or V group (donors). As a result, the crystal receives an overabundance of holes or electrons, leading to the formation of P-type silicon or N-type silicon, respectively.

The so-called P-N Junction is produced when P-type and N-type silicon come into contact. The charge carriers will naturally disperse from one area to another due to their non-homogeneous distribution. The equations below explain the flux of holes ($\vec{F_p}$) and electrons ($\vec{F_n}$):

$$\vec{F_p} = D_p \vec{\nabla} p$$
$$\vec{F_n} = D_n \vec{\nabla} n$$

(3.1)

Where $\vec{\nabla}_p$ and $\vec{\nabla}_n$ represent the graient of electrons and holes denities, and D_p, D_n the diffusion constants [cm^2/s], related by the Einstein relation to the temperature T:

$$D_i = (\frac{kT}{q})\mu_i \qquad\qquad (3.2)$$

The Boltzmann constant is denoted by k and has a value of $8,617 \cdot 10^{-5}$ eV K^{-1}, while the elementary charge is denoted by q and has a value of $1,602 \cdot 10^{-19}$ C.

The mobility of charge carriers, denoted by μ_i and measured in units of $[cm^2/Vs]$, is influenced by doping and temperature.

For intrinsic silicon at a temperature of 300K, the mobilities of electrons and holes are approximately $\mu_n \backsim 1350\ cm^2/Vs$ and $\mu_p \backsim 450\ cm^2/Vs$, respectively. Diffusion continues until the system reaches equilibrium. The remaining ions create a space charge and an electric field that stops diffusion, resulting in an intermediate region in the P-N junction that is devoid of charge carriers. This region is known as the depletion region or zone, as depicted in Figure 3.5.
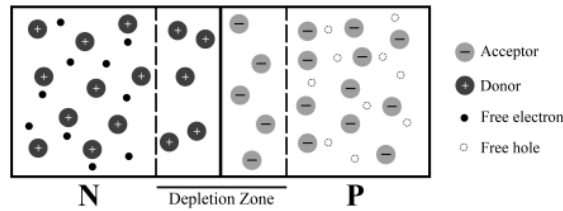
Figure 3.5: P-N junction and Depletion Region.

3.2.2 Electric field and charge drift

The following relationships can be used to explain the drift of charge carriers in an electric field E:

$$\vec{v}_p = (\frac{q\tau_c}{m_p})\vec{E} = \mu_p\vec{E}$$
$$\vec{v}_n = (\frac{q\tau_c}{m_n})\vec{E} = \mu_n\vec{E} \qquad\qquad (3.3)$$

One can observe that the drift velocities of electrons and holes, represented by $\vec{v}_n$ and $\vec{v}_p$, respectively, are directly proportional to their respective mobilities μ_n and μ_p. These formulas are derived under the assumption that charge carriers with charge $\pm q$ and mass m_i move through the lattice in response to an electric field, while losing energy through scattering due to imperfections. The mean time between successive collisions is represented by τ_c. For larger electric fields, τ_c decreases until the drift velocity reaches a saturation point. The PN junction described in the previous paragraph can either

increase or decrease the size of the depletion region when subjected to an external voltage. A forward bias voltage, denoted by V, can reduce the size of the depletion zone, promoting the natural diffusion of charge carriers. In contrast, a reverse bias voltage increases the size of the depletion region, as illustrated in Figure 3.6.
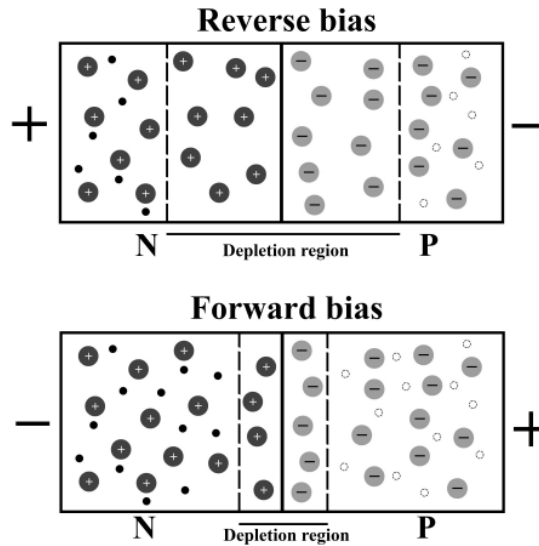

Figure 3.6: P-N junction with two different polarizations.

The overall current density of the charge carriers can be calculated by adding the contributions of electron and hole diffusion and drift:

$$\vec{J}_p = q\mu_p p\vec{E} - qD_p\vec{\nabla}p$$
$$\vec{J}_n = q\mu_n n\vec{E} + qD_n\vec{\nabla}n$$

(3.4)

It is important to highlight that this relationship holds true when the electric field, denoted by $\vec{E}$, is not excessively strong and when there are no external magnetic fields that can alter the path of the charge carriers. When subjected to extremely high electric fields, the energy acquired by individual charge carriers can be significant enough to generate a new electron-hole pair. This can initiate an avalanche process and lead to an electrical breakdown of the devices. Avalanche processes of this nature are utilized in SiPMs that operate above the breakdown voltage or within a controlled range in LGAD technologies.

3.3 Passage of particles through silicon detectors
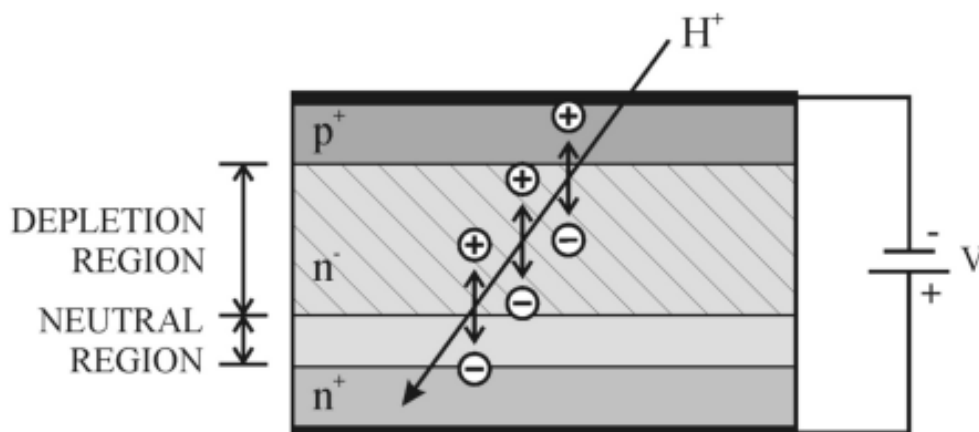
Figure 3.7: The operating principle of a silicon detector (p-on-n type).

Figure 3.7 illustrates the working principle of a silicon detector of the p-on-n type. A silicon detector typically comprises of a P-N junction consisting of heavily doped p^+ and n^+ electrodes separated by a lightly doped n^- type bulk. When in reverse biasing conditions, the heavily doped n^+ silicon is directly connected to the positive electrode where the negative charges are gathered. Conversely, the p^+ silicon is linked with the negative electrode where the holes are collected. The application of a reverse bias of sufficient magnitude leads to the creation of a depletion region that is almost coincident with the detector's active region. Here, charged particles or photons can interact with the detector structure, generating electron-hole pairs. As these are the only mobile charges in this region, they produce a signal, or rather, induce a current that can be measured. The signal persists until all charge carriers have reached their corresponding collection electrodes.

3.4 Time Resolution

A typical time measurement system is depicted in Figure 3.8.
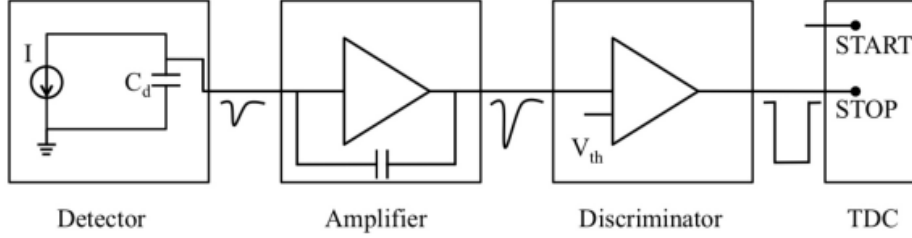
Figure 3.8: Time-measurement system chain.

The working principle of a silicon detector can be depicted as a device that generates current, with a capacitance connected in parallel. The generated current signal is amplified and then typically discriminated by a threshold system. To measure the time interval between the trigger (which starts the TDC and can come from another detector or an external source related to the primary event) and threshold crossing, a Time to Digital Converter (TDC) is used. The time resolution of a silicon detector can be measured and involves at least 5 contributions that add up quadratically [38]:

$$\sigma_t^2 = \sigma_{TS}^2 + \sigma_{Landau}^2 + \sigma_{Dist}^2 + \sigma_{Jitter}^2 + \sigma_{TDC}^2 \tag{3.5}$$

- The Time Slewing term σ_{TS}^2 and the Landau term σ_{Landau}^2 are due to the nature of the energy deposition process of the charged projectile.

  Each signal is distinct and the amount of energy released varies. Depending on the magnitude of the signal, it may cross the preselected threshold at different times. This phenomenon is known as time slewing, which can be simply rectified by examining the peak amplitude of the signal or the quantity of charge deposited. If it is supposed that the signal is linear with the rise time t_r and amplitude S, then the time delay t_d caused by time slewing is expressed as:

$$t_d \propto \frac{t_r V_0}{S} \tag{3.6}$$

  with threshold voltage V_0. The RMS of the t_d therefore provides the related error σ_t^2:

$$\sigma_{TW} = [t_d]_{RMS} \tag{3.7}$$

The Landau term, on the other hand, is connected to the variation of a minimum ionizing particle's (MIP) interaction with silicon; in fact, the energy deposited by an incoming particle with a specific energy is spread in accordance with the Landau distribution.

- The distortion term σ_{Dist}^2 is strongly correlated with the uniformity of the Electric field which causes changes in the shape of the signal from event to event.

- The jitter term σ_{Jitter}^2 is caused by noise from both the electronic and detector systems. When the signal is in the rising phase, the threshold comparator may be triggered either too early or too late due to the effect of noise at that point. Therefore, σ_{Jitter} is directly proportional to the root mean square (RMS) of the noise, σ_N, and inversely proportional to the slope of the signal near the threshold value:

$$\sigma_{Jitter}^2 = \frac{\sigma_N}{dV/dt} \tag{3.8}$$

- The term related to the TDC, σ_{TDC} is a constant that can be expressed as:

$$\sigma_{TDC} = \frac{TDC_{bin}}{\sqrt{12}} \tag{3.9}$$

where TDC_{bin} is the width in time of the least significant bit of the used TDC.

The initial three terms of equation 3.5 represent the characteristics of the detector construction and interaction with particles. Thus, these contributions can be combined into a single term, known as the intrinsic resolution term σ_{intr}. With this notation, equation 3.5 can be expressed as follows:

$$\sigma_t^2 = \sigma_{intr}^2 + \sigma_{Jitter}^2 + \sigma_{TDC}^2 \tag{3.10}$$

3.5 SiPM

A matrix of Single Photon Avalanche Photodiode (SPAD) on a common silicon substrate forms a silicon photomultiplier (SiPM), a solid-state photodetector. Each cell (pixel) functions individually as a micro Geiger counter (binary system), i.e., it only indicates the passage of a photon without providing additional details about the signal, such as the number of photons [30].

This is possible, however, through to the parallel operation of several SPADs, exploiting their small size.

This kind of detector, created as a technological advancement over the conventional photomultiplier, has recently attained very high performance in terms of single-photon sensitivity and good intrinsic time resolutions. These days, this kind of detector is widely used in the fields of technology, medicine, and HEP.

3.5.1 SiPM structure and working principles

As shown in Figure 3.9, an analog SiPM is a matrix made up of 100-10000 SPADs with typical dimensions between 10 μm^2 and 100 μm^2. When a single SPAD causes an avalanche, the quenching resistors R_q attached to each one are utilized to stop the process of uncontrolled multiplication. They are read in parallel.
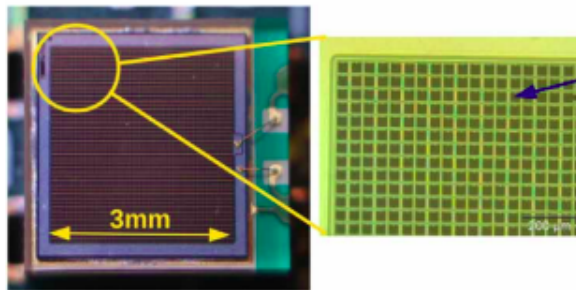
Figure 3.9: Srtucture of an analog SiPM.

For each triggered SPAD, $10^4 - 10^6$ elementary charges are generated when one or more SPADs enter Geiger-mode. Due to their parallel connection, the signal generated will depend on how many SPADs are activated. Since the signal produced will be the same in both scenarios — for example, when a single SPAD is struck by multiple photons — this instance cannot be distinguished from the other. Figure 3.10 shows the SiPM single pixel (SPAD) comparable circuit.

The SPAD can be thought of as a link that runs parallel to the diode's total internal capacitance C_d (which is the sum of the SPAD's area capacitance and any perimeter or
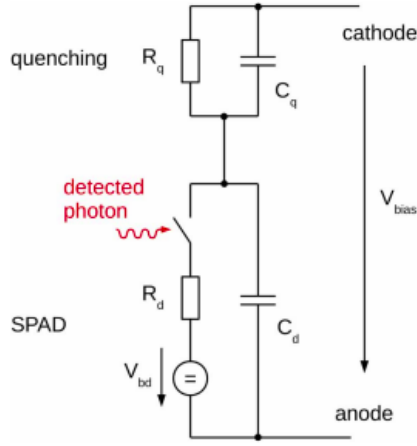
Figure 3.10: SPAD equivalent circuit.

parasitic capacitances). The quenching series circuit is formed by a parasitic capacitance (C_q) in parallel with the quenching resistor (R_q). The applied voltage V_bias is the voltage on C_d in the quiescent state. In this approach, a signal caused by a photon (or a noise event) might be thought of as the switch closing in figure. As a result, the capacitor C_d begins to discharge and there is an exponential voltage drop in the node between C_q and C_d. The capacitor C_q starts charging through R_d at the same moment. When charging, capacitances $C_q + C_d$ are involved, and the voltage discharge time constant τ_d is:

$$\tau_d = R_d(C_q + C_d) \tag{3.11}$$

It should be noted that the influence of R_q has been overlooked because it is typically quite large. The voltage of the breakdown over which the avalanche process in the SPAD begins is represented by the model's V_{bd}, which is the maximum voltage drop at the internal node. Starting with this, the overvoltage V_{ov} can be defined as follows:

$$V_{ov} = V_{bias} - V_{bd} \tag{3.12}$$

The discharge of C_d and recharge of C_q end when the current through R_d reaches the value I_d which is approximately:

$$I_d = \frac{V_{ov}}{R_q + R_d} \sim \frac{V_{ov}}{R_q} \tag{3.13}$$

The avalanche is "quenched" at this point, and the cell returns to its initial conditions with a recharge time constant:

$$\tau_r = R_q(C_q + C_d) \tag{3.14}$$

76

The ratio of the avalanche's total charge to its elemental charge q can be used to express the SPAD's gain G:

$$Gain = \frac{avalanche_{charge}}{q} = \frac{V_{ov}(C_q + C_d)}{q} \tag{3.15}$$

3.5.2 Primary and secondary noise

SiPM detectors exhibit two types of noise: primary and correlated (or secondary). The primary noise is caused by the Dark Count Rate (DCR), which refers to false signals generated by thermally induced electron-hole pairs triggering an avalanche (as shown in Figure 3.11(a)). The DCR strongly depends on temperature and decreases by a factor of 2 every 10K temperature drop. The DCR can be reduced by using specific production processes and materials with high purity. Correlated noise includes Afterpulsing and Crosstalk. Afterpulsing refers to events following the main event (signal or Dark Count event) due to the release of charges trapped in the high electric field region during the avalanche (an example of a Dark Count signal with an afterpulse is shown in Figure 3.11(b)). Typically, the same cell that produced the primary event is involved. The probability of afterpulse depends on the number of traps, release time constant, and recharge time, which can be reduced by selecting the material, for instance by using a low-lifetime substrate.

3.5.3 Crosstalk

One form of noise that warrants specific attention in this study is crosstalk between neighboring Single-Photon Avalanche Diodes (SPADs) within the SiPM array. During an avalanche, up to 3×10^{-5} photons per charge carrier can be generated [9], which can reach adjacent cells and cause a response in those SPADs. This effect can be mitigated by introducing trenches between the cells. As a result of this crosstalk, more SPADs may be triggered even if only one photon hits a single SPAD. The crosstalk can take two forms: direct or prompt optical crosstalk (as seen in Figure 3.11(c)), where isotropically emitted photons from an avalanche can reach neighboring cells and produce a signal, and delayed optical crosstalk, which occurs when an electron-hole pair is created in the bulk and subsequently diffuses to the active region, producing an avalanche with delays ranging from a few nanoseconds to microseconds (as seen in Figure 3.11(d)).
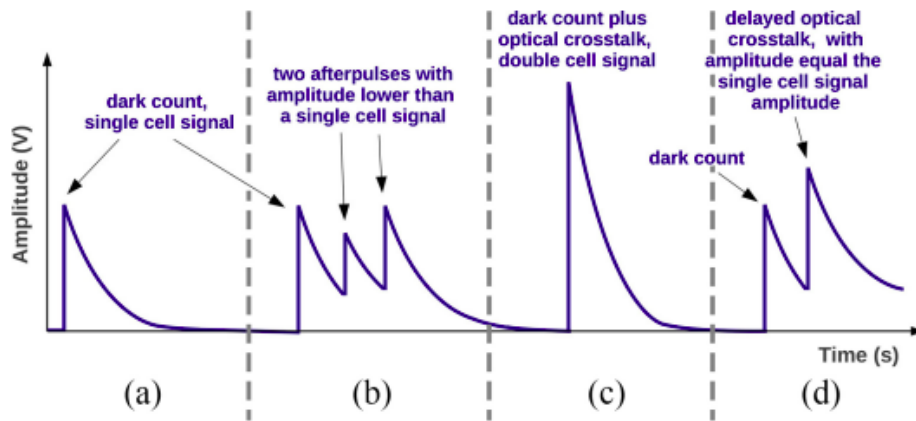
Figure 3.11: Analog SiPM output signal of different kinds of noise.

3.5.4 Background Reduction Techniques

The performance of a collider can depend on three main parameters:

- The center of mass collision energy E_{CM}

- The instantaneous luminosity, specifying the rate at which certain events are generated in the beam collisions (number of events per second $= L(t) \cdot \sigma_{event}$ with σ_{event} being the cross section of the event of interest)

- The integrated luminosity specifying the total number of events that are produced over a time interval

Optimizing the luminosity of a collider includes minimizing the experimental background. When working on SiPMs, the possible background reduction techniques are:

- *Cooling*, which reduces background effects due to thermal excitation by lowering operating temperatures

- *Annealing* cycles, which use high temperatures in order to repair radiation damage. This technique uses thermal excitation at high temperature to re-order out-of-lattice atoms to their former positions, recovering performance

- Correction on the *Timing* of the signal. By adding a 'fine' component to the 'coarse' time value, it is possible to perform cuts when acquiring a signal in order to have a better background rejection, which becomes more necessary as higher luminosities are achieved

The following chapter will investigate this last technique as a background reduction method for SiPMs.

Chapter 4

Data Analysis

4.1 ALCOR
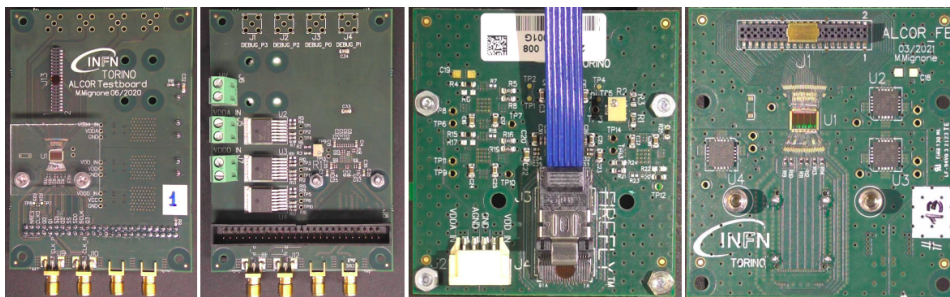
Figure 4.1: Photos of the ALCOR chip mounted on the front-end card.

ALCOR (A Low power Chip for Optical sensors Readout) - Figure 4.1, is the prototype of a mixed-signal ASIC (Application Specific Integrated Circuit) for SiPM detectors, developed by the INFN Torino for the DarkSide [1] experiment at the Laboratori Nazionali del Gran Sasso.
The chip performs amplification, signal conditioning and event digitisation, and features fully digital I/O.
Its core consists of 32 parallel pixels arranged in a matrix of 4×8, as shown in Figure 4.2.

Figure 4.3 illustrates the structure of the pixel. Each individual pixel incorporates a dual-polarity front end, utilizing the Regulated Common Gate (RCG) framework,

---

[1]DarkSide-50, a direct search for dark matter operating in the underground Laboratori Nazionali del Gran Sasso (LNGS) and searching for the rare nuclear recoils possibly induced by weakly interacting massive particles (WIMPs) [43].

which enables the reading of either the anode or cathode signal. The amplified signal is then directed into two separate branches, both of which are equipped with a leading-edge discriminator. This discriminator employs a basic voltage comparator, with its threshold set to a desired voltage. When the rising edge of the analog pulse surpasses this threshold, the comparator generates a logical pulse.

To enhance the pixel's counting capability and eliminate randomness in the incoming photons, a group of four Time-to-Digital Converters (TDCs), employing analog inter-polation techniques, is implemented on each pixel. The data generated for each event is gathered by an End of Column circuit, and the complete digitized data is ultimately transmitted off-chip using four LVDS (Low Voltage Differential Signaling) transmitters [44].
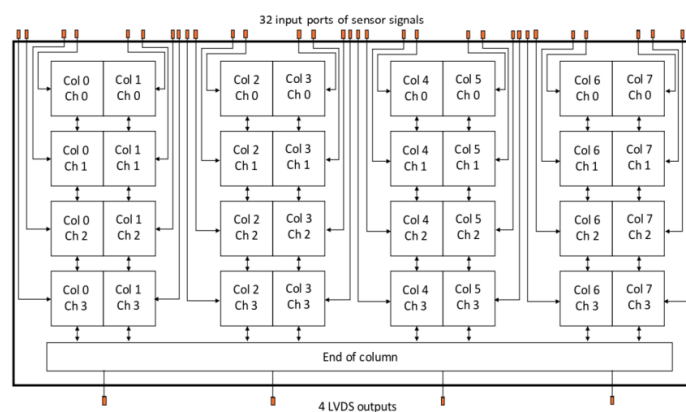
Figure 4.2: Architecture of the ALCOR chip.
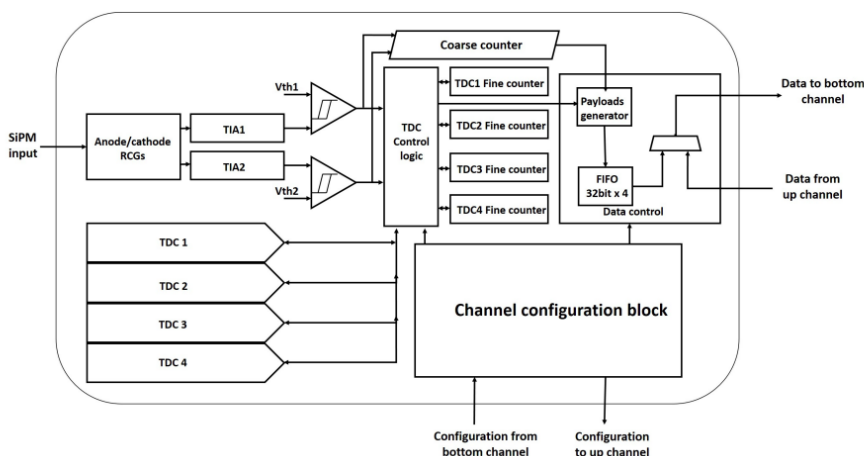
Figure 4.3: Architecture of the ALCOR readout pixel.

81
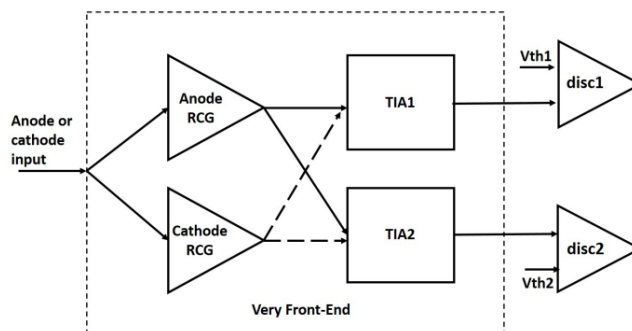
Front End

Figure 4.4: Front End Architecture.

The front end, depicted in Figure 4.4, is constructed using complementary Regulated Common Gates (RCGs) to facilitate the readout of both anode and cathode signals. Subsequently, the selected signal, whether from the anode or cathode RCG, is split into two separate branches. To convert the current signal to a voltage signal, a TransImpedance Amplifier (TIA) is employed, utilizing a common source amplifier.

The front end comprises two distinct output stages, each with its own gain and corresponding discriminator threshold voltages. Additionally, the end circuit is designed to operate with dual threshold settings, as illustrated in Figure 4.5. The four Time-to-Digital Converters (TDCs) are controlled to ensure the desired conversions are achieved.
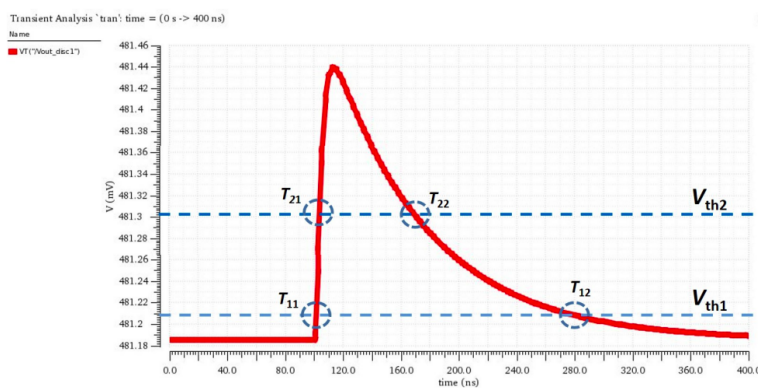
Figure 4.5: Working principle of dual threshold voltages.

To achieve a more precise measurement of the leading edge timing (T_{11}), a lower threshold voltage (V_{th1}) can be set, taking advantage of the faster signal slope. The advantages of utilising a lower threshold voltage include intercepting the signal rising

82

edge at a point where it is faster (as the signal amplitude grows, the derivative of its rising edge decreases) and reducing the presence of time walk effects.

The energy information derived from the Time over Threshold (ToT) measurement can be utilized for time walk calibration.

The time walk is an effect given by the presence of signals with different amplitude. Depending on the signal amplitude, its derivative describing the signal rising edge varies, as the rising time remains constant (while the signal amplitude does not). This effect causes some signals to trigger the TDC earlier than others. A graphic example of the time walk is given in Figure 4.6.
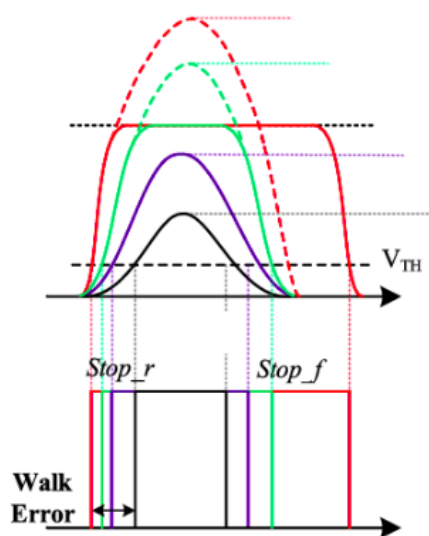
Figure 4.6: Illustration of the Time Walk effect.

The resolution of ToT measurement is primarily influenced by the falling edge measurement (T_{12}), calculated at a point in which the slope is less steep.

In order to measure the falling edge time (T_{22}) with improved accuracy, a higher threshold voltage (V_{th2}) can be employed, as it provides a better falling edge slope compared to the previous measurement, due to its distance form the baseline, hence, noise disturbance. Additionally, by measuring the leading edge times (T_{11} and T_{12}) using dual thresholds, the slew rate of the signal can be determined. This information can be utilized to characterize the bandwidth of the front end circuit and the sensor capacitance.

Discriminator and TDC

Figure 4.7 displays the detailed transistor-level schematic of the ALCOR leading-edge discriminator. The threshold voltage of the discriminator can be adjusted within a range of 550 mV to 878 mV, with a step size of 2 mV. This discriminator is connected to the

output of the very front end section and serves the purpose of generating the CMOS (complementary metal-oxide semiconductor) trigger signal required for the analog-to-digital conversion process.
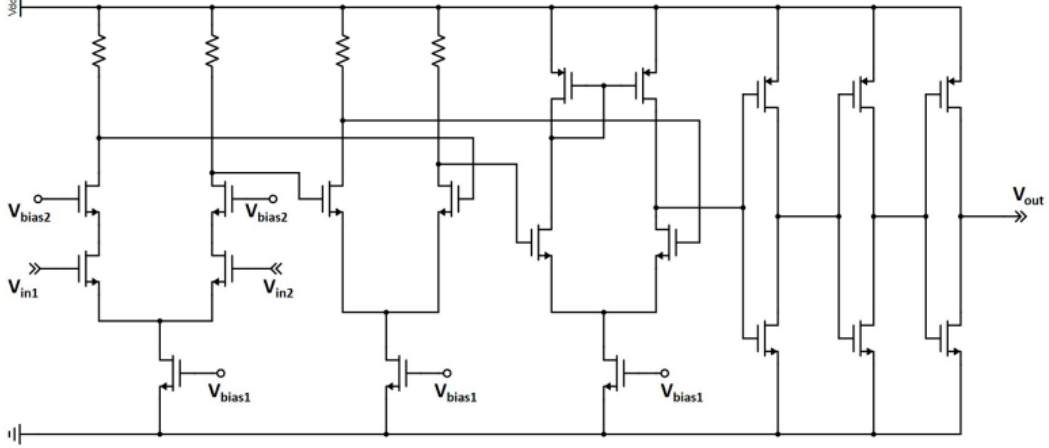

Figure 4.7: TDC schematic in ALCOR.

Figure 4.8 illustrates the operational principle of the TDC (Time-to-Digital Converter) block. Prior to each measurement, the voltages of capacitors C_1 and C_2 are reset to a reference voltage V_0. The switch s_1 is closed, initiating the charging of capacitor C_1 with the coarse current I_{coarse} when the discriminator is triggered. Once the charge process commences, s_1 is turned off, and the charging halts at the next rising edge of the clock signal. The voltage value V_A attained by C_1 is recorded, with the rising edge of the clock serving as the coarse time reference, captured by a 15-bit counter.

During the conversion phase, switch s_2 is closed, allowing capacitor C_2 to be charged with a smaller current I_{fine}. The control state machine halts the conversion when the latched comparator changes its state, and the fine time stamp is recorded using a 9-bit counter.

Both capacitors, C_1 and C_2, have identical values, and the interpolation factor is determined by the ratio of the coarse and fine currents.

With the relation:

$$I_{coarse} = 64I_{fine} \tag{4.1}$$

or

$$I_{coarse} = 128I_{fine} \tag{4.2}$$

the bin of fine time resolution is 50 ps or 25 ps.

84
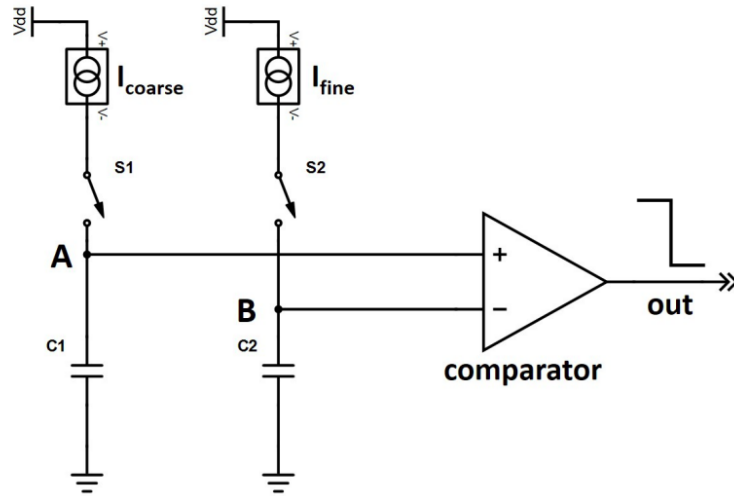
Figure 4.8: Discriminator schematic in ALCOR.

When the master clock operates at its highest frequency of 320 MHz, the TDC (Time-to-Digital Converter) exhibits a time bin size of 50 ps and a dead time of 150 ns. The fine time information, captured by the TDC, is combined with the coarse time information derived from the system clock. The system clock's coarse time is latched using a 15-bit gray-encoded counter, and these two sets of information are integrated to provide a comprehensive time measurement [44].
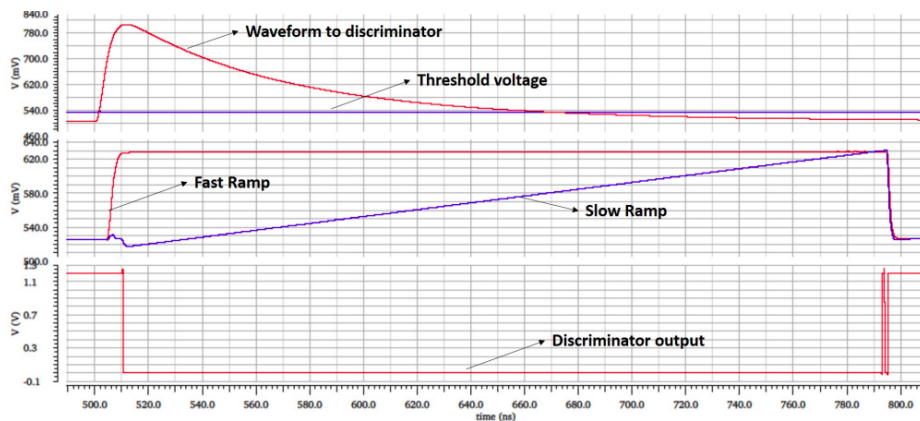

Figure 4.9: ALCOR TDC simulation.

Figure 4.9 describes the simulation of TDC in ALCOR, to see the behaviour of the analogue waveform, discriminator output and two voltage ramps.

85

4.1.1 Full pixel operation and data transmission

Five working modes of the pixel are configured by the pixel control logic, distributing the working of four TDCs.

1. OFF

2. LET: the rising edge of TRG1 (T_{11} as referred to in section 4.1)

3. TOT: the rising and falling edges of TRG1 (T_{11} and T_{12})

4. TOT2: the rising edge of TRG1, the falling edge of TRG2 (T_{11} and T_{22})

5. SR: rising edges of TRG1 and TRG2 (T_{11} and T_{21})

Where the TRG1 and TRG2 are trigger signal of two discriminators respectively.
The OFF mode will turn off the four TDCs, no conversion is carried out in this mode. The four working modes described in points 2-5 have been discussed in the front end section.
LET mode is used for photon count, achieving high timing resolution and high count rate by using the four TDCs sequentially.
The ToT and $ToT2$ mode are used for energy measurement, and $ToT2$ mode can have a better resolution by dual voltage setting.
SR mode is used to characterize the front end bandwidth and sensor capacitance.

Figure 4.10 shows the last four different working modes and the TDCs distribution.

After the completion of the conversion process, the data control logic produces a 32-bit payload that comprises the time-stamp, channel ID, and the corresponding TDC address. This arrangement is depicted in Figure 4.11.

Furthermore, if all four TDCs are occupied at the occurrence of a new event, an additional register is utilized to store the Status Word. This Status Word includes the channel ID, TDC number, the count of cases to be discarded, and the number of single event upset (SEU) errors. The generated payloads are initially queued and stored in a First-In, First-Out (FIFO) register within the respective channel. Subsequently, these payloads are transmitted to the peripheral region of the chip.

To facilitate this data transmission process, the End of Column (EoC) circuit is employed. The EoC serves as an interface between the channels within the chip and the external world. It collects data from the channels and ensures its transfer to the periphery.

The schematic diagram illustrating the data transmission within the ALCOR chip is presented in Figure 4.12.

Each column within the ALCOR chip is equipped with its own dedicated Finite State Machine (FSM) responsible for scanning the column and reading pixels with valid stored data. Ownership of the bus is exclusive to the channel that stores the event data.
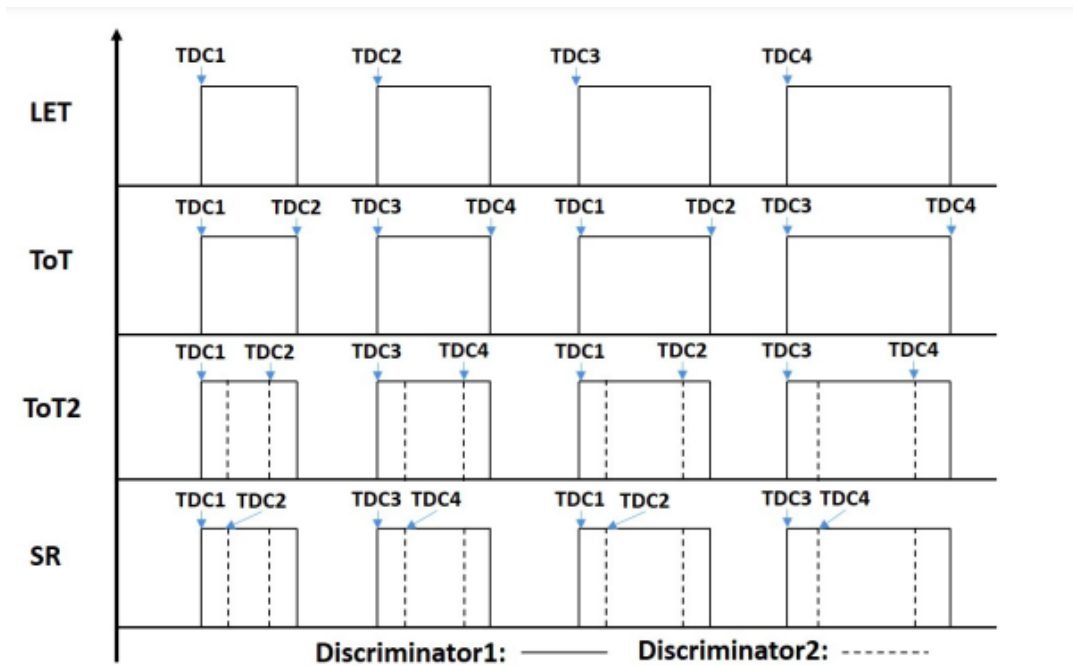
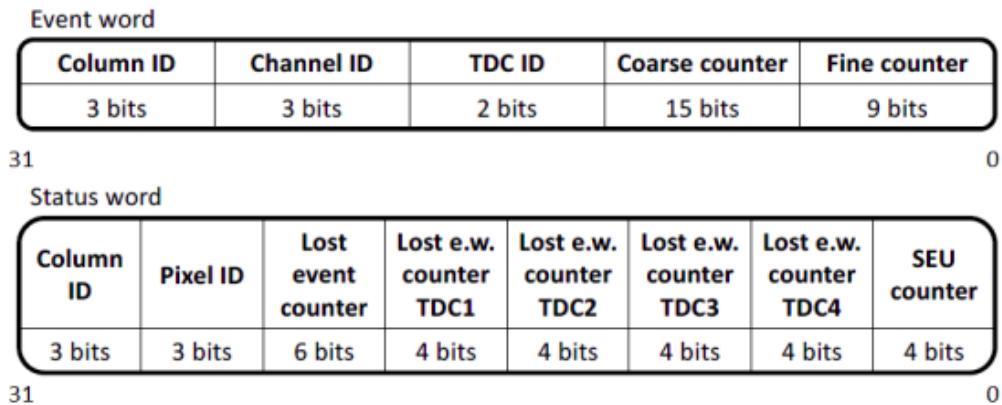Figure 4.10: TDCs distribution with different working modes.

Event word

Column ID	Channel ID	TDC ID	Coarse counter	Fine counter
3 bits	3 bits	2 bits	15 bits	9 bits

31   0

Status word

Column ID	Pixel ID	Lost event counter	Lost e.w. counter TDC1	Lost e.w. counter TDC2	Lost e.w. counter TDC3	Lost e.w. counter TDC4	SEU counter
3 bits	3 bits	6 bits	4 bits	4 bits	4 bits	4 bits	4 bits

31   0

Figure 4.11: Format of event payload and status word.

During each read cycle, only a specific set of data can be extracted from each channel to prevent buffer overflow in other channels. Newly entered data can be processed and stored during the readout cycle for subsequent retrieval. However, the existing readout logic does not inherently sort the cases according to their time order. To address this, an additional Finite State Machine (FSM) is employed to sort the data from the two
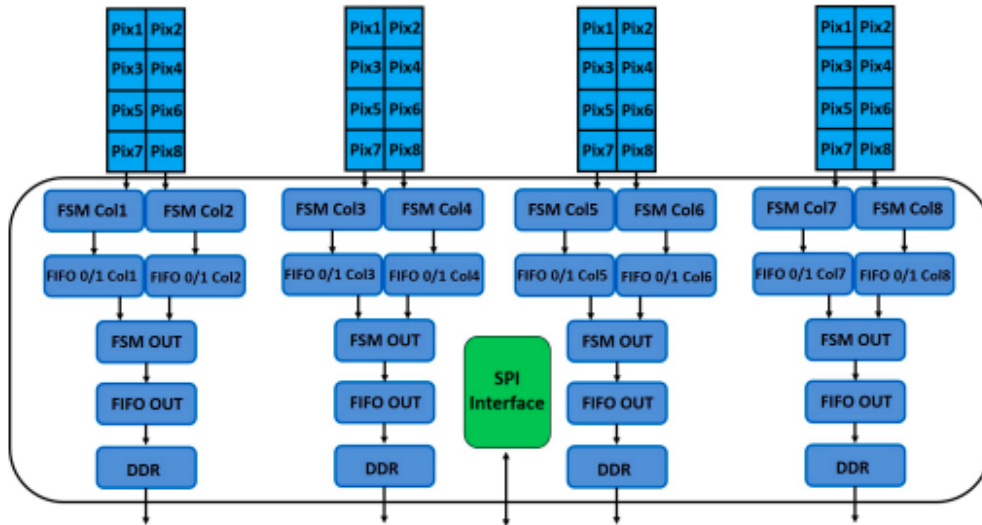
Figure 4.12: ALCOR data transmission system.

columns based on coarse time information. The sorted data is then outputted to the next stage.

Configuration signals for the End of Column (EoC) circuit are provided through a Serial Peripheral Interface (SPI) interface. Data transmission off-chip is facilitated by four LVDS (Low Voltage Differential Signaling) drivers, with each pair of columns (8 pixels) sharing one LVDS transmitter [44].

The ALCOR chip integrates 32 readout channels, with each pixel having dimensions of approximately 500 μm $\times$ 500 μm . The overall chip size is 4.95 mm $\times$ 3.78 mm. The analog and digital components are situated in separate regions, and adjacent readout pixels are mirror assembled to maintain distance between the analog and digital parts. At the full chip level, the analog inputs are positioned on top, while the digital outputs are located at the bottom. These strategies minimize crosstalk from the digital blocks to the analog blocks. The readout channels are arranged in a squared matrix configuration, with 32 channels mounted per carrier board [44].

4.2   Beam Test

The data analysed in this chapter was obtained from a beam test performed on SiPM arrays coupled to the dRICH detector prototype using the PS beam from the T10 area (Figure 4.13) located in the East Area on the Meyrin site of CERN, Geneva during the week between October 12th and 19th 2022.

The objective of this test beam was investigating the performance of different SiPM sensors as a possible option for dRICH detector.

The key point for R&D on the dRICH optical readout with SiPMs is demonstrating the capability to measure single photons produced by Cherenkov radiation and keeping dark count rate (DCR) under control (ring imaging background) despite radiation damages.

The beam line is located in building 157, as shown in Figure 4.14 and provides beams of charged particles (p and π^+ in positive mode; π^- in negative mode) in a momentum range from 1 GeV/c up to 12 GeV/c, produced due to interaction of a primary 24 GeV/c proton beam with the target. The beam structure foresees typical intensities in the order of $10^3 - 10^6$ particles per extraction cycle (spill) for a spill duration of $\sim$ 400 ms with a repetition period of about 20s [45].
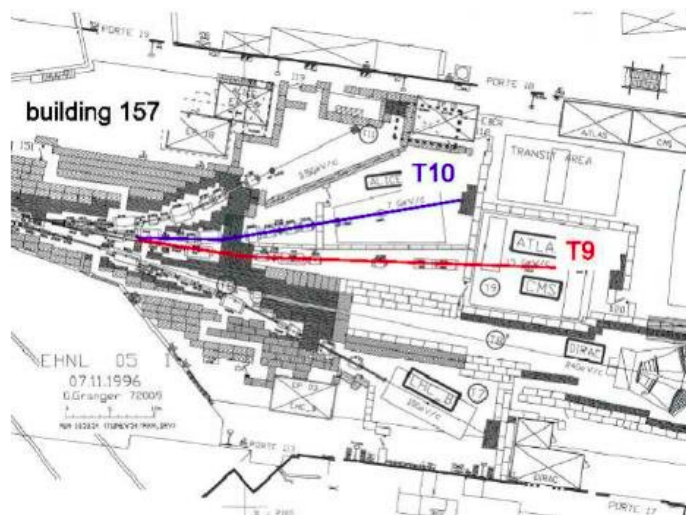
Figure 4.13: T10 in building 157 in the East Area.
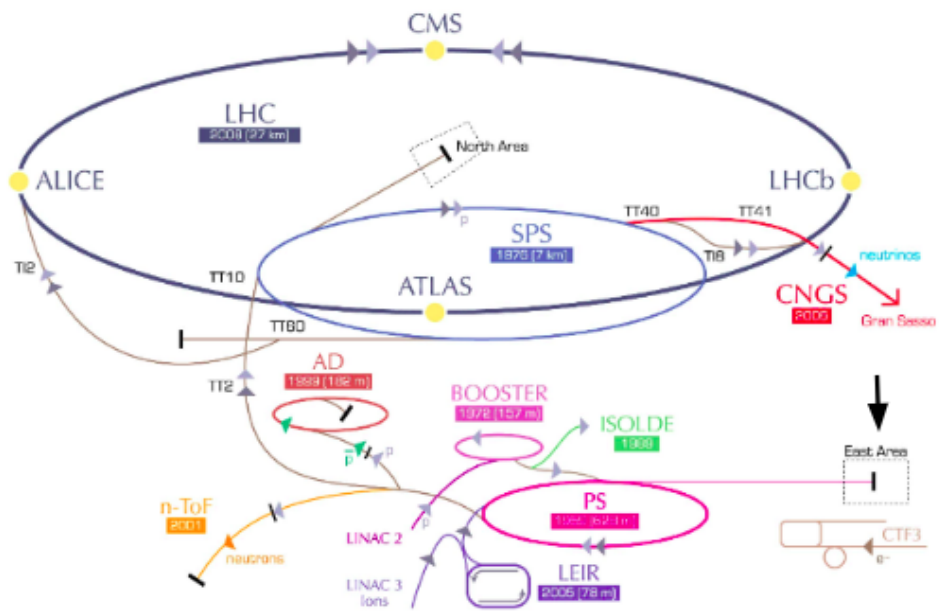
Figure 4.14: CERN complex scheme with arrow pointing at the East Area (bottom-right).

4.2.1 Experimental Set Up

The prototype consists of two concentric cylinders with different radii, placed in sequence. Each cylinder is filled with gas and is equipped with a mirror at its base opposite the direction of the incoming beam. Their function is the reflection the Cherenkov-photons created in the detector by the passage of charged particles in order to focuse them on the photon detector array placed upstream of the dRICH prototype.

A charged particle crossing the dRICH initially passes through an aerogel box and produces a Cherenkov-photon cone.

The particle also passes through the gas-filled detector producing a Cherenkov-photon cone of about 2 degrees aperture. The first mirror has a central hole, to allow the photons produced in the gas at small angles to fly towards a second spherical mirror and be focused back on the same photon detector array. The information of the two imaged Cherenkov rings combined with the beam momentum will allow identification of pions, kaons and protons.
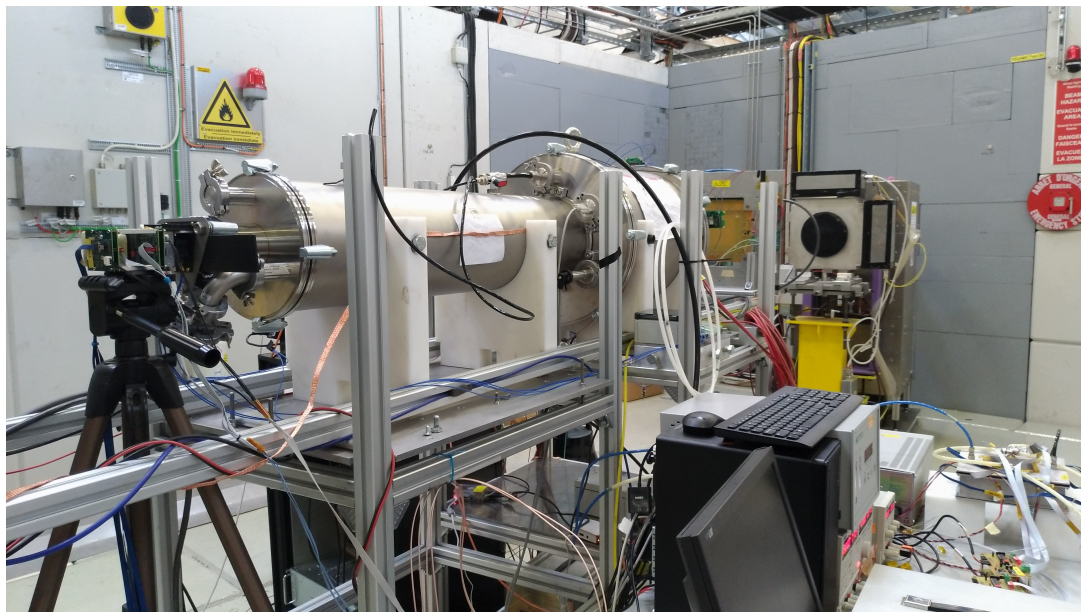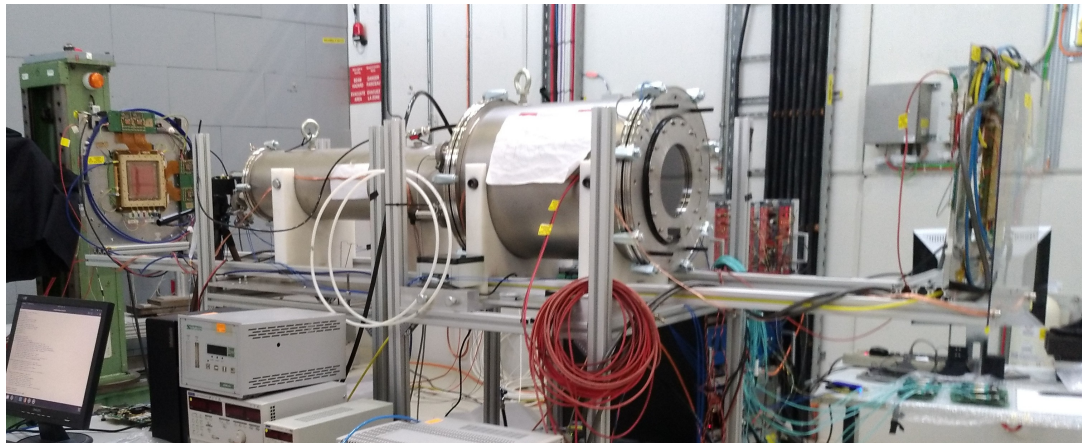
Figure 4.15: Top: dRICH upstream view. The beam enters from the right. Bottom: dRICH downstream view.

The instruments employed in the beam test included:

- 6 carrier boards, each hosting a matrix of SiPMs:
  4 carrier boards were placed inside the dRICH readout box for the detection of light produced by Cherenkov radiation (Imaging SiPMs).
  2 carrier boards, each coupled with a plastic scintillator, were placed downstream the dRICH prototype for the measurement of a reference particle time (Timing SiPMs).

- ALCOR chips.
  Each SiPM carrier board is coupled with an ALCOR front-end card hosting the ALCOR chip.

- 2 Peltier cells
  The four SiPM carrier boards placed inside the dRICH readout box are cooled down to $T = -30°C$ and kept a this temperature for the duration of the beam test through the thermoelectric effect provided by the Peltier cells. The Peltier cells are placed inside the dRICH readout box on the back side of the SiPM carrier board. One Peltier cell is used to cool two SiPM carrier boards. Excess heat created by the thermoelectric cooling is removed by water circulating in a cooling block (chiller) connected to the hot side of the Peltier module.

- 6 Adapter boards
  Electronic boards responsible for adaptation between the SiPM carrier board connector and ALCOR. It also hosts electronic circuits which regulate the sensor V_{bias} values which supplies them with power.

- 4 Master logic boards
  A board that hosts a microcontroller which is responsible for communication with circuits on the adapter. It sends instructions to the adapter as well as receiving information from it, such as the working temperature of the sensors.

- 1 FPGA (Field-Programmable Gate Array)
  FPGAs consist of programmable logic blocks and configurable interconnects, which allow designers to create custom digital circuits without the need for custom silicon. These chips can be programmed to perform a wide variety of tasks [41]. In the case of this experiment, its function was collecting data received from ALCOR and transferring it to a computer.

- QL355TP Power Supply for the front-end boards

- TSX1820P Power Supply used to bring power to the Peltier elements;

- PLH250-P Power Supply used to bring the high voltage to the sensors;

- 1 Workstation composed by computers provided with a personalised analytics and monitoring program written with Grafana [42].

The objective of this setup, as is the goal of the test beam is the study of the response of different SiPM to the detection of Cherenkov light signals in order to evaluate their performance in an accelerator environment.

4.3 SiPM Carrier Boards

As mentioned in the previous paragraph, the tested SiPMs were mounted on 6 carrier boards: 4 carrier boards dedicated to Imaging and 2 dedicated to Timing. As shown in Figure 4.16, the SiPM are arranged on each carrier board in a matrix configuration.
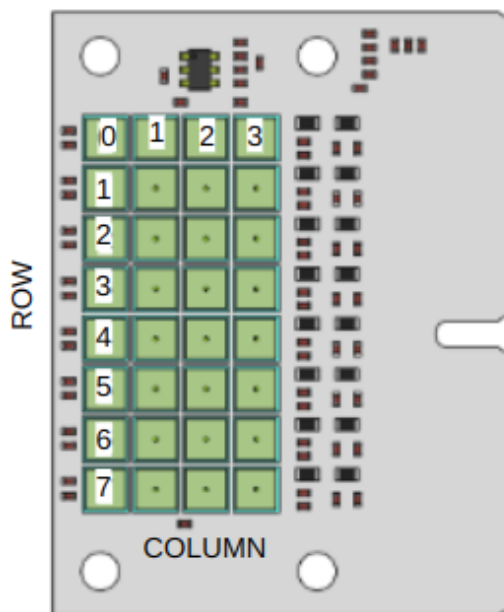
Figure 4.16: Placement of each SiPM matrix on its carrier board.

Figure 4.16 shows a SiPM matrix formed by 8 rows and 4 columns, for a total of 32 SiPMs.

This description fits all SiPM matrices except for the FBK brand SiPM matrix, which contains only 6 rows instead of 8 (for a total of 24 SiPMs) as the dimension of these SiPMs are larger than the SiPMs of other brands tested.

Further details about the employed SiPM brands and characteristics will be given in sections 4.3.1 and 4.3.2.

SiPM Index Notation for Data Analysis

The row and column indices can be combined as one 'channel' index which allows to describe all SiPMs on each carrier board with a single index instead of the combination of the two. The channel index, ranging 0-31, will describe all 32 hosted SiPMs on the carrier boards.

Naturally, this index will only reach 24 in the case of the FBK SiPM matrix which hosts 6 rows instead of 8.

Since each SiPM is readout by 4 TDCs, the channel index will need to be multiplied by 4 to describe the readout value of each TDC over all the tested SiPMs.

To describe all SiPMs studied in the beam test, the channel index must be multiplied by the 'chip' index (ranging 0-5: 0-3 describing the imaging SiPM carrier boards and 4-5 describing the reference timing SiPM carrier boards) - to describe the SiPM sensors on all 6 carrier boards.

To condense all the above indices into one, the 'TDC calibration index' is introduced:

$$TDC\_calibration\_index = TDC + 4{}^*pixel + 16{}^*column + 128{}^*chip$$

This number, describing the readout from all 4 TDCs of each SiPM on all 6 carrier boards, ranges 0-767 and will be referred to as TDC calibration index through the data analysis description section.

4.3.1 Imaging SiPMs

The Imaging SiPMs are exploited with the function of detecting the Cherenkov light signal created inside the dRICH. The signal in the dRICH is formed by a Cherenkov-photon cone, which reflected onto the SiPM carrier boards formes a circumference.
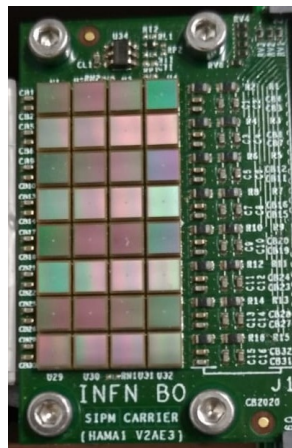The boards hosting the SiPM matrices are represented in Figures 4.17 - 4.20.

Figure 4.17: Carrier board ('chip' index = 0) hosting the HAMA1 brand SiPMs.

Figure 4.18: Carrier board ('chip' index = 1) hosting the FBK brand SiPMs.
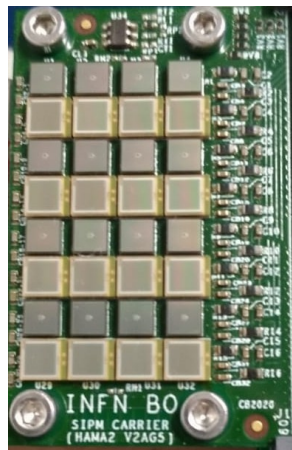
Figure 4.19: Carrier board ('chip' index = 2) hosting the HAMA2 brand SiPMs.
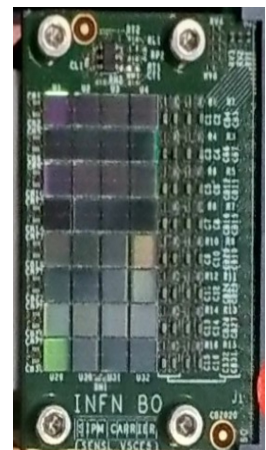
Figure 4.20: Carrier board ('chip' index = 3) hosting the SENSL brand SiPMs.

The details of the utilsed SiPMs are illustrated in Table 4.1.

CHIP Index	SIPM Brand	SENSOR	uCELL (μm)	V_{bd} (V) (at T = -30°C)	PDE (%)	DCR (kHz/mm^2) (at T = -30°C)
0	HAMA1	S13360 3050VS	50	53	40	55
0	HAMA1	S13360 3025VS	25	53	25	44
1	FBK	NUV-HD-RH	15	32	27.5	40
1	FBK	NUV-HD-CHK	40	32	42	60
2	HAMA2	S14160 3050HS	50	38	50	NA
2	HAMA2	S14160 3015PS	15	38	32	78
3	SENSL	MICROFJ 30035	35	24.5	38	50
3	SENSL	MICROFJ 30020	20	24.5	30	50

Table 4.1: Imaging SiPM characteristics.

The imaging SiPM matrices were fixed to a box (Figure 4.21) which was then placed between the beam source and the dRICH (Figure 4.22) to allow them to detect and record the reflected Cherenkov light signals produced within it.
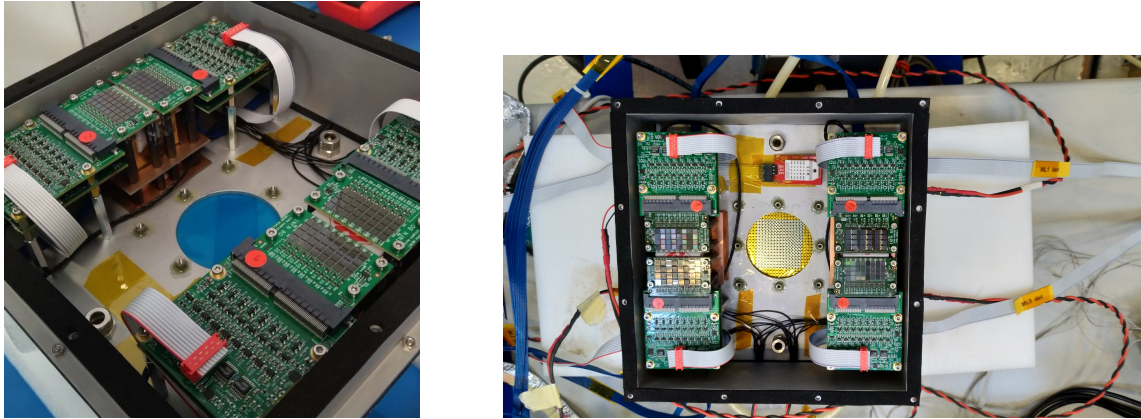
Figure 4.21: View of the 4 SiPM carrier boards fixed in the box.
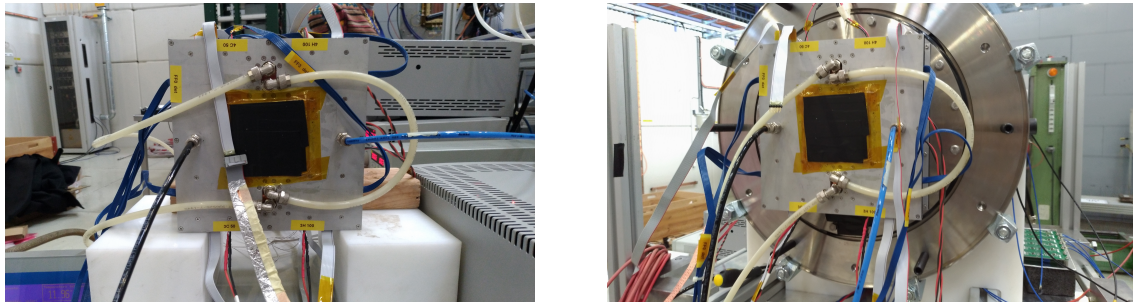
Figure 4.22: Zoom on the closed box (left) which is then shown mounted in front of the dRICH (right).

Their working principle is represented in Figure 4.23: the ring represents the Cherenkov light cone reflected onto the photon detector array, while the yellow pixels represent the SiPMs recording a hit.

The figure confirms the expected behaviour of the imaging SiPMs: the pattern of SiPMs recording a hit approximate the circumference created by the cone of Cherenkov light.
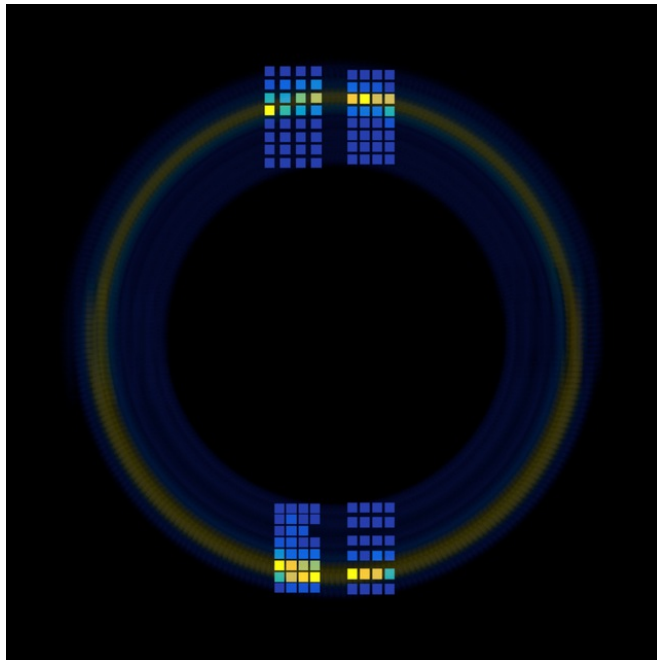
Figure 4.23: HAMA1, FBK, HAMA2, SENSL working principle.

4.3.2 Reference Timing System

The function of these Reference Time SiPMs is providing the reference time associated with the passage of a beam particle in the dRICH prototype.

The reference timing system described is composed by two 32 SiPM matrices placed on two separate carrier boards, placed closely one in front of the other.

Each carrier board is coupled to a scintillator in order to receive a signal at the passage of a particle.

The whole system is supported by a tripod and positioned downstream of the dRICH as to avoid chances interfering with the imaging measurements. However, the placement of the reference time system is arbitrary.

The details of the utilsed SiPMs are illustrated in Table 4.2.

CHIP Index	SIPM Brand	uCELL (μm)	V_{bd} (V) (at T = -30°C)	PDE (%)	DCR (Mcps) (at T = -30°C)
4,5	AFBR-S4N33C013	3.14×3.14	26.9	54	1.0

Table 4.2: Timing SiPM characteristics.

The value of the Reference Time T is given by the following formula:

$$T = \frac{T_4 + T_5}{2} \tag{4.3}$$

where T_4 and T_5 represent the average registered time coincidence signal calculated on all 32 SiPMs on the Timing carrier boards (described by the 'chip' indices 4 and 5).

T_4 and T_5 are calculated as:

$$T_{4,5} = \frac{1}{N} \sum_{i=1}^{N} t_{4,5}^{SiPM} \tag{4.4}$$

where the N index is employed to describe all SiPMs on each carrier board and ranges 0-31.

The timing SiPM matrices and their placement are shown in Figure 4.24 (front view) and 4.25 (above view).
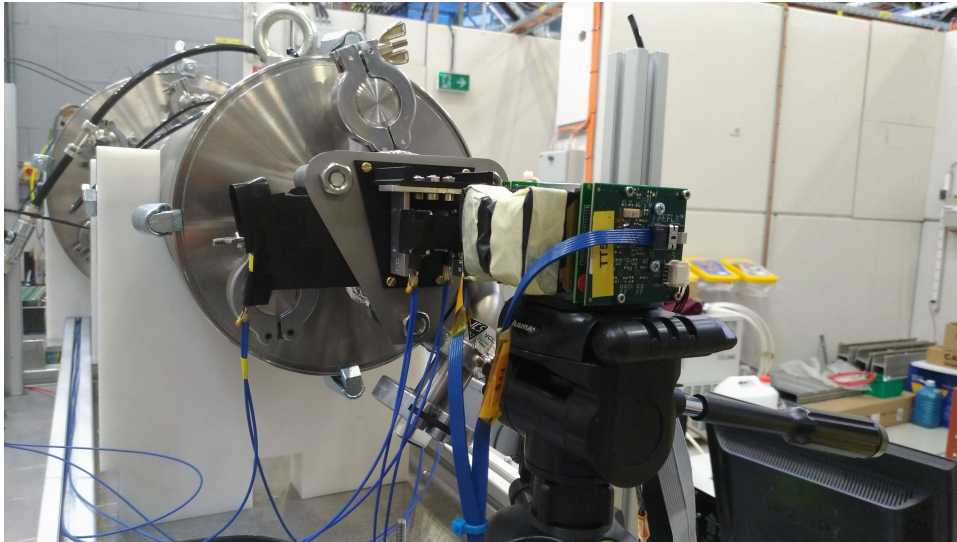

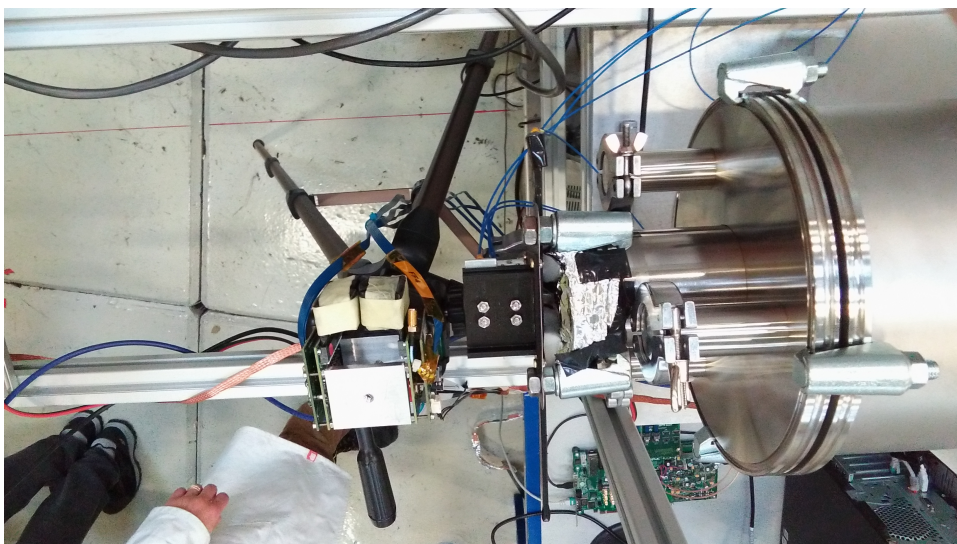Figure 4.24: Front view of timing scintillators places downstream of the dRICH with respect to the beam.

Figure 4.25: Above view of timing scintillators places downstream of the dRICH with respect to the beam.

4.4   ALCOR Time

As mentioned in section 3.5.4, a refinement on the signal time measurement becomes increasingly essential as the luminosity of the accelerator environment increases.
Higher signal rates imply higher background disturbance, so a more precise measurement of the time value is necessary to create cuts that allow a better background rejection.
To reconstruct the time of a hit, ALCOR uses the *rollover*, *coarse* and *fine* fields and is able to express the time of the hit in *ns*.
The coarse counter measures the hit time in terms of the 320 MHz clock cycle. Given that the coarse counter has a 15 bit size, only up to 32768 values can be stored.
When the coarse counter resets, a rollover is increased.
Phase is the measured phase of a recorded signal with respect to the 320 MHz ALCOR clock cycle. The value of *phase* can be defined starting from the *fine* TDC value provided by the ALCOR chip after the necessary calibration parameters are known. A discussion of the determination of the calibration parameters is needed for the measurement of the *phase* component is the subject of this work and will be discussed further.

The time value of a registered hit is expressed as:

$$t = (coarse - phase) \cdot 3.125ns + rollover \cdot 102.4\mu s \tag{4.5}$$

Where 3.125 ns and 102.4 μs are the clock and rollover periods, respectively.
In the following data analysis, the signal time-of-hit measurements calculated without the *phase* correction to the *coarse* time value is referred to as t_{raw} and defined as:

$$t_{raw} = coarse \cdot 3.125ns + rollover \cdot 102.4\mu s \tag{4.6}$$

Phase can be derived from the value of the fine TDC counter and the calibration parameters IF and CUT, which are defined as follows:

$$IF = MAX - MIN; \tag{4.7}$$

$$CUT = \frac{(MIN + MAX)}{2}; \tag{4.8}$$

The IF and CUT values are derived from the fit parameters MIN and MAX, which define the boundaries of the dynamic range of the fine time distribution.

This process requires finding a suitable function to fit the fine time distribution boundaries in order to obtain the MIN and MAX values of this range (see Figure 4.27 for a

graphic example of the described process).

The fit function chosen during the data analysis for this dissertation is based on the Fermi-Dirac distribution function, as the fine distribution described by each TDC resembled a square wave.

To deal with both the rising and falling front of the fine distribution to fit, a Fermi-Dirac 'double' step function was defined in the following way:

$$f = [0] \cdot \frac{1}{exp(\frac{x-[1]}{[2]}) + 1} \cdot \frac{1}{exp(\frac{[3]-x}{[4]}) + 1} \tag{4.9}$$

The *phase* term is then calculated by applying the following formula:

If $fine < CUT$:

$$phase = \frac{fine - MIN}{IF} \tag{4.10}$$

In the cases in which the *fine* time value exceeds that of the CUT value, an additional clock cycle is removed by applying the following modified version of eq.4.10:

If $fine > CUT$:

$$phase = \frac{(fine - MIN)}{IF} - 1 \tag{4.11}$$

The *phase* correction will be expressed, due to its definition, as a factor ranging from -0.5 to +0.5 to add to the coarse time.

4.5 Fine Time Analysis

Figure 4.26 shows the ALCOR TDC fine values for all TDC calibration indices describing the SiPMs employed during the test beam.

The 'TDC calibration index' represented on the x axis is used to create, define and record the calibration for each TDC.

As mentioned in section 4.1, each ALCOR channel is served by 4 individual TDCs and therefore the total number of TDCs to be calibrated for the beam test system is equal to 736.

The empty intervals in the graph in Figure 4.26 are due to the fact that the FBK SiPM matrix only presents 24 channels as opposed to the others who present 32.

It is possibe to notice that the *fine* range is roughly between the values of 37 and 100, which means that the typical phase binning corresponds to $3.125/63 \approx 50$ ps.

Notice also that the *fine* distribution for a given TDC seems to present some outliers, namely hits with *fine* value below or above the apparent minimum and maximum values of the distribution. The reason for such a behaviour will have to be investigated.

The outliers were included in the calibration process of this data analysis.

Cuts to exclude their contribution were performed only on the obtained phase values, once the calibraion process was finalised.
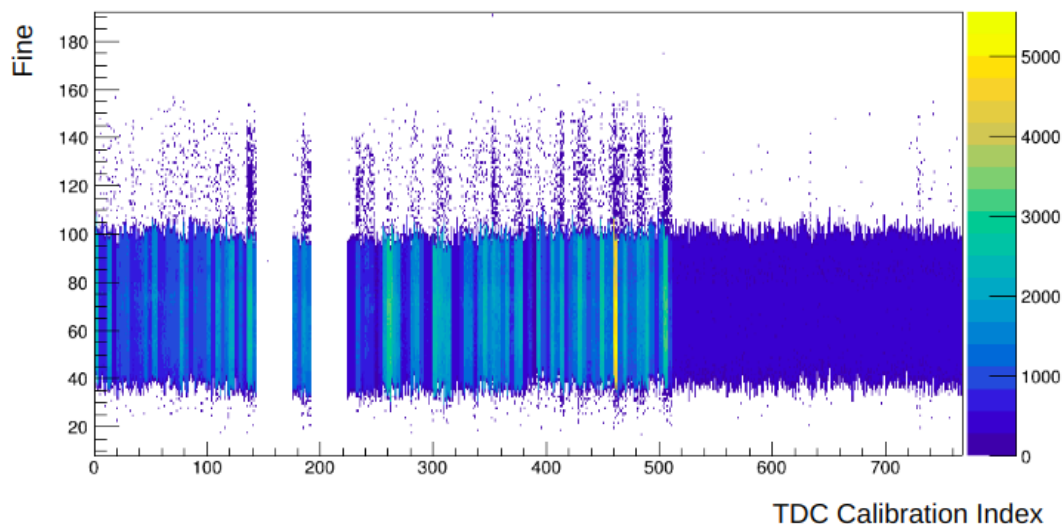

Figure 4.26: Range of the fine time values of each TDC calibration index.

105

Figure 4.27 shows the fine time distribution for a selected TDC calibration index: in this case, the index 0 describing the TDC 0 of channel 0 of the SiPM carrier board chip 0.
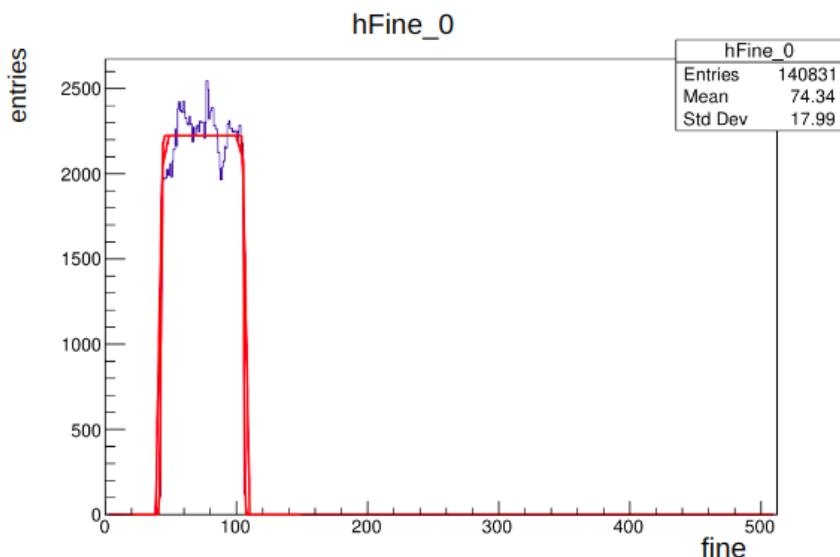

Figure 4.27: Histogram representing fine time distribution of the TDC calibration index 0.

Figure 4.28 shows a close up of the fit on the same histogram referenced in Figure 4.27.
The procedure of fitting the histograms describing the *fine* distribution with the equation described in eq.4.9 was used to obtain the MIN and MAX parameters of all TDC calibration indices.
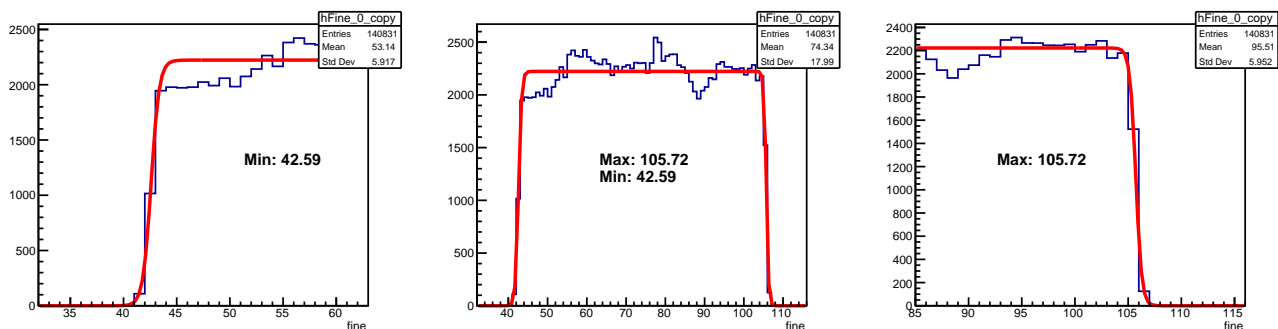
Figure 4.28: Close up of fit on histogram shown in Figure 4.27 This graph was used to check the performance of the fit on each histogram

Before proceeding with the use of the *fine* time calibration parameters MIN and MAX (which are needed to derive IF and CUT, as discussed in section 4.4) to obtain the measured phase of the hit with respect to the ALCOR clock cycle, an analysis of the MIN and MAX parameters calculated on each TDC calibration index of the analysed run was performed: Figure 4.29 represents the distribution of the MIN (top) and MAX (bottom) parameters calculated for each TDC calibration indices of the run.

This test was conducted to verify the consistency of the MIN and MAX parameter values throughout the whole run.

The fits performed on the MIN and MAX parameter distributions provided the following results: mean value of the MIN parameter equal to 37.09 and mean value of the MAX parameter equal to 100.1.

These vaues were considered reliable as the sigma values of the fit performed on the MIN and MAX distributions resulted being equal to 2.715 and 2.973 respectfully, which are both within an acceptable RMS of 3. No outliers have been observed in the distribution, which means that the calilbration process was succesful for all TDCs.

The parameter distributions well fitted by a Gaussian with $\sigma < 3$ demonstrates the uniformity of the various ALCOR TDCs.
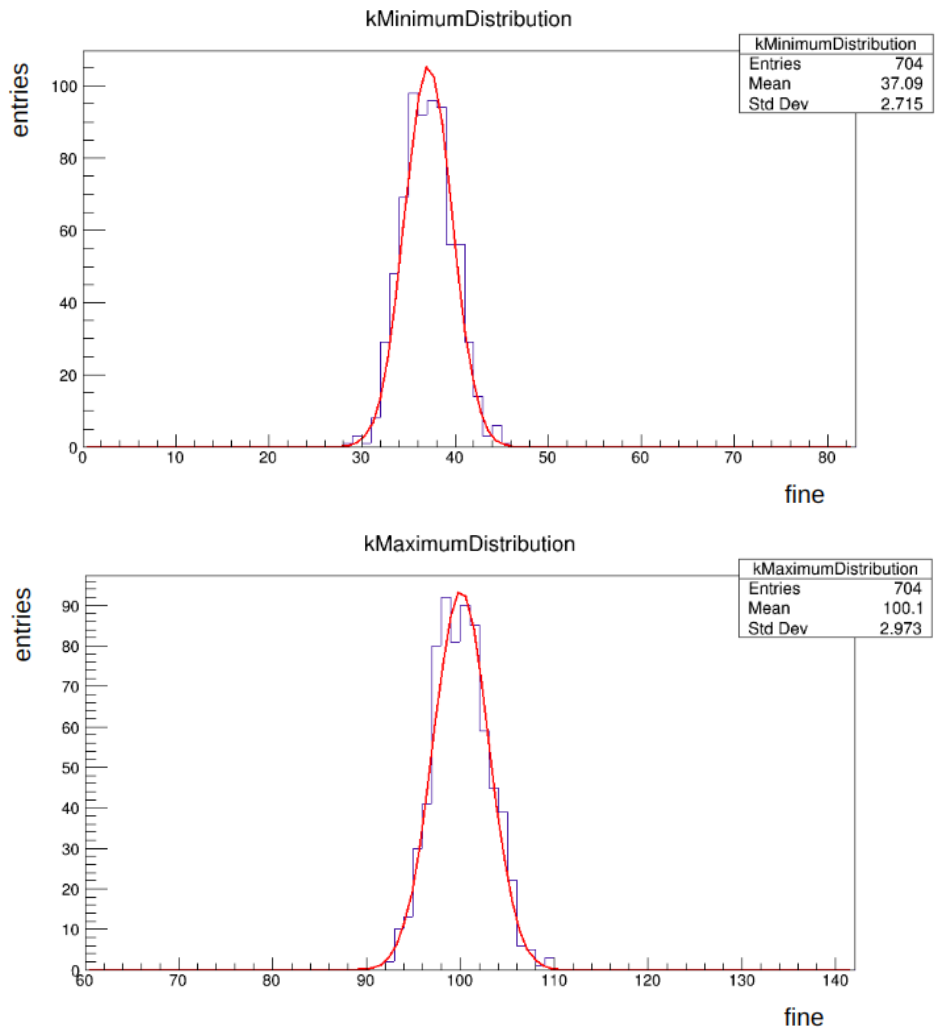
Figure 4.29: Fit on MIN parameter distribution (top) and MAX parameter distribution (bottom).

In addition to the checks on a single run, a comparison between two consecutive runs was also performed in order to verify consistencies of parameter measurements on different runs. The plots in Figure 4.30 show the distribution of the difference of MAX and MIN parameters calculated on the first and second run of the test beam.

The distributions show that the value of the MIN and MAX parameters measured in the two runs are consistent for most channels, despite a small number of outliers.
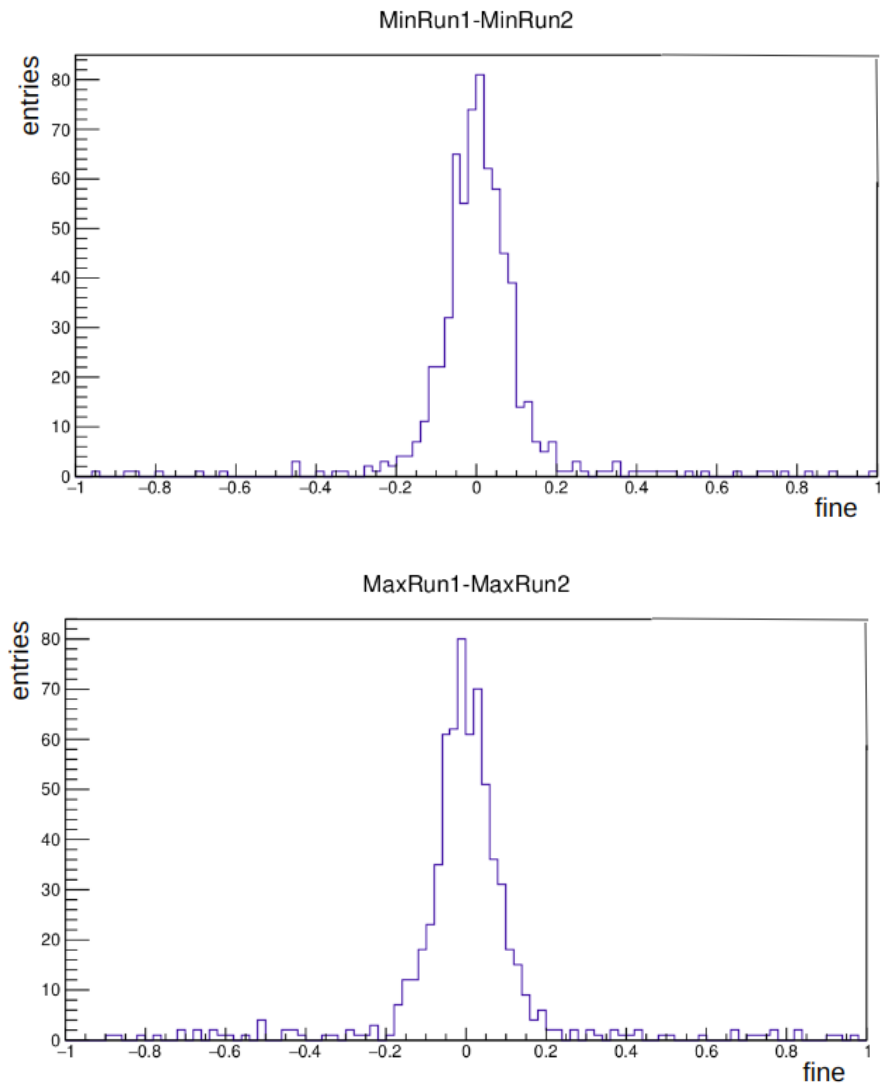

Figure 4.30: Difference between the MIN (top) and MAX (bottom) parameters calculated on the first and second run of the beam test.

Once all the MIN and MAX parameters of the run were obtained through this fit, the series of calculations in eq.4.7 were applied and we find, as expected, the calibrated phase correction distributed between [-0.5;+0.5] (Figure 4.31).
The few outliers can be noticed, which are due to the outliers highlighted by Figure 4.26).
After obtaining the phase values from the calibration, its outliers were cut, as their origin is unknown and requires further investigation.
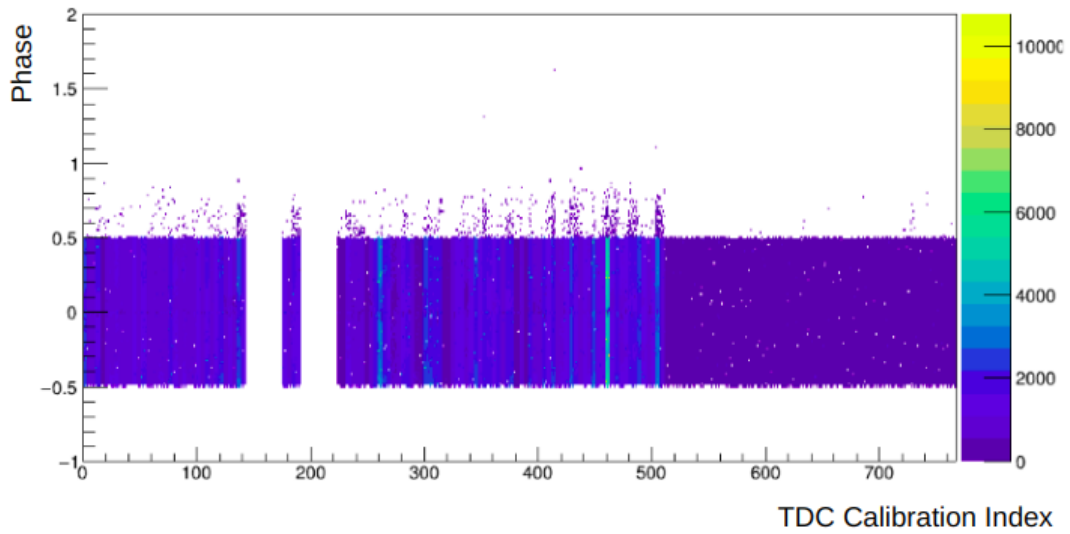

Figure 4.31: Phase correction terms.

To test further in depth and to visualise the performance of the calibration procedure previously outlined, several checks have been performed on dedicated channels.
The presence of a time coincidence highlights the fact that there is a signal observed in the imaging SiPM that corresponds to the passage of a particle registered by the timing system. This means that the coincidence signals in the imaging SiPM most likely corresponds to detected photons from the emitted Cherenkov radiation.

Figures 4.32 and 4.33 show the behaviour of the measured time value of a coincidence signal without the addition of the fine correction with respect to the Reference Time T measured by the Timing system.
The introduced value is defined as:

$$\Delta t_{raw} = t_{raw} - T \tag{4.12}$$

and is shown in the following graphs as a function of the fine and phase parameters.

In Figure 4.32, the measured raw time (eq.4.6) is used to highlight the dependence of the time coincidence signal as a function of the values of the TDC fine measurement. The plot represents the behaviour of the value given by the difference between the measured coincidence signal raw time and the Reference Time (defined in eq.4.3) as a function of the fine parameter.
As can be observed, the plot displays a behaviour which is dependant on the fine parameter. In particular, it is possible to notice a shift of the plotted data of approximately 3 ns along the y axis in proximity to the fine value.
This shift is due to the fact that a clock cycle is removed once the *fine* value exceeds the CUT value (eq. 4.11), which in this case, coincides with the *fine* value ≈ 65.
In Figure 4.33, the measured raw time (eq. 4.6) is used to highlight the dependence of the time coincidence signal as a function of the valued of the TDC phase parameter.
In this case as well, the plot displays a behaviour which is increasing with the phase parameter.
The shift of the data of approximately 3 ns along the y axis around the phase value 0.4 is due (as was the case in Figure 4.32) to an imperfection in the fine calibration approach which leaves a few cases in which the clock cycle that has not been removed.
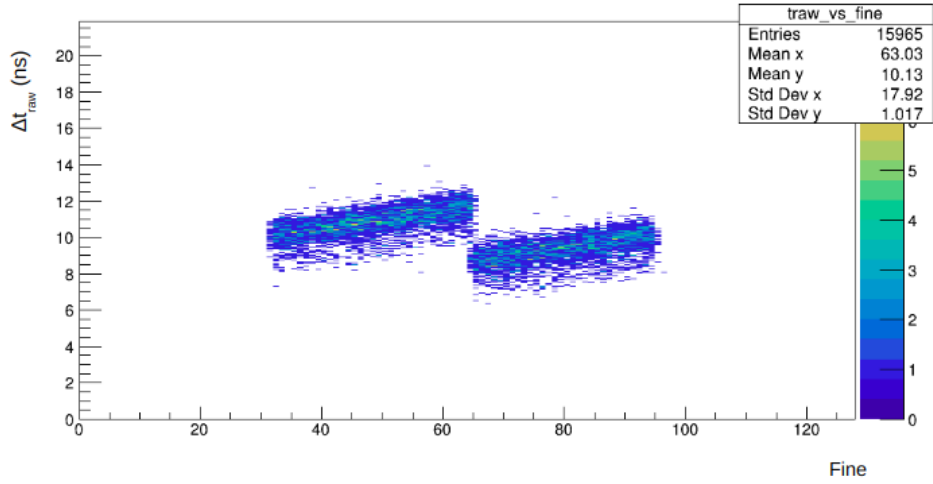
Figure 4.32: Difference between measured coincidence signal raw time t_{raw} and the Reference Time T as a function of the fine values.
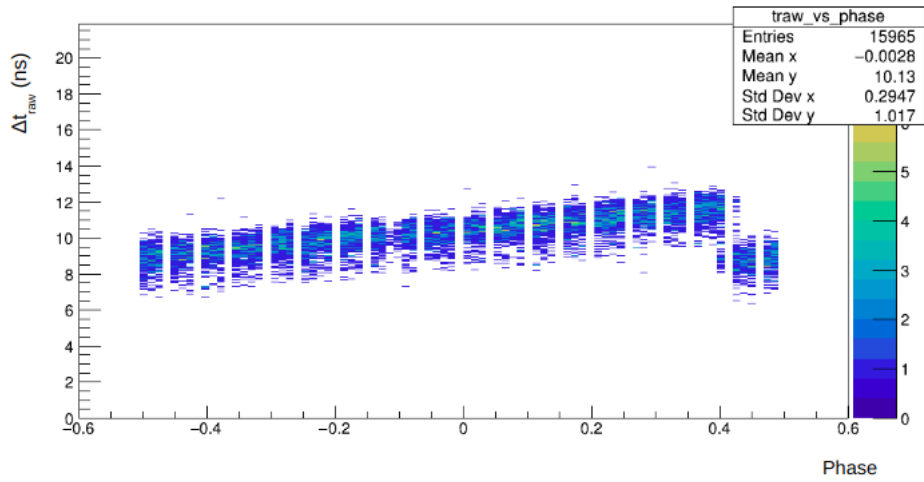

Figure 4.33: Difference between measured coincidence signal raw time and t_{raw} and the Reference Time T phase values.

The following graphs (Figures 4.34 and 4.35) differ from the two previous plots just by the *phase* correction factor which has been added to the t_{raw} value, in order to utilise the t value as defined in eq.4.5.

Hence, the following plots represent the value as defined:

$$\Delta t = t - T \tag{4.13}$$

in function of the *fine* and *phase* the parameters.

With the addition of the *phase* correction on the time coincidence signal measurements, the behaviour of the *fine* and *phase* plots which shows dependence on the x axis parameter value is expected to disappear.

These plots, as described in Figures 4.34 and 4.35 show the expected constant behaviour in approximately 90% of the data.

As can be clearly seen in Figure 4.34, around 10% of the data is shifted by approximately 3 ns, which coincides with a different clock cycle. This effect which is highlighted in these plots is indicative of the fact that the calibration formula (referred to in section 4.4) is an accurate approximation for most of the analysed data, however requires additional refining. Nevertheless, the advantage of this fine time calibration process is due to the fact that the calibration procedure is performed using only the distribution of the TDC file values, without the need of any external information, such as a reference time.

TDCs calibration can be performed also using data from a run with SiPMs collecting *fine* payload from dark count events.
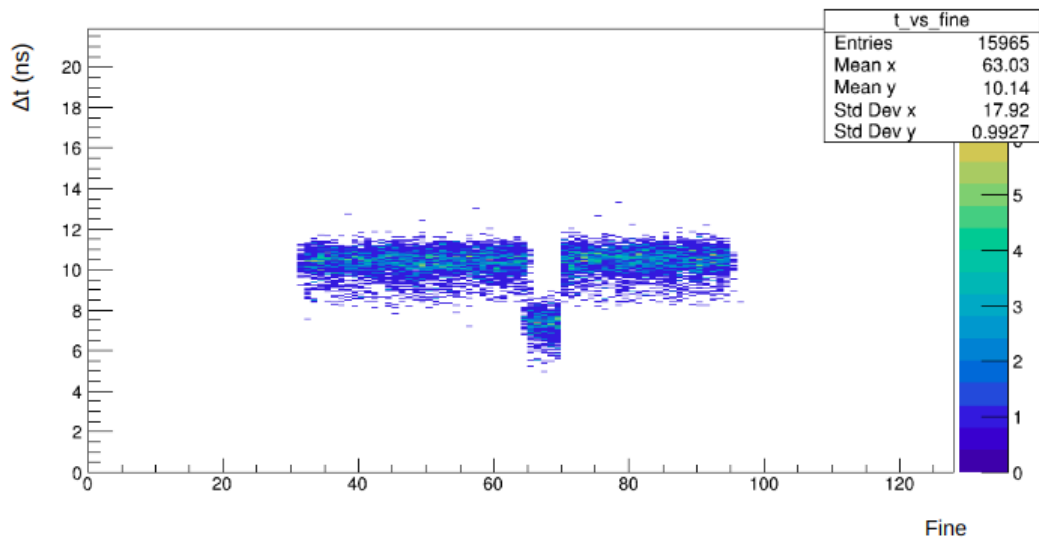
Figure 4.34: Difference between measured coincidence signal time t and Reference Time T as a function of the fine values.
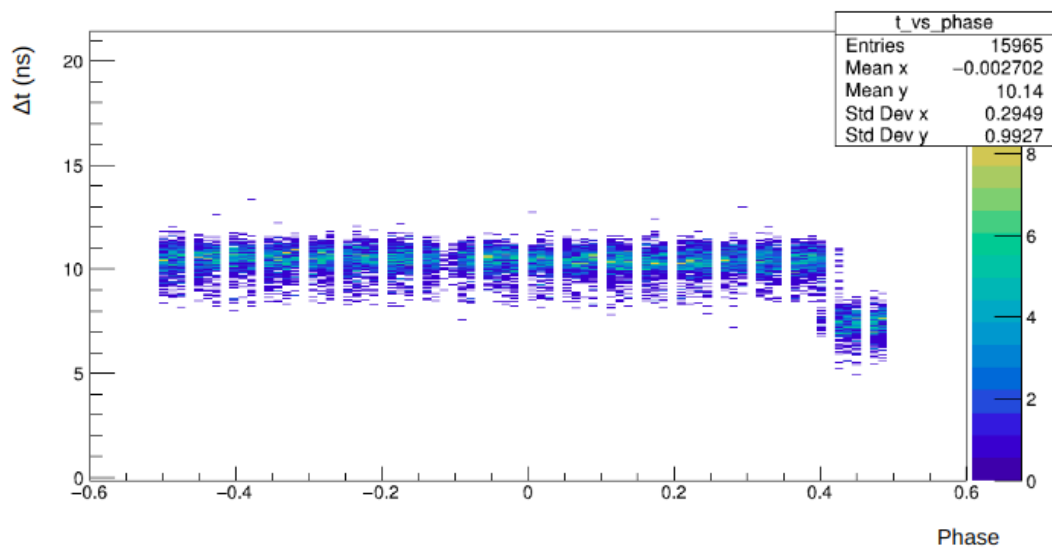

Figure 4.35: Difference between measured coincidence signal time t and Reference Time T as a function of the phase values.

4.6 Offset Calibration

Distinct channels may have a different time-delay calibration constant due to the dissimilar length of the signal traces on the PCBs (printed circuit boards) of the electronic cards.
An offset calibration is introduced in order to take this effect into account and obtain a better time resolution.

Figure 4.36 represents the time coincidence signal registered by all SiPMs hosted by the 6 carrier boards.
It can be noticed in the plot that the TDC calibration indices corresponding to the imaging SiPM sensors (index < 512) present some scattered background in addition to the time coincidences, whereas no background can be seen in the case of the timing SiPM TDC indices.
The reason for this difference is due to the different configuration and application of these two sets of SiPM sensors.
In the case of the imaging SiPMs, the signal to be detected corresponds to the signal generated by a single photon and therefore the threshold on the readout electronics must be maintained at a low level to accept such small signals. It is known that the SiPM signals from single photons cannot be distinguished from dark counts, hence the presence of the scattered background in the plot.
On the other hand, the timing SiPMs were coupled with plastic scintillators, which typically release a large number of photons when traverse by a charged particle. For this reason, the threshold on the timing SiPM was higher than the one used for the imaging SiPM and the chances to detect dark counts from the SiPM were negligible, hence the much cleaner time coincidences.

The timing sensor calibration carries an additional complication due to the fact that each time a channel of the timing SiPMs is calibrated, this leads to the Reference Time needing a recalculation, as its value before the calibration process depends on channels that haven't undergone the calibration process.
The method used to allow for this effect is described in section 4.6.

This is then simply added to the time coincidence signals in order to cancel out the different time-delay calibration constant of the different TDC calibration indices.
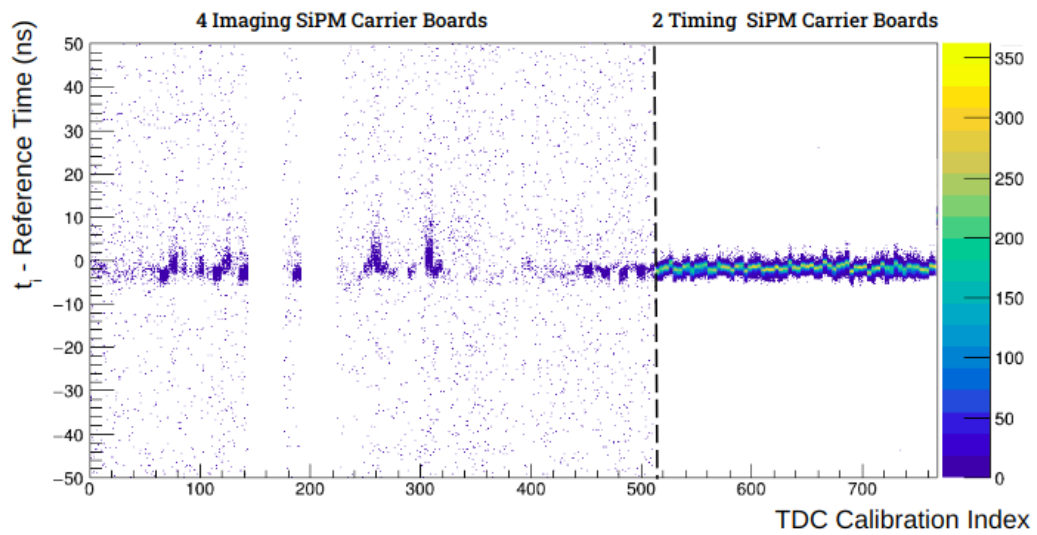
Figure 4.36: Time coincidence signal registered by all SiPMs hosted by the 6 carrier boards, represented by the 767 TDC calibration indices.

This calibration was performed on the Timing SiPM sensors, thereby the ones hosted by the carrier boards indicated with the 'chip' indices 4 and 5. The calibration on the

Timing SiPM sensors is performed on one TDC at a time.

The way the calibration algorithm works is the following: each time a TDC calibration index is selected, the time value of its registered coincidence signal is calculated, as well as its offset with respect to the Reference Time computed on all other TDCs excluding the TDC undergoing calibration. As described in the previous paragraph, the sum of the calculated TDC coincidence signal time value and its offset value returned the its calibrated value.

This process will be repeated for each TDC of each SiPM until all 256 Timing TDC calibration indices will be calibrated.

Each time the Reference Time is calculated from the second iteration onward, the calculation on the average time over all TDCs of the two timing SiPM matrices will include the time value registered by a TDC that has already gone through the calibration process, changing the value of this Reference Time slightly.

This will cause the already calibrated TDCs to be somewhat "off" calibration every time the Reference Time is newly calculated.

To take this effect into account, the calibration algorithm loop will be repeated on the entire set of timing TDC calibration indices multiple times until it reaches a determined precision level threshold.

In this analysis, convergence has been achieved after 4 loops.

At this point, the offset value for each TDC will be obtained and will be used to calibrate each channel and align the time coincidence signals.

The following plots are reported as a graphic example of the described process.

The timing offset calibration process of the data reported in Figure 4.36 starts by selecting a TDC calibration index between 512 and 767, which correspond to the timing SiPMs. When isolated, a bin of the aforementioned plot represents the coincidence time signal of each TDC, represented by a gaussian curve.

As an example, the plot of the coincidence time signal registered by the selected TDC calibration index 700 is reported in Figure 4.37.
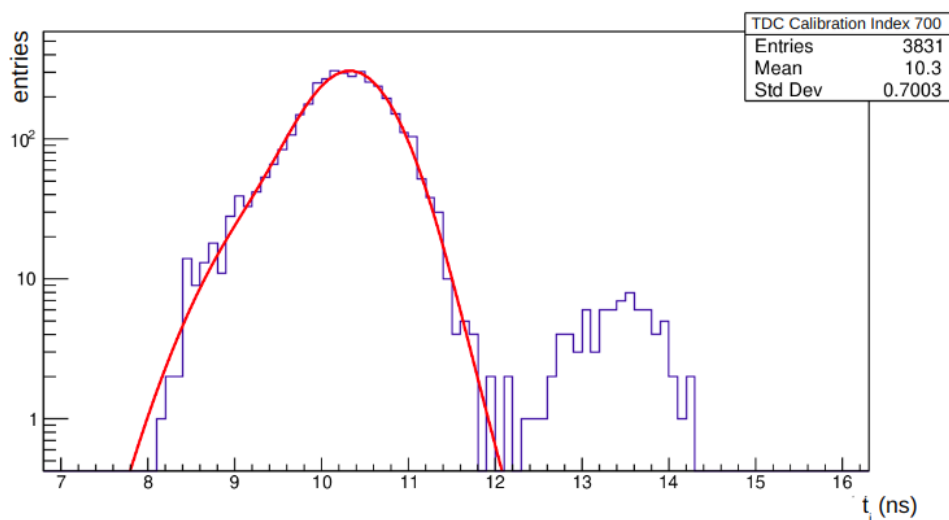

Figure 4.37: Coincidence time signal registered by the selected TDC calibration index 700 (TDC 0, pixel 3, column 3, chip 5).

In addition to the Gaussian representing the signal, described by the tallest curve with peak between 10-11 ns, two other contributions can be observed: a tail on its left another smaller peak present on its right.

For best results when calculating the coincidence signal time, all other effects should be removed or, in any case, minimised.

The first step towards this objective was taken by performing a cut on the absolute value of the phase parameter. While previously in the range between [-0.5; +0.5], it has at this point been restricted to the [-0.45; +0.45] range.

This cut was performed as a result of the information provided by Figures 4.34 and 4.35: inconsistencies throughout the data appear towards the clock front, which correspond to the regions close to the phase values of 0.5 and -0.5.

This cut results in the elimination of the smaller peak on the right, as shown in Figure 4.38.

The tail on the left of the Gaussian describing the TDC resolution is attributed to time walk (see section 4.1 for further details on the time walk effect).

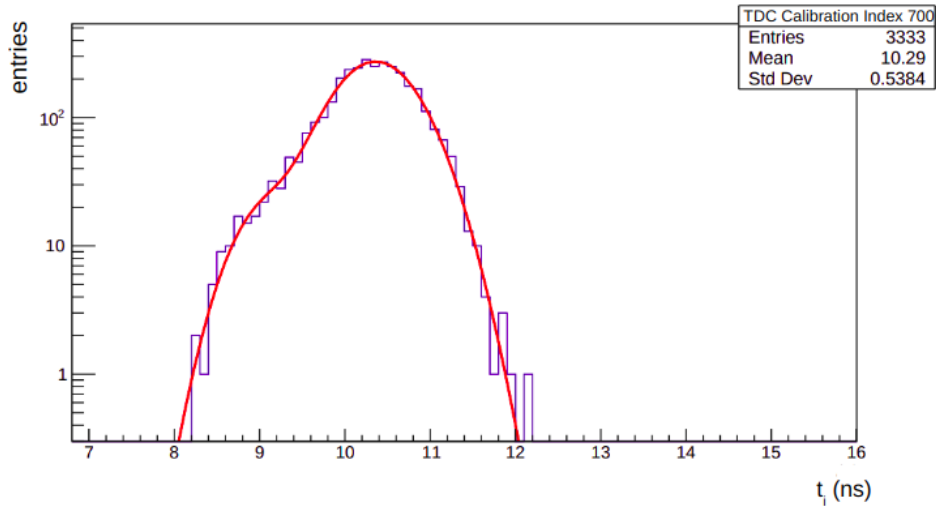An attempt of reducing this contribution was made by performing an additional cut

Figure 4.38: Coincidence time signal registered by the same selected TDC calibration index 700 after the performed cut.

around the 0 range of the phase value, excluding the range [-0.05; +0.05]. The effect of this cut resulted in decreasing the statistics by 10% while maintaining the mean of the distribution nearly unchanged, therefore this cut was not applied to the data analysis code.

Once the required cuts are performed and a time coincidence signal distribution as shown in Figure 4.38 is obtained, its mean value is obtained and is employed in the calculation for the offset value of the selected channel. The time difference (expressed in ns) between the obtained mean and the Reference Time represents the offset correction to be applied to each TDC calibration index.

The time coincidence signals provided by the TDCs of all Timing SiPMs taken from Figure 4.36 are reported in Figure 4.39 and show the data before the offset calibration.

After the calibration process, the time coincidence signals provided by each TDC of all timing SiPMs are aligned with one another, as shown in 4.40.
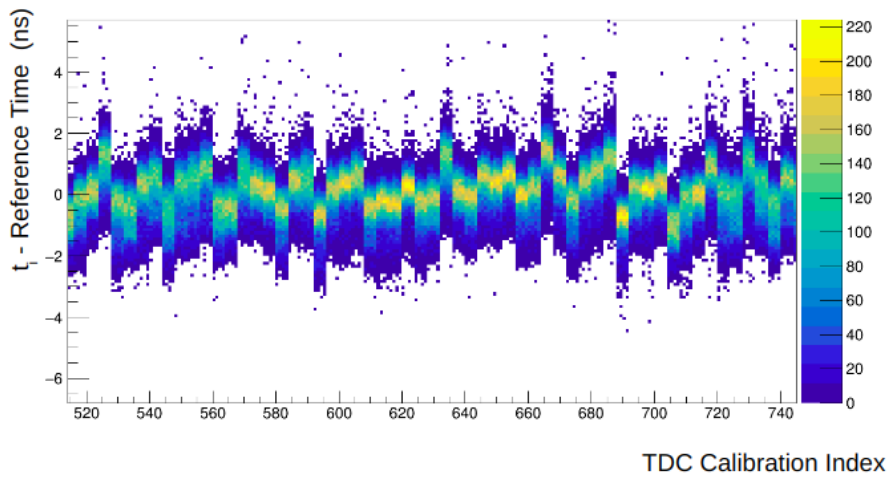

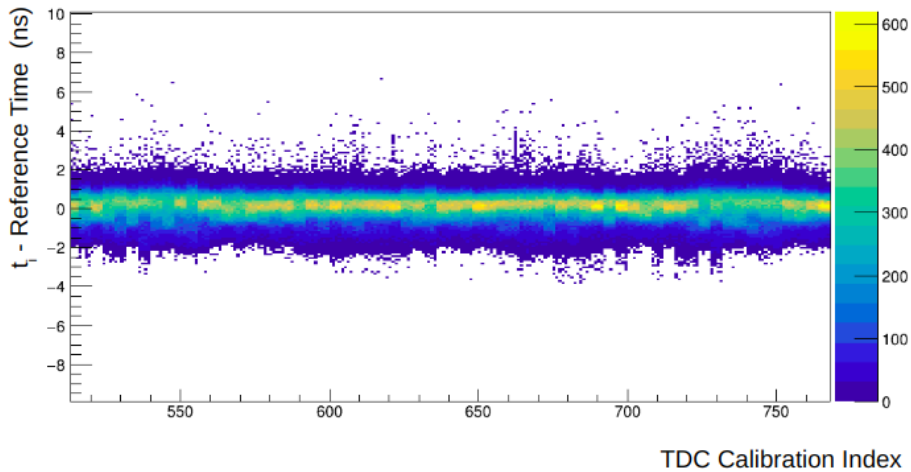Figure 4.39: Timing SiPM coincidence time signals before offset calibration.

Figure 4.40: Timing SiPM coincidence time signals after offset calibration.

4.7 Timing Sensor Time Resolution

Figures 4.41 and 4.42 represent the difference between the coincidence time signal average calculated on the timing SiPM arrays hosted by the two carrier boards 4 and 5 before and after offset calibration.

The plotted value ΔT is described by the formula:

$$\Delta T = T_4 - T_5 \tag{4.14}$$

where T_4 and T_5 represent the average of the coincidence time signals calculated on all 32 SiPMs hosted by the two timing sensor carrier boards, as described in eq.4.4.

The Time Resolution (σ_T) of the Timing System is defined in the following formula:

$$\sigma_T^2 = \frac{\sigma_{T4}^2 + \sigma_{T5}^2}{4} \tag{4.15}$$

it is possible to obtain the value of the term $\sigma_{T4}^2 + \sigma_{T5}^2$ (before and after offset correction) from the sigma value of the fit on the plots in Figures 4.41 or 4.42:

$$\sigma_{\Delta_T}^2 = \sigma_{T4}^2 + \sigma_{T5}^2 \tag{4.16}$$

Once $\sigma_{\Delta T}^2$ value is obtained, by combining eq.4.15 and eq.4.16 it is possible to calculate the σ_T value through the expression:

$$\sigma_T^2 = \frac{\sigma_{\Delta T}^2}{4} \tag{4.17}$$

A Gaussian fits was performed on the plots in Figures 4.41 and 4.42. Because of the presence of tails on both ends of the curves, the fit range was restricted between [-0.5,0.5] in order to allow for a better approximation of the plot towards the mean.
Despite this adjustment, the fits show that the effect of the correction for offset is marginal.
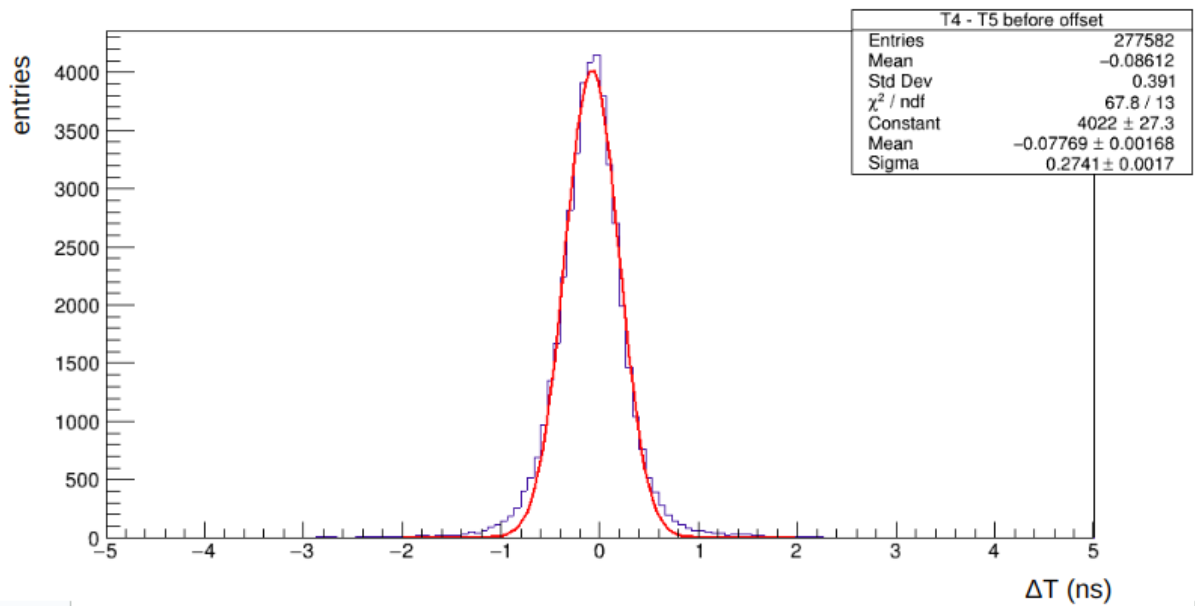
Figure 4.41: Fit on the plot representing the difference between the coincidence time signal average calculated on the two Timing SiPM sensors before offset correction.
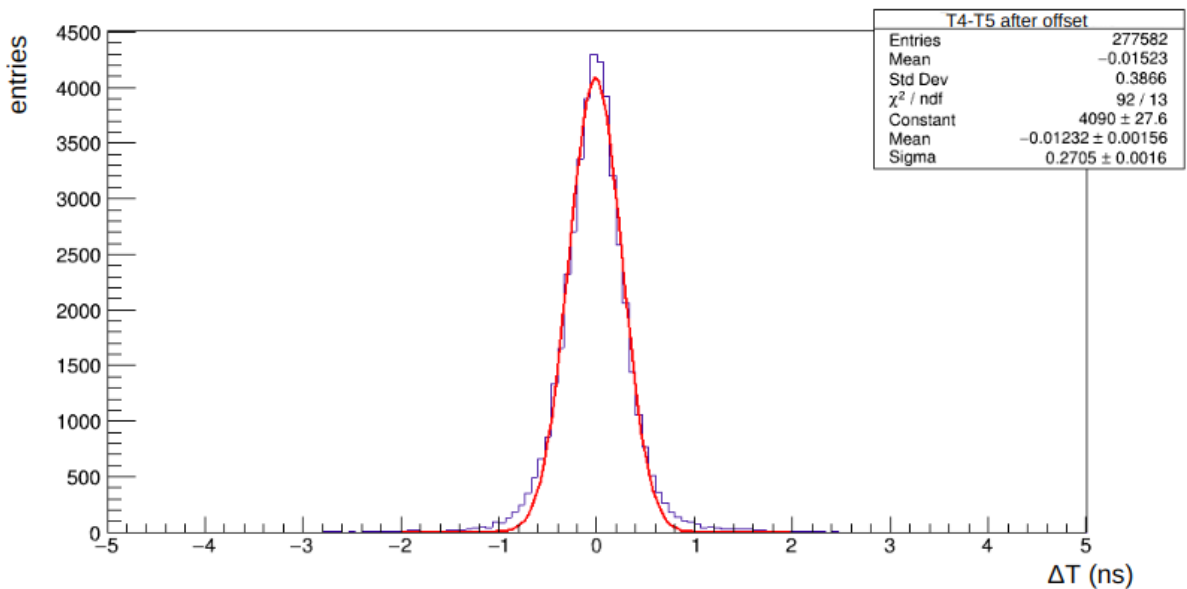

Figure 4.42: Fit on the plot representing the difference between the coincidence time signal average calculated on the two Timing SiPM sensors after offset correction.

122

The obtained $\sigma_{\Delta T}$ values, as well as the calculated Timing system Time Resolution σ_T values before and after the calibration for offset are reported in Table 4.3:

	$\sigma_{\Delta T}$	σ_T
Before Offset Calibration	0.274 ± 0.002	0.138 ± 0.014
After Offset Calibration	0.271 ± 0.002	0.135 ± 0.002

Table 4.3: Obtained $\sigma_{\Delta T}$ values and calculated Timing system Time Resolution σ_T values before and after offset calibration.

The results don't show a noticeable improvement in the Time Resolution value of the Timing system with the addition of the offset correction.

It is important to note, however, that this result is obtained without including some corrections which are suspected to improve its value, such as for time walk, time-over-threshold and low V_{bias}, which is not optimised for best performance.

Overall, the results show that the Time Resolution value achieved by this calibration of the Timing system is $\sigma_T = (135 \pm 2)$ ps.

4.8 Imaging Sensor Time Resolution

This preliminary study on the Time Resolution of selected Imaging channels was performed on one selected channel on each of the four Imaging sensor carrier boards.
As can be observed from Figure 4.23, the Cherenkov light only hits a few sensors on the board. The ones which were selected for this study were the ones which displayed the best statistics.

The plots in Figures 4.43, 4.44, 4.45 and 4.46 represent the difference between a Cherenkov light signal registered by an Imaging channel and the Reference Time as defined in the following formula:

$$\Delta t = t - T \tag{4.18}$$

where t represents the Imaging channel and T the Reference Time obtained by the Timing system (eq.4.3).

In an equivalent way as described in the previous paragraph, the sigma values obtained by fitting these plots ($\sigma_{\Delta t}$) are necessary for the calculation of the Imaging channel Time Resolution values σ_t.

This is possible by means of the following formulas:

$$\sigma_{\Delta t}^2 = \sigma_t^2 + \sigma_T^2 \tag{4.19}$$

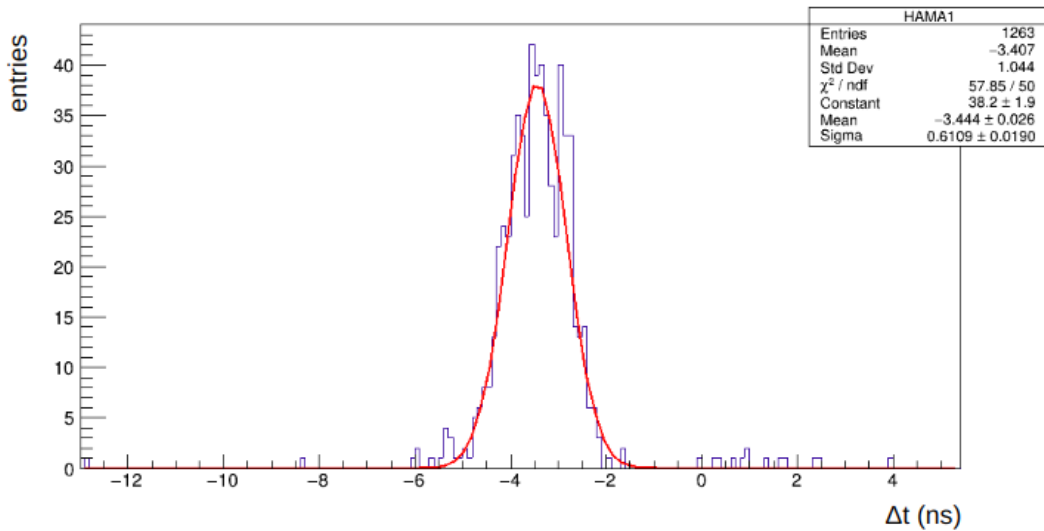$$\sigma_t^2 = \sigma_{\Delta t}^2 - \sigma_T^2 \tag{4.20}$$

Figure 4.43: Difference between a Cherenkov light signal registered by the selected HAMA1 channel (TDC calibration indices [64,68]: chip0, pixel0, column4, TDCs 0-3) and the Reference Time.
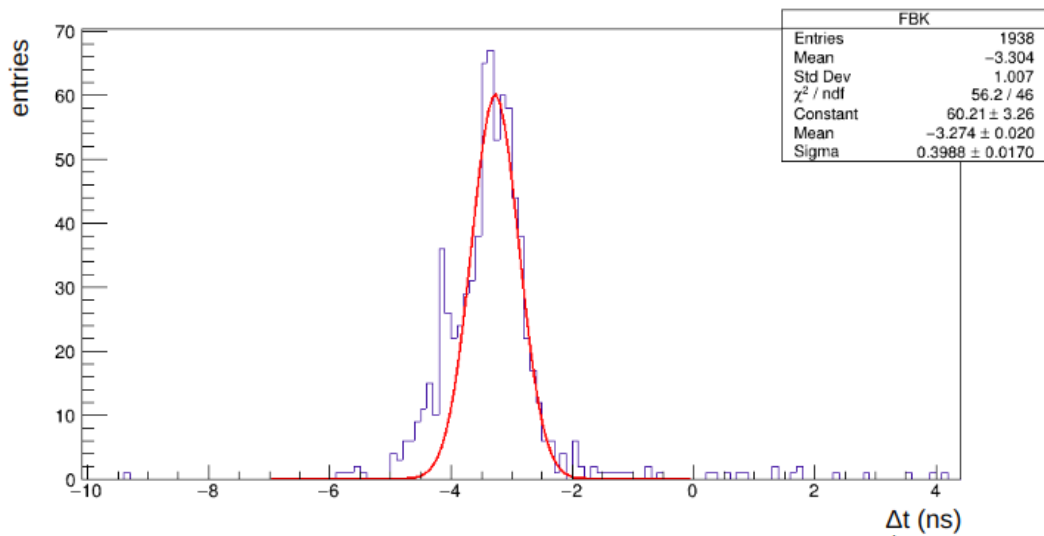

Figure 4.44: Difference between a Cherenkov light signal registered by the selected FBK channel (TDC calibration indices [136,140]: chip1, pixel3, column3, TDCs 0-3) and the Reference Time.
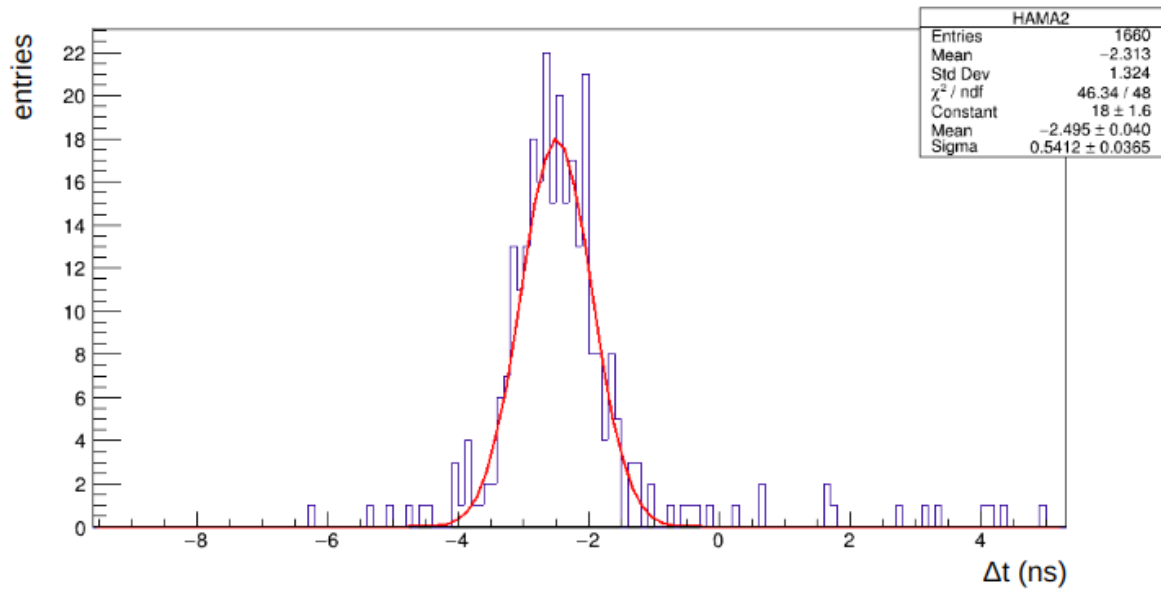
Figure 4.45: Difference between a Cherenkov light signal registered by the selected HAMA2 channel (TDC calibration indices [312,316]: chip2, pixel3, column0, TDCs 0-3) and the Reference Time.
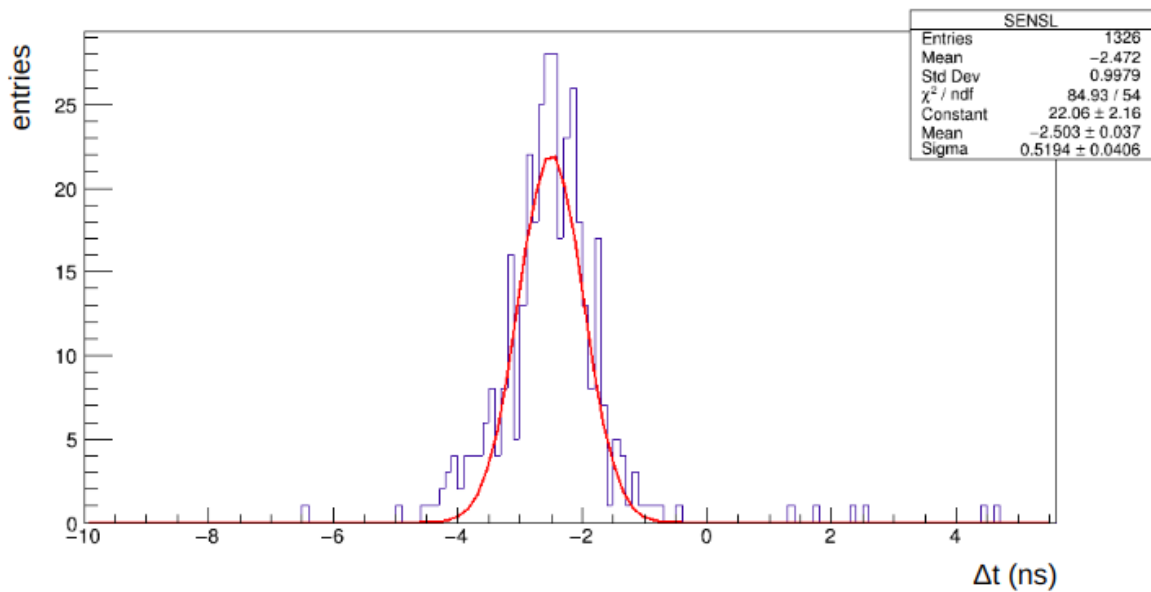

Figure 4.46: Difference between a Cherenkov light signal registered by the selected SENSL channel (TDC calibration indices [500,504]: chip3, pixel1, column7, TDCs 0-3) and the Reference Time.

It should be noted that the distribution for the FBK shows a tail on negative Δt, therefore the left range of the fit was limited to -3.90 to reduce the potential contribution due to time walk effects on the measured Time Resolution.

The obtained σ_{Δ_t} values from the fit, as well as the Imaging sensor Time Resolution σ_t values calculated owing to the Timing system Time Resolution are reported in Table 4.4:

Imaging Sensor	σ_{Δ_t}	σ_t
HAMA1	0.61 ± 0.02	0.59 ± 0.02
FBK	0.40 ± 0.02	0.37 ± 0.04
HAMA2	0.54 ± 0.04	0.52 ± 0.01
SENSL	0.52 ± 0.04	0.50 ± 0.01

Table 4.4: Obtained σ_{Δ_t} fit values and Time Resolution σ_t calculated on the Imaging sensors 4.8.

The calculated Imaging sensor Time Resolution values are within approximately 500 ps for all four tested SiPM manufacturers.

This result confirms the reliability of the obtained Timing system Time Resolution value of 135 ps.

4.9 Conclusions

The performance of Silicon PhotoMultipliers (SiPM), the baseline photo-sensor contender for the dRICH, was evaluated using a dRICH prototype. The tested SiPM technology was employed with two distinct objectives: Imaging sensors for the detection of the Cherenkov light produced in the dRICH and Timing sensors responsible for the calculation of a Reference Time to couple to the signal time-of-hit measurements provided from the Imaging sensors. The employed SiPM readout electronics chip, ALCOR, provides a signal time-of-hit measurement through the *rollover*, *coarse* and *fine* time contributions.

In this dissertation, a study on the refinement of the Time Resolution of the Reference Timing system is presented.
The corrections applied in order to improve the value of the Timing system Time Resolution is based on parameters obtained from the measured *fine* time component of the registered time coincidence signals.
The higher precision provided by this element becomes increasingly advantageous in an accelerator environment with high luminosity, in which performing cuts permits the reduction of background. The inclusion of this fine time component is, in fact, one of the SiPM background reduction techniques.

To test and to visualise the performance of the calibration procedure described, several checks were performed on dedicated channels.
The results show that it represents an accurate approximation for the correction of most (approximately 90%) of the analysed data, however requires additional refining. Nevertheless, the advantage of this calibration process is due to the fact that the procedure is performed using only the distribution of the TDC file values, without the need of any external information, such as a reference time. The TDC calibration can in fact be performed also using data from a run with SiPMs collecting the fine payload from only dark count events.

Overall, the performance of the studied SiPMs displayed satisfying results in both applications - the Imaging SiPMs were successful in registering the Cherenkov light signal and the Timing SiPMs provided a Reference Time value which allowed to correctly track the signal time-of-hits.
The Reference Timing system was calibrated to provide a measured Time Resolution of 135 ± 2 ps.

A preliminary study of the Imaging sensor Time Resolution, which for was calculated to be for a single photoelectron within approximately 500 ps, indicates that the value of the Timing system Time Resolution is adequate for the framework.

It is important to note that although these preliminary Time Resolution illustrate satisfactory results, they do not include corrections for effects such as time walk, time over threshold or low V_{bias} working conditions, which would presumably further improve the results.

Bibliography

[1] S. Vallarino, Prototype of a dual-radiator RICH detector for the Electron-Ion Collider

[2] E. C. Aschenauer, R. Sassot, and M. Stratmann,
arXiv:1206.6014. Phys. Rev. D86, 054020 (2012)

[3] M. Anselmino et al., J. Phys. Conf. Ser. 295, 012062 (2011), arXiv:1012.3565.

[4] J. Arrington, M.Battaglieri, A. Boehnlein: Physics with CEBAF at 12 GeV and
Future Opportunities
https://arxiv.org/pdf/2112.00060.pdf

[5] Jefferson Lab,
https://www.jlab.org/about

[6] COmmon Muon Proton Apparatus for Structure and Spectroscopy,
https://wwwcompass.cern.ch/

[7] Electron Ion Collider: The Next QCD Frontier Understanding the glue that binds us
all, Second Edition
BNL-98815-2012-JA, JLAB-PHY-12-1652, arXiv:1212.1701, December, 2014

[8] Science Requirements and Detector Concepts for the Electron-Ion Collider EIC Yel-
low Report
BNL-220990-2021-FORE, JLAB-PHY-21-3198, LA-UR-21-20953, October 2021

[9] Appendix A, Science Requirements and Detector Concepts for the Electron-Ion Col-
lider EIC Yellow Report
BNL-220990-2021-FORE, JLAB-PHY-21-3198, LA-UR-21-20953, October 2021

[10] M. Diehl: Generalized Parton Distributions
DESY-THESIS-2003-018 hep-ph/0307382, *https://arxiv.org/pdf/hep-ph/0307382.pdf*

[11] Larry McLerran, RIKEN-BNL Center and Physics Department, Brookhaven Na-
tional Lab., Upton, NY, 11973 USA, A Brief Introduction to the Color Glass Conden-
sate and the Glasma
$https://bibpubdb1.desy.de/record/296833/files/ismd08_mcl_intro-corr.pdf$

[12] Degele, D. (Deutsches Elektronen-Synchrotron (DESY), Hamburg (Germany)), The e-p collider HERA
$https://inis.iaea.org/search/search.aspx?orig_q = RN : 24054492$

[13] Brookhaven National Laboratory, Accelerators at Brookhaven Lab, Relativistic Heavy Ion Collider,
$https://www.bnl.gov/accelerators/rhic.php$

[14] CERN Accelerating Science, The Large Hadron Collider
$https://home.cern/science/accelerators/large-hadron-collider$

[15] CERN Accelerating science, Heavy ions and quark-gluon plasma
$https://home.cern/science/physics/heavy-ions-and-quark-gluon-plasma$

[16] Shanshan Cao and Xin-Nian Wang, Jet quenching and medium response in high-energy heavy-ion collisions: a review
$https://arxiv.org/pdf/2002.04028.pdf$

[17] Terry Sloan; Department of Physics, University of Lancaster, UK, History of the European Muon Collaboration (EMC)
$https://cds.cern.ch/record/2690197/files/91-79-PB.pdf$

[18] T. Sjostrand, S. Mrenna, P. Z. Skands, PYTHIA 6.4 Physics and Manual, JHEP 05 (2006) 026.
arXiv:hep-ph/0603175, doi:10.1088/1126-6708/2006/05/026.

[19] S. Agostinelli, et al., GEANT4–a simulation toolkit, Nucl. Instrum. Meth. A 506 (2003) 250–303.
doi:10.1016/S0168-9002(03)01368-8.

[20] R. Kersevan, M. Ady, Recent developments of Monte-Carlo codes Molflow+ and Synrad+, in: 10th International Particle Accelerator Conference, 2019, p. TUPMP037.
doi:10.18429/JACoW-IPAC2019-TUPMP037.

[21] T. Sjostrand, S. Mrenna, P. Z. Skands, A Brief Introduction to PYTHIA 8.1, Comput. Phys. Commun. 178 (2008) 852–867.
arXiv:0710.3820, doi:10.1016/j.cpc.2008. 01.036.

[22] B. P. Singh, et al., Experimental access to Transition Distribution Amplitudes with the PANDA experiment at FAIR, Eur. Phys. J. A 51 (8) (2015) 107.
arXiv:1409.0865,
doi:10.1140/epja/i2015-15107-y.

131

[23] F. Sauli, GEM: A new concept for electron amplification in gas detectors, Nucl. Instrum. Meth. A 386 (1997) 531–534.
doi:10.1016/S0168-9002(96)01172-2.

[24] J. Xie, Development of mcp-pmt/lappd and exploring their application for particle identification,
https://indico.bnl.gov/event/7449/contributions/35906/attachments/27154/41387/YR-Temple-2.pdf,

presentation at Temple Yellow Report Meeting (March 2020).

[25] M. Dugger, et al., A study of decays to strange final states with GlueX in Hall D using components of the BaBar DIRC (8 2014).
arXiv:1408.0215

[26] M. Helbich, Y. Ning, S. Paganis, Z. Ren, W. B. Schmidke, F. Sciulli, U. Schneekloth, C. Buttner, A. Caldwell, J. Sutiak, The Spectrometer system for measuring ZEUS luminosity at HERA, Nucl. Instrum. Meth. A 565 (2006) 572–588.
arXiv:physics/ 0512153,
doi:10.1016/j.nima.2006.06.049.

[27] W. Blum et al., Particle Detection with Drift Chambers, 2nd ed., Springer Verlag, 2008.

[28] H. Spieler, Semiconductor Detector Systems, Oxford University Press, 2005.

[29] C. Amsler et al. (Particle Data Group), The review of particle physics, Physics Letters B667 (2008) 1.

[30] *https://hub.hamamatsu.com/us/en/technical-notes/mppc-sipms/what-is-an-SiPM-and-how-does-it-work.html*

[31] E. Cisbani, A. Del Dotto, C.Fanelli, M. Williams: AI-optimized detector design for the future Electron-Ion Collider: the dual-radiator RICH case
arXiv:1911.05797v1 [physics.ins-det] 13 Nov 2019

[32] M. Ungaro, et al., Geant4 Monte Carlo (GEMC).
http://gemc.jlab.org

[33] S. Pereira, et al., Test of the CLAS12 RICH large-scale prototype in the direct proximity focusing configuration, Eur. Phys. J. A 52 (2) (2016) 1–15. arXiv:1509.02818, doi:10.1140/epja/i2016-16023-4

[34] C. M., et al., Aerogel mass production for the CLAS12 RICH: Novel characterization methods and optical performance, Nuc. Instrum. Meth. A 876 (2017) 168–172. doi:https://doi.org/10.1016/j.nima.2017.02.068

[35] C. Mironov, Studying nuclear matter created in p+p, d+Au and Au+Au collisions using charged kaons, J. Phys.: Conf. Ser. 50 (2006) 311-314.

[36] Christian Lippmann, GSI Helmholtzzentrum fur Schwerionenforschung
arXiv:1101.3276v4 [hep-ex] 12 Jun 2011

[37] F. M. Penning, Uber Ionisation durch metastabile Atome, Die Naturwissenschaften 15 (1927) 818-818.

[38] Hartmut F-W S. et al. 4d tracking with ultra-fast silicon detectors. Rep. Prog. Phys., 81(026101), 2018.

[39] Gundacker S. and Heering A. *The silicon photomultiplier: fundamentals and applications of a modern solid-state photon detector.* Phys. Med. Biol., 65(17TR01), 2020.

[40] *https://www.electricalvolt.com/2022/04/what-is-the-peltier-effect-peltier-cell-its-applications/*

[41] *https://www.xilinx.com/products/silicon-devices/fpga/what-is-an-fpga.html*

[42] *https://grafana.com/grafana/*

[43] P. Agnes et al, First Results from the DarkSide-50 Dark Matter Experiment at Laboratori Nazionali del Gran Sasso
arXiv:1410.0653v3 [astro-ph.CO] 27 Feb 2015

[44] Weishuai Cheng, Development of CMOS Integrated Circuits for SiPM Readout Doctoral Dissertation Doctoral Program in ELECTRICAL, ELECTRONICS AND COMMUNICATIONS ENGINEERING (32.th cycle)

[45] G. D'Alessandro1†, S.T. Boogert, S.M. Gibson, L.J. Nevay, W. Shields, John Adams Institute, Royal Holloway University of London, Egham, UK J. Bernhard, A. Gerbershagen, M.S. Rosenthal, CERN, Geneva, Switzerland also at CERN, Geneva, Switzerland, *IMPLEMENTATION OF CERN SECONDARY BEAM LINES T9 AND T10 IN BDSIM*
http://cdsweb.cern.ch/record/2693147/files/thpgw069.pdf